NASA CONTRACTOR REPORT

NASA CR-2550

NASA CR-2550

HYPERSONIC IONIZING AIR VISCOUS SHOCK-LAYER FLOWS OVER NONANALYTIC BLUNT BODIES

E. W. Miner and Clark H. Lewis

Prepared by
VIRGINIA POLYTECHNIC INSTITUTE AND STATE UNIVERSITY
Blacksburg, Va. 24061
for Lyndon B. Johnson Space Center

NATIONAL AERONAUTICS AND SPACE ADMINISTRATION • WASHINGTON, D. C. • MAY 1975

BIBLIOGRAPHIC DATA SHEET	1. Report No. NASA CR-2550	2.	3. Recipient's Accession No.
4. Title and Subtitle HYPERSONIC IONIZING AIR VISCOUS SHOCK-LAYER FLOWS OVER NONANALYTIC BLUNT BODIES			5. Report Date May 1975 6.
7. Author(s) E. W. Miner and Clark H. Lewis			8. Performing Organization Rept. No.
9. Performing Organization Name and Address Aerospace and Ocean Engineering Department Virginia Polytechnic Institute and State University Blacksburg, Virginia 24061			10. Project/Task/Work Unit No. 11. Contract/Grant No. NAS9-12630
12. Sponsoring Organization Name and Address L. B. Johnson Space Center Houston, Texas 77058 Technical Monitor: D. M. Curry Mail Code ES32			13. Type of Report & Period Covered Contractor Report 14.

15. Supplementary Notes E. W. Miner is currently with the National Air and Space Museum, Arts and Industries Bldg., 900 Jefferson Drive, Washington, D. C. 20560

16. Abstracts

Hypersonic, nonequilibrium viscous flow with ionization over nonanalytic blunt bodies is considered. The equations which govern the viscous shock-layer flow are presented and the method by which the equations are solved is discussed. The predictions of the present finite-difference method are compared with other numerical predictions as well as with experimental data. The principal emphasis is placed on predictions of the viscous flowfield for the windward plane of symmetry of the space shuttle orbiter and other axisymmetric bodies which approximate the shuttle orbiter geometry. Also considered are two slender sphere-cones at hypersonic conditions for which experimental data were available. The present predictions agreed well with with experimental data and with the predictions of Tong, Buckingham and Morse. Substantial differences were found between the present predictions and the predictions of the more approximate method of Kang and Dunn.

17. Key Words and Document Analysis. 17a. Descriptors

shock layers
laminar flows
chemically reacting flows
ionization
reentry bodies
space shuttle
heat-transfer
computer software

17b. Identifiers/Open-Ended Terms

17c. COSATI Field/Group

18. Availability Statement
Unclassified-Unlimited
Star Cat 34

19. Security Class (This Report) UNCLASSIFIED
20. Security Class (This Page) UNCLASSIFIED
21. No. of Pages 100
22. Price $4.75

*For sale by the National Technical Information Service, Springfield, Virginia 22151

TABLE OF CONTENTS

LIST OF FIGURES

LIST OF FIGURES cont.

LIST OF TABLES

LIST OF SYMBOLS

C_i	concentration of species i, ρ_i/ρ
C_p	specific heat at constant pressure
D_i	binary diffusion coefficient, $D_i^*\rho_\infty^*/\mu_{ref}^*$
ECW	denotes equilibrium catalytic wall
FVSL	denotes fully viscous shock layer
h	static enthalpy, h^*/U_∞^{*2}
H	total enthalpy, H^*/U_∞^{*2}
k	thermal conductivity, $k^*/(\mu_{ref}^* C_{p\infty}^*)$
Le_i	Lewis number, $C_p^*\ \rho^*\ D_i^*/k^*$
M	Molecular weight
$\overline{M}$	mixture molecular weight, $1/(\sum_i C_i/M_i)$
nj	number of species plus catalytic third bodies, ns + nz
ns	number of species
nr	number of chemical reaction
nz	number of catalytic third bodies
NSS	denotes no shock slip
N_e	number of electrons/CM^3
NCW	denotes noncatalytic wall
P	pressure, $P^*/(\rho_\infty^* U_\infty^{*2})$
Pr	Prandtl number, $C_p^*\mu^*/k^*$
q	heat transfer, $q^*/(\rho_\infty^* U_\infty^{*3})$
r	body radius, r^*/R_n^*
R	universal gas constant
R_n^*	body nose radius

Re_s	shock Reynolds number, $\dfrac{\rho_\infty^* U_\infty^* R_n^*}{\mu_{sh}^*}$
s	coordinate measured along body surface, s^*/R_n^*
s_{tan}	location of sphere-cone tangent point
St	Stanton number, $q_w/(H_\infty - H_w)$
SS	denotes shock slip
T	temperature, T^*/T_{ref}^*
T_{ref}^*	reference temperature, $U_\infty^{*2}/C_{p\infty}^*$
TVSL	denotes thin viscous shock layer
u	velocity component tangent to the body surface, u^*/U_∞^*
U_∞	freestream velocity
v	velocity component normal to the body surface, v^*/U_∞^*
y	coordinate measured normal to the body, y^*/R_n^*
z	coordinate measured along body axis, z^*/R_n^*
$Z_{(j-ns),i}$	third body catalytic efficiencies relative to argon
α	angle between shock tangent and body axis
α_{rj}	forward stoichiometric coefficients
β_{rj}	backward stoichiometric coefficients
γ_i	species mass concentrations, C_i/M_i
ε	Reynolds number parameter, $\left[\dfrac{\mu_{ref}^*}{\rho_\infty^* U_\infty^* R_n^*}\right]^{1/2}$
κ	surface curvature, $\kappa^* R_n^*$
μ	coefficient of viscosity, μ^*/μ_{ref}^*
μ_{ref}^*	coefficient of viscosity evaluated at T_{ref}^*
ρ	density, ρ^*/ρ_∞^*

ϕ	angle between body tangent and axis

Superscripts

j	indicator for axisymmetric flow (1) or two-dimensional flow (0)
*	dimensional quantities
'	denotes differentiation with respect to ξ

Subscripts

eq	equilibrium value
i	specie i
sh	value behind the shock
w	wall value
o	stagnation point value
∞	freestream value

FOREWARD

Reports Hypersonic Ionizing Air Viscous Shock-Layer Flows Over Nonanalytic Blunt Bodies (CR-2250) and Computer User's Guide For a Chemically Reacting Viscous Shock-Layer Program (CR-2251) by Miner and Lewis should be used together as source or reference material.

INTRODUCTION

While supersonic and hypersonic flows over blunt bodies have been of interest in fluid dynamics for many years, recent developments in aerodynamics and space flight have increasingly focused attention on the problem of predicting the blunt body flowfield. In the approach most commonly used, the flowfield over the body is treated in two parts, an inviscid outer flow and a viscous boundary layer. Many methods have been developed for solving the inviscid outer flow, as examples, the methods Inouye, Rakich and Lomax,[1] Rizzi and Inouye,[2] and Kutler, Reinhardt and Warming.[3] Likewise, many methods have been developed for solving the boundary-layer flow; two particular examples are the methods of Blottner and Flugge-Lotz[4] and Blottner.[5]

This approach to the problem generally worked quite well. It is, however, most appropriate for supersonic, high Reynolds number flows. As interest in hypersonic, low Reynolds number flows increased (for example, for reentry applications, including the space shuttle), problems were encountered in applying first-order boundary-layer theory to such flows. Some of the problems, such as displacement-thickness interaction, were partially met by using second-order boundary-layer theory, as an example the work of Lewis.[6] Another problem of the boundary-layer methods is determining the edge conditions. For supersonic, high Reynolds number flows, in which the boundary-layer is thin compared to the shock layer thickness and more specifically the entropy layer thickness,

it is generally adequate to consider the conditions at the boundary-layer edge to be the same as given by the inviscid solution at the body surface. For hypersonic, low Reynolds number flows in which the boundary layer is not thin, determining the edge conditions for the boundary layer can be most difficult (see, for example, Ref. 6). In the method of Blottner,[5] edge conditions were optionally determined by tracking streamlines from the shock crossing point to the boundary-layer edge or by entropy-layer swallowing.

Many of the problems (including those mentioned above) associated with computing viscous, hypersonic flows over blunt bodies can be overcome by the viscous shock-layer approach in which the entire flowfield from the body to the shock is treated in a unified manner. Knowledge of the shock shape is still required (to determine the flow properties behind the shock), but problems such as those of streamline tracking and displacement-thickness interaction are avoided. While many researchers have been involved in developing viscous shock-layer methods, the one who achieved perhaps the greatest degree of success was Davis.[7,8]

An alternative approach to obtaining solutions for hypersonic blunt body flows has been the use of the full Navier-Stokes equations, for example, the method of Jain and Adimurthy.[9,10] Such methods have been quite successful in providing solutions for the stagnation region but generally have been applied only about one nose radius downstream. Further, the elliptic nature of the equations, at least in the physical coordinates, increases the complexity of the solution procedure and restricts the application of the methods in the downstream direction.

The first objective of the present research was to develop a method for predicting hypersonic, low Reynolds number flowfields over nonanalytic blunt

bodies with particular emphasis for the shuttle orbiter windward plane of symmetry. The downstream region was of considerable interest and the method could not be restricted to the stagnation region. A second objective was that the method would not be subject to the problems involved in applying boundary-layer theory to such flows (problems such as displacement-thickness interaction and streamline tracking).

Both objectives were partially met by the viscous shock-layer methods of Davis,[7,8] but his methods were restricted to analytic bodies such as hyperboloids for which the pressure distribution was nearly Newtonian. Despite the restriction to analytic bodies, the viscous shock-layer methods of Davis,[7,8] had several advantages. The principal equations were parabolic in the streamwise direction, and thus there was no restriction on obtaining downstream solutions. A finite-difference method was used for solving the equations which gave very good accuracy in reasonably short computing times. Further, and quite important, for increasing Reynolds numbers the equations tend to first order boundary-layer equations, and thus the methods were not restricted to only shock-layer flow regimes but could also be applied in the boundary-layer regime as well. In fact, the boundary-layer equations are a subset of the viscous shock-layer equations. Before discussing the present work, the methods of Davis[7,8] are briefly described.

In Ref. 7, Davis developed a set of viscous shock-layer equations for a perfect gas valid from the body to the shock. The equations are accurate from the body to the shock to second order in the Reynolds number parameter, ε. In the solution procedure used by Davis, a first global solution was obtained using the thin viscous shock layer (TVSL) assumption and subsequent global iterations were for a fully viscous shock layer (FVSL) or for TVSL. Davis considered only

hyperboloids and, for the first (TVSL) global iteration, used the assumption that the shock angle was the same as the body angle. In subsequent global iterations the shock angle was computed from the body angle and the previous global iteration value of the shock-layer thickness derivative. This technique successfully gave the correct shock shape for the analytic bodies Davis considered. In Ref. 8 the governing equations were extended to treat a reacting binary gas mixture. The viscous shock-layer equations were subsequently extended by Moss[11] for nonequilibrium air (O, O_2, NO, NO^+, N, N_2 and e^-) and other gas chemistries.

In the present work, the viscous shock-layer equations which follow the formulation of Davis were solved for flows over nonanalytic blunt bodies. The present method is for nonequilibrium, multi-component, ionizing air; dissociating oxygen is also included. Predictions of the present method were compared with the predictions of the boundary-layer method of Tong, Buckingham and Morse[12] for the space shuttle orbiter windward plane of symmetry at 224,000 feet. Predictions of the present method also were compared with predictions of perfect gas boundary-layer flow from the method given in Refs. 13 and 14, with predictions of seven-specie, nonequilibrium boundary-layer flow using the method described in Refs. 15 and 16, and with the no-injection, experimental data of Pappas and Lee.[17] Predictions of the present method were also compared with the results Kang and Dunn[18-21] obtained with a more approximate integral method. Predicted electron concentration profiles were compared with the predicted and experimental profiles given by Evans, Schexnayder, and Huber.[22]

ANALYSIS

In the present work, the governing equations for the viscous shock-layer flows follow the formulation of Davis[7,8] and Moss.[11] The shock-layer equations derive from the governing equations for reacting gas mixtures (such as given by Bird, Stewart and Lightfoot[23] or Williams[24]) written for a body oriented coordinate system as shown in Fig. 1. The equations are first nondimensionalized by variables of order one at the body surface (corresponding to high Reynolds number, boundary-layer flows). The equations are also nondimensionalized by variables of order one in the outer inviscid flow (corresponding to tne shock region). A single set of equations is then obtained by retaining terms from the equations in each set to second order. The resulting set of shock-layer equations is uniformly second-order accurate in the inverse Reynolds number parameter, ε, from the body to the shock. Both longitudinal and transverse curvature are included. As given by Davis, the governing viscous shock-layer equations were specialized for a perfect gas[7] or a binary, reacting mixture of oxygen atoms and molecules.[8] Moss[11] gave the shock-layer equations for a multi-component mixture of reacting gases.

Governing Equations

The equations for shock-layer flows of multicomponent gases are given below.

Continuity Equation:

$$\frac{\partial}{\partial s}\left[(r + y\cos\phi)^j \rho u\right] + \frac{\partial}{\partial y}\left[(1 + \kappa y)(r + y\cos\phi)^j \rho v\right] = 0 \qquad (1)$$

s-Momentum Equation:

$$\frac{1}{1+\kappa y}\rho u\frac{\partial u}{\partial s}+\rho v\frac{\partial u}{\partial y}+\rho uv\frac{\kappa}{1+\kappa y}+\frac{1}{1+\kappa y}\frac{\partial P}{\partial s}=\varepsilon^2\frac{\partial}{\partial y}\left[\mu\left(\frac{\partial u}{\partial y}-\frac{\kappa u}{1+\kappa y}\right)\right]+$$

$$\varepsilon^2\mu\left(\frac{2\kappa}{1+\kappa y}+\frac{j\cos\phi}{r+y\cos\phi}\right)\left(\frac{\partial u}{\partial y}-\frac{\kappa u}{1+\kappa y}\right) \qquad (2)$$

y-Momentum Equation:

$$\frac{\partial P}{\partial y}=\frac{\kappa}{1+\kappa y}\rho u^2-\frac{1}{1+\kappa y}\rho u\frac{\partial v}{\partial s}-\rho v\frac{\partial v}{\partial y}\qquad\text{(FVSL)} \qquad (3a)$$

which becomes

$$\frac{\partial P}{\partial y}=\frac{\kappa}{1+\kappa y}\rho u^2\qquad\text{(TVSL)} \qquad (3b)$$

if the thin shock-layer approximation is made.

Energy Equation:

$$\frac{1}{1+\kappa y}\rho u\,C_p\frac{\partial T}{\partial s}+\rho v\,C_p\frac{\partial T}{\partial y}-\frac{1}{1+\kappa y}u\frac{\partial P}{\partial s}-v\frac{\partial P}{\partial y}=$$

$$\varepsilon^2\frac{\partial}{\partial y}\left(k\frac{\partial T}{\partial y}\right)+\varepsilon^2\left(\frac{\kappa}{1+\kappa y}+\frac{j\cos\phi}{r+y\cos\phi}\right)k\frac{\partial T}{\partial y}-\varepsilon^2\sum_{i=1}^{ns}J_i\,C_{p_i}\frac{\partial T}{\partial y}+$$

$$\varepsilon^2\mu\left(\frac{\partial u}{\partial y}-\frac{\kappa u}{1+\kappa y}\right)^2-\sum_{i=1}^{ns}h_i\,\dot{w}_i \qquad (4)$$

Species Conservation Equations:

$$\frac{1}{1+\kappa y}\rho u\frac{\partial C_i}{\partial s}+\rho v\frac{\partial C_i}{\partial y}=\dot{w}_i-\varepsilon^2\frac{\partial}{\partial y}(J_i)-\varepsilon^2\left(\frac{\kappa}{1+\kappa y}+\frac{j\cos\phi}{r+y\cos\phi}\right)J_i \qquad (5)$$

where J_i is the diffusion mass flux term of species i, and

Equation of State:

$$P = \frac{\rho R T}{\overline{M} C^*_{p\infty}} \tag{6}$$

With binary diffusion only and with constant binary Lewis numbers (all equal), the diffusion mass flux term of the species is given by

$$J_i = -\frac{\mu}{Pr} Le_i \frac{\partial C_i}{\partial y} \tag{7}$$

The species mass fractions are given by

$$C_i = \rho_i / \rho \tag{8}$$

The frozen specific heat of the mixture is given by

$$C_p = \sum_{i=1}^{ns} C_i \, C_{p_i} \tag{9}$$

and the mixture molecular weight is given by

$$\overline{M} = \frac{1}{\sum_{i=1}^{ns} \frac{C_i}{\overline{M}_i}} \tag{10}$$

The preceding equations are nondimensional. The dimensional equations were nondimensionalized by the following relations:

$$u^* = u \, U^*_\infty \tag{11a}$$

$$v^* = v \, U^*_\infty \tag{11b}$$

$$T^* = T \, T^*_{ref} = T \, U^{*2}_\infty / C^*_{p\infty} \tag{11c}$$

$$P^* = P \, \rho^*_\infty \, U^{*2}_\infty \tag{11d}$$

$$\rho^* = \rho \, \rho^*_\infty \tag{11e}$$

$$\mu^* = \mu \, \mu^*_{ref} \tag{11f}$$

$$k^* = k\,\mu^*_{ref}\,C^*_{p_\infty} \tag{11g}$$

$$C^*_p = C_p\,C^*_{p_\infty} \tag{11h}$$

$$h^* = h\,U^{*2}_\infty \tag{11i}$$

$$w^*_i = w_i\,\rho^*_\infty\,U^*_\infty/R^*_n \tag{11j}$$

$$J^*_i = J_i\,\mu^*_{ref}/R^*_n \tag{11k}$$

$$s^* = s\,R^*_n \tag{11l}$$

$$y^* = y\,R^*_n \tag{11m}$$

$$\kappa^* = \kappa\,R^*_n \tag{11n}$$

and

$$r^* = r\,R^*_n \tag{11o}$$

The dimensionless parameters which appear in the shock-layer equations are given by the following relations:

$$Pr = C^*_p\,\mu^*/k^* \tag{12a}$$

$$\varepsilon = \sqrt{\frac{\mu^*_{ref}}{\rho^*_\infty\,U^*_\infty\,R^*_n}} \tag{12b}$$

and

$$Le_i = \rho^*\,C^*_p\,D^*_i/k^* \tag{12c}$$

For the finite-difference solution procedure, it is advantageous to transform the shock-layer equations. The independent and dependent variables (except for the species concentrations) are normalized by their local shock values. When the normal coordinate is normalized by the local shock-layer thickness, a constant number of finite-difference grid points with constant spacing between the body and the shock can be used. Also, interpolation is

not needed to determine the shock location and grid points in the normal direction need not be added.

The transformed independent and dependent variables are

$$\eta = y/y_{sh} \tag{13a}$$

$$\xi = s \tag{13b}$$

$$\bar{u} = u/u_{sh} \tag{13c}$$

$$\bar{v} = v/v_{sh} \tag{13d}$$

$$\bar{P} = P/P_{sh} \tag{13e}$$

$$\bar{\rho} = \rho/\rho_{sh} \tag{13f}$$

$$\bar{T} = T/T_{sh} \tag{13g}$$

$$\bar{\mu} = \mu/\mu_{sh} \tag{13h}$$

$$\bar{k} = k/k_{sh} \tag{13i}$$

and

$$\bar{C}_p = C_p/C_{p_{sh}} \tag{13j}$$

The transformations relating the differential expressions are

$$\frac{\partial}{\partial s} = \frac{\partial}{\partial \xi} - \frac{y'_{sh}}{y_{sh}} \eta \frac{\partial}{\partial \eta} \tag{14a}$$

$$\frac{\partial}{\partial y} = \frac{1}{y_{sh}} \frac{\partial}{\partial \eta} \tag{14b}$$

and

$$\frac{\partial^2}{\partial y^2} = \frac{1}{y_{sh}^2} \frac{\partial^2}{\partial \eta^2} \tag{14c}$$

where

$$y'_{sh} = \frac{dy_{sh}}{d\xi} \tag{14d}$$

When written in the transformed ξ,η coordinates, the s-momentum, energy and species continuity equations (Eqs. 2, 4 and 5) can be expressed in the following standard form for a parabolic partial differential equation:

$$\frac{\partial^2 W}{\partial \eta^2} + A_1 \frac{\partial W}{\partial \eta} + A_2 W + A_3 + A_4 \frac{\partial W}{\partial \xi} = 0 \tag{15}$$

where W represents $\bar{u}$ in the s momentum equation, $\bar{T}$ in the energy equation and C_i in the species continuity equations. The coefficients A_1 through A_4 are functions of the independent and dependent variables and may be written as follows:

s-momentum equation

$$A_1 = \frac{1}{\bar{\mu}} \frac{\partial \bar{\mu}}{\partial \eta} + \frac{\kappa y_{sh}}{1+\kappa y_{sh}\,\eta} + \frac{j\, y_{sh} \cos\phi}{r + y_{sh}\,\eta \cos\phi} + \frac{y_{sh}\, y'_{sh}\, \rho_{sh}\, u_{sh}}{\varepsilon^2\, \mu_{sh}\, (1+\kappa y_{sh}\,\eta)} \frac{\overline{\rho u}\eta}{\bar{\mu}}$$

$$- \frac{y_{sh}\, \rho_{sh}\, v_{sh}}{\varepsilon^2\, \mu_{sh}} \frac{\overline{\rho v}}{\bar{\mu}} \tag{16a}$$

$$A_2 = - \frac{\kappa y_{sh}}{1+\kappa y_{sh}\,\eta} \frac{1}{\bar{\mu}} \frac{\partial \bar{\mu}}{\partial \eta} - \frac{\kappa^2 y_{sh}^2}{(1+\kappa y_{sh}\,\eta)^2} - \frac{\kappa y_{sh}^2\, j \cos\phi}{(1+\kappa y_{sh}\eta)\,(r + y_{sh}\,\eta \cos\phi)} -$$

$$\frac{y_{sh}^2\, \rho_{sh}\, u'_{sh}}{\varepsilon^2\, \mu_{sh}\, (1+\kappa y_{sh}\,\eta)} \frac{\overline{\rho u}}{\bar{\mu}} - \frac{\kappa y_{sh}^2\, \rho_{sh}\, v_{sh}}{\varepsilon^2\, \mu_{sh}\, (1+\kappa y_{sh}\,\eta)} \frac{\overline{\rho v}}{\bar{\mu}} \tag{16b}$$

$$A_3 = - \frac{y_{sh}^2}{\varepsilon^2\, \mu_{sh}\, u_{sh}\, (1+\kappa y_{sh}\,\eta)\, \bar{\mu}} \left[\bar{P} \frac{\partial P_{sh}}{\partial \xi} + P_{sh} \frac{\partial \bar{P}}{\partial \xi} - \eta \frac{y'_{sh}}{y_{sh}} P_{sh} \frac{\partial P}{\partial \eta} \right] \tag{16c}$$

$$A_4 = - \frac{y_{sh}^2\, \rho_{sh}\, u_{sh}}{\varepsilon^2\, \mu_{sh}\, (1+\kappa y_{sh}\,\eta)} \frac{\overline{\rho u}}{\bar{\mu}} \tag{16d}$$

Energy equation

$$A_1 = \frac{1}{\bar{k}} \frac{\partial \bar{k}}{\partial \eta} + \frac{\kappa y_{sh}}{1+\kappa y_{sh}\,\eta} + \frac{y_{sh}\, j \cos\phi}{r + y_{sh}\,\eta \cos\phi} - \frac{y_{sh}}{k_{sh}\,\bar{k}} \sum_{i=1}^{ns} J_i\, C_{p_i} -$$

$$\frac{y_{sh}\,\rho_{sh}\, C_{p_i}\, \bar{\rho}\,\bar{C}_p}{\varepsilon^2\, k_{sh}\,\bar{k}} \left[v_{sh}\,\bar{v} - \frac{u_{sh}\, y'_{sh}\,\bar{u}\,\eta}{1+\kappa y_{sh}\,\eta} \right] \qquad (17a)$$

$$A_2 = A_4 \frac{1}{T_{sh}} \frac{\partial T_{sh}}{\partial \xi} - \frac{y_{sh}^2\, \dot{w}_2}{\varepsilon^2\, k_{sh}\,\bar{k}} \qquad (17b)$$

$$A_3 = -\frac{y_{sh}^2\, \dot{w}_1}{\varepsilon^2\, T_{sh}\, k_{sh}\,\bar{k}} + \frac{y_{sh}^2\, \mu_{sh}\,\bar{\mu}}{T_{sh}\, k_{sh}\,\bar{k}} \left[\frac{u_{sh}}{y_{sh}} \frac{\partial \bar{u}}{\partial \eta} - \frac{\kappa u_{sh}\,\bar{u}}{1+\kappa y_{sh}\,\eta} \right]^2 +$$

$$\frac{y_{sh}\, u_{sh}\,\bar{u}}{\varepsilon^2\,(1+\kappa y_{sh}\,\eta)\, T_{sh}\, k_{sh}\,\bar{k}} \left[y_{sh}\,\bar{P} \frac{\partial P_{sh}}{\partial \xi} + y_{sh}\, P_{sh} \frac{\partial \bar{P}}{\partial \xi} - y'_{sh}\, P_{sh}\,\eta \frac{\partial \bar{P}}{\partial \eta} \right] +$$

$$\frac{y_{sh}\, P_{sh}\, v_{sh}\,\bar{v}}{\varepsilon^2\, T_{sh}\, k_{sh}\,\bar{k}} \frac{\partial \bar{P}}{\partial \eta} \qquad (17c)$$

$$A_4 = -\frac{y_{sh}^2\, C_{P_{sh}}\, \rho_{sh}\, u_{sh}}{\varepsilon^2\,(1+\kappa y_{sh}\,\eta)\, k_{sh}} \frac{\bar{C}_p\,\overline{\rho u}}{\bar{k}} \qquad (17d)$$

Species Conservation Equation

$$A_1 = \frac{1}{JB} \frac{\partial JB}{\partial \eta} + \frac{y_{sh}\kappa}{1+\kappa y_{sh}\,\eta} + \frac{y_{sh}\, j \cos\phi}{r + y_{sh}\,\eta \cos\phi} - \frac{y_{sh}\,\rho_{sh}\, v_{sh}\,\overline{\rho v}}{\varepsilon^2 JB} +$$

$$\frac{y_{sh}\, y'_{sh}\,\rho_{sh}\, u_{sh}\,\overline{\rho u}\,\eta}{\varepsilon^2\, JB\,(1+\kappa y_{sh}\,\eta)} \qquad (18a)$$

$$A_2 = - \frac{y_{sh}^2 \rho_{sh} \bar{\rho} \; w_i^{\,1}}{\varepsilon^2 \, JB} \tag{18b}$$

$$A_3 = \frac{y_{sh}^2 \rho_{sh} \bar{\rho} \; w_i^{\,0}}{\varepsilon^2 \, JB} \tag{18c}$$

$$A_4 = - \frac{y_{sh}^2 \rho_{sh} u_{sh} \overline{\rho u}}{\varepsilon^2 \, JB \, (1+\kappa y_{sh} \eta)} \tag{18d}$$

where

$$JB = \frac{\mu_{sh} \bar{\mu} \, Le_i}{Pr_{sh} \overline{Pr}} \tag{18e}$$

In the transformed coordinates the remaining equations are

Continuity Equation

$$\frac{\partial}{\partial \xi} \left[y_{sh} (r + y_{sh} \eta \cos \phi)^j \rho_{sh} u_{sh} \overline{\rho u} \right] =$$

$$\frac{\partial}{\partial \eta} \left[(r + y_{sh} \eta \cos \phi)^j \{ y'_{sh} \rho_{sh} u_{sh} \overline{\rho u} \eta - (1+\kappa y_{sh} \eta) \rho_{sh} v_{sh} \overline{\rho v} \} \right] \tag{19}$$

y-momentum equation

$$\frac{P_{sh}}{y_{sh} \rho_{sh} u_{sh} v_{sh}} \frac{\partial \bar{P}}{\partial \eta} - \frac{\kappa u_{sh}}{v_{sh} (1+\kappa y_{sh} \eta)} \overline{\rho u}^{\,2} + \frac{v_{sh} \overline{\rho v}}{y_{sh} u_{sh}} \frac{\partial \bar{v}}{\partial \eta} +$$

$$\frac{\overline{\rho u}}{1+\kappa y_{sh} \eta} \left[\frac{\partial \bar{v}}{\partial \xi} + \frac{\bar{v}}{v_{sh}} \frac{\partial v_{sh}}{\partial \xi} - \frac{y'_{sh} \eta}{y_{sh}} \frac{\partial \bar{v}}{\partial \eta} \right] = 0 \tag{20a}$$

which becomes

$$\frac{\partial \bar{P}}{\partial \eta} = \frac{\kappa y_{sh}\, \rho_{sh}\, u_{sh}^2}{P_{sh}\,(1+\kappa y_{sh}\,\eta)}\ \frac{}{\rho u}^2 \qquad (20b)$$

if the thin shock-layer approximation is made, and

State Equation

$$\bar{P} = \bar{\rho}\,\bar{T}\,\frac{\bar{M}_{sh}}{\bar{M}} \qquad (21)$$

The energy and species conservation equations (Eqs. 4 and 5) include the rate of production terms, $\dot{w}_i$, of species i. The $\dot{w}_i$ terms are functions of both the temperature and the species concentrations. Blottner[5] and Davis[8] discuss the need for rewriting these terms so that the temperature or the species concentrations appear as one of the unknowns. For the energy equation, the production term is written so that the temperature appears as an unknown as given by Davis[8] as

$$\left(\frac{\dot{w}_i}{\rho}\right)_{k+1} = \left(\frac{\dot{w}_i}{\rho}\right)_k + \left[\frac{\partial}{\partial \bar{T}}\left(\frac{\dot{w}_i}{\rho}\right)\right]_k \left[T_{k+1} - T_k\right] \qquad (22)$$

where k denotes the iteration for which the solution is known and k+1 the iteration for which a solution is sought. Accordingly, the production term in the energy equation (Eq. 4) was rewritten as

$$\sum_{i=1}^{ns} h_i\, \dot{w}_i = \dot{w}_1 + T_{sh}\,\bar{T}\,\dot{w}_2 \qquad (23)$$

and the terms $\dot{w}_1$ and $\dot{w}_2$ appear in the energy equation coefficients (Eqs. 17b and 17c). For the species conservation equation, the production term was written so that the species mass fractions appear as an unknown as

$$\frac{\dot{w}_i}{\rho} = \dot{w}_i^{\,0} - C_i\,\dot{w}_i^{\,1} \tag{24}$$

and the terms $\dot{w}_i^{\,0}$ and $\dot{w}_i^{\,1}$ appear in the species conservation equation coefficients (Eqs. 18b and 18c).

The viscous shock layer for nonequilibrium chemistry is described by equations (15) through (21) together with the appropriate boundary conditions and relations for the thermodynamic and transport properties.

Boundary Conditions

At the body surface, the no slip boundary conditions were imposed. For $\eta = 0$, the surface conditions are

$$\bar{u} = 0 \tag{25a}$$

$$\bar{v} = 0 \tag{25b}$$

and

$$T = T_w \tag{25c}$$

where T_w is either a constant or has a specified variation. For a noncatalytic surface, (NCW), the species boundary conditions are

$$\frac{\partial C_i}{\partial \eta} = 0 \tag{25d}$$

The equilibrium catalytic wall (ECW) conditions are specified by

$$C_i = C_{i_{eq}}\,(T_w) \tag{25e}$$

In the present work the surface temperatures were sufficiently low that the ECW condition could be approximated by a fully catalytic surface (FCW) condition specified by

$$C_O = 0,\ C_{O_2} = 0.23456,\ C_{NO} = 0,\ C_N = 0,\ C_{NO^+} = 0 \text{ and } C_{N_2} = 0.76544 \tag{25f}$$

At the shock, the velocity components tangent and normal to the shock are not the same as the components tangent and normal to the body surface. The velocity components tangent and normal to the shock are denoted by $\hat{u}_{sh}$ and $\hat{v}_{sh}$ and the components tangent and normal to the body surface are denoted as u_{sh} and v_{sh}. The transformation relating the two sets of shock velocity components is

$$u_{sh} = \hat{u}_{sh} \sin(\alpha + \beta) + \hat{v}_{sh} \cos(\alpha + \beta) \tag{26a}$$

and

$$v_{sh} = -\hat{u}_{sh} \cos(\alpha + \beta) + \hat{v}_{sh} \sin(\alpha + \beta) \tag{26b}$$

where $\beta = \pi/2 - \phi$.

For shocks of finite thickness called shock slip (SS), the shock properties are given by the modifed Rankine-Hugoniot relations (see Davis[7,8] and Cheng[25]) below.

$$\rho_{sh} \hat{v}_{sh} = -\sin\alpha \tag{27a}$$

$$\varepsilon^2 \mu_{sh} \left(\frac{\partial \hat{u}}{\partial y}\right)_{sh} + \sin\alpha \, \hat{u}_{sh} = \sin\alpha \cos\alpha \tag{27b}$$

$$P_{sh} - \sin\alpha \, \hat{v}_{sh} = \frac{P_\infty}{\rho_\infty U_\infty^2} + \sin^2\alpha \tag{27c}$$

$$\varepsilon^2 k_{sh} \left(\frac{\partial T}{\partial y}\right)_{sh} + \sin\alpha \sum_{i=1}^{ns} C_{i_\infty} h_{i_{sh}} - \frac{\sin\alpha}{2} \left[(\hat{u}_{sh} - \cos\alpha)^2 + \sin^2\alpha - \hat{v}_{sh}\right]$$

$$= \sin\alpha \sum_{i=1}^{ns} C_{i_\infty} h_{i_\infty} \tag{27d}$$

and

$$\varepsilon^2 \frac{\mu_{sh}}{Pr_{sh}} Le_i \frac{\partial C_{i_{sh}}}{\partial y} + \sin\alpha \, C_{i_{sh}} = \sin\alpha \, C_{i_\infty} \tag{27e}$$

The quantity ρ_{sh} is determined from the equation of state (6) after determining P_{sh}, T_{sh} and $C_{i_{sh}}$ from Eqs. (27c), (27d) and (27e). In Eq. (27d) above, the species enthalpy at the shock, $h_{i_{sh}}$, is expressed directly in terms of T_{sh} before T_{sh} is determined.

With no shock slip (NSS) the Rankine-Hugoniot relations are used to determine the shock values. Eqs. (27a) and (27c) are unchanged. The expressions for $\hat{u}_{sh}$, T_{sh} and $C_{i_{sh}}$ become

$$\hat{u}_{sh} = \cos \alpha \tag{28a}$$

$$\sum_{i=1}^{ns} C_{i_\infty} h_{i_{sh}} - (\hat{u}_{sh} - \cos \alpha)^2/2 + (\sin^2 \alpha - \hat{v}_{sh})/2 = \sum_{i=1}^{ns} C_{i_\infty} h_{i_\infty} \tag{28b}$$

and

$$C_{i_{sh}} = C_{i_\infty} \tag{28c}$$

The shock conditions for the dependent variables (at y = 1) are

$$\overline{u} = \overline{v} = \overline{\rho} = \overline{P} = \overline{T} = 1 \tag{29a}$$

and

$$C_i = C_{i_{sh}} \tag{29b}$$

Surface Transport

The surface skin friction and heat transfer rates are given by the skin friction coefficient and Stanton number. The skin friction coefficient is given by

$$C_f = \frac{2\tau_w^*}{\rho_\infty^* U_\infty^{*2}} \tag{30a}$$

where

$$\tau_w^* = \left[\mu^* \frac{\partial u^*}{\partial y^*} \right]_w \tag{30b}$$

In terms of the nondimensionalized variables, the skin friction coefficient is given by

$$C_f = 2\varepsilon^2 \left[\mu \frac{\partial u}{\partial y} \right]_w \tag{30c}$$

The Stanton number is given by the expression

$$St = \frac{q_w^*}{\rho_\infty^* V_\infty^* (H_\infty^* - H_w^*)} \tag{31a}$$

or in the dimensionless variables

$$St = \frac{q_w}{H_\infty - H_w} \tag{31b}$$

where

$$q_w^* = - \left[k^* \frac{\partial T^*}{\partial y^*} - \sum_{i=1}^{ns} h_i^* J_i^* \right]_w \tag{31c}$$

and

$$q_w = -\varepsilon^2 \left[k \frac{\partial T}{\partial y} - \sum_{i=1}^{ns} h_i J_i \right]_w \tag{31d}$$

or

$$q_w = -\varepsilon^2 \left[k \frac{\partial T}{\partial y} + \sum_{i=1}^{ns} \frac{\mu}{Pr} Le_i h_i \frac{\partial C_i}{\partial y} \right]_w \tag{31e}$$

with the restriction of constant and equal Lewis numbers.

THERMODYNAMIC AND TRANSPORT PROPERTIES

The specific heat, Cp, and static enthalpy, h, are required for each of the species considered and for the gas mixture. Also required are the viscosity, μ, and the thermal conductivity, k. Since the multi-component gas mixture is considered to be a mixture of thermally perfect gases, the thermodynamic and transport properties for each species were calculated using the local temperature. The properties for the gas mixture were then determined in terms of the individual species properties. In this section all expressions are presented in terms of dimensional quantities, and the superscript star will not be used to denote dimensional quantities.

Thermodynamic Properties

The enthalpy and specific heat of the species were obtained from the thermodynamic data tabulated by Browne.[26-28] Browne gave tables of specific heat and enthalpy versus temperature in gm cal/gm mole - °K with the enthalpy as $(H - H^*)/T$ where H^* was the heat of formation. In the present work the units were converted as

$$\hat{H}_i = \frac{49686}{1.98726\ M_i} \quad \frac{H - H^*}{T} \quad ; \ ft^2/sec^2\text{-}°R \tag{32a}$$

and

$$\hat{C}_{p_i} = \frac{49686}{1.98726\ M_i} \ C_p ; \ ft^2/sec^2\text{-}°R \tag{32b}$$

Second-order Lagrangian interpolation was used to obtain the values of $\hat{H}$ and $\hat{C}p$ from the tables. The species enthalpy and specific heat were then obtained

from the expressions

$$h_i = T\,\hat{H}_i + \Delta h_i^F;\ ft^2/sec^2 \tag{33a}$$

and

$$C_{p_i} = \hat{C}_{p_i};\ ft^2/sec^2\text{-}°R \tag{33b}$$

where Δh_i^F is the heat of formation of species i. The tabulated values of enthalpy and specific heat are given in Tables I and II and the heats of formation are given in Table III.

Transport Properties

The viscosity of each of the individual species was calculated from the curve fit relation

$$\mu_i = \exp(C_i)\, T_k^{(A_i \ln T_k + B_i)};\ \frac{gm}{cm\text{-}sec} \tag{34}$$

where A_i, B_i and C_i are the curve fit constants for species from Blottner[29] which are given in Table IV and T_k is the local temperature in degrees Kelvin. The units of the species viscosity were converted to lbf-sec/ft^2.

The thermal conductivity of the individual species was calculated from the Eucken semi-empirical formula using the species viscosity and specific heat by the expression

$$k_i = \frac{\mu_i R}{M_i}\left(\frac{C_{p_i} M_i}{R} + \frac{5}{4}\right);\ \frac{lbf}{sec\ °R} \tag{35}$$

After the viscosity and thermal conductivity of the individual species were calculated, the viscosity and thermal conductivity of the mixture were calculated using Wilke's semi-empirical relations;

$$\mu = \sum_{i=1}^{ns} \left(\frac{X_i \, \mu_i}{\sum_{j=1}^{ns} X_i \, \Phi_{ij}} \right) ; \frac{\text{lbf-sec}}{\text{ft}^2} \tag{36}$$

$$k = \sum_{i=1}^{ns} \left(\frac{X_i \, k_i}{\sum_{j=1}^{ns} X_i \, \Phi_{ij}} \right) ; \frac{\text{lbf}}{\text{sec-}^\circ\text{R}} \tag{37}$$

where $X_i = C_i \, \overline{M}/M_i$

and $\Phi_{ij} = \left[1 + \left(\frac{\mu_i}{\mu_j} \right)^{1/2} \left(\frac{M_j}{M_i} \right)^{1/4} \right]^2 \left[\sqrt{8} \left(1 + \frac{M_i}{M_j} \right)^{1/2} \right]^{-1}$

In the present work, the diffusion model is limited to binary diffusion with the binary diffusion coefficients specified by the Lewis number from Eq. (12c).

$Le_i = \rho \, Cp \, D_i/k$

The values of the Lewis numbers used were 1.4.

CHEMICAL REACTION MODEL

In the present work, it is assumed that the chemical reactions proceed at a finite rate, and the rate of production terms, $\dot{w}_i$, of the individual species are needed. The production terms occur in the energy equation (Eq. 4) and the species conservation equations (Eq. 5). For a multi-component gas with ns distinct chemical species and nr simultaneous chemical reactions, the chemical reaction equations are written in the general stoichiometric form

$$\sum_{i=1}^{nj} \alpha_{ri} \; X_i \; \frac{k_{f_r}}{k_{b_r}} \; \sum_{i=1}^{nj} \beta_{ri} \; X_i \tag{38}$$

where r = 1, 2, ... nr and nj is equal to the sum of the species and the catalytic third bodies. The quantities X_i represent the chemical species and the catalytic third bodies, and the α_{ri} and β_{ri} are the stoichiometric coefficients for reactants and products. The rates at which the forward and backward reactions occur are specified by the forward and backward rate constants which are given by the equations

$$k_{f_r} = T_k^{C2_r} \exp\left(CO_r - C1_r/T_k\right) \tag{39a}$$

and

$$k_{b_r} = T_k^{D2_r} \exp\left(DO_r - D1_r/T_k\right) \tag{39b}$$

where T_k is the temperature in degrees Kelvin. The constants CO_r, $C1_r$, $C2_r$, DO_r, $D1_r$ and $D2_r$ depend in part on the specific reaction equations chosen. In

the present work reaction rate constants were matched to those used by Evans, Schexnayder and Huber[22] or by Kang and Dunn.[19] The reaction equations and rate constants for these two sets of data are given in Tables V and VI. Other rate constants were used for test purposes (from Blottner[29] and from Blottner[30]) and are given in Tables VII and VIII.

With the forward and backward reaction rate constants given by Eq. (39) the net mass rate of production of species i per unit volume, $\dot{w}_i$, is given by the equation

$$\frac{\dot{w}_i}{\rho} = M_i \sum_{r=1}^{nr} (\beta_{ri} - \alpha_{ri}) (L_{f_r} - L_{b_r}) \tag{40}$$

where

$$\alpha_r = \sum_{j=1}^{nj} \alpha_{rj} - 1$$

$$\beta_r = \sum_{j=1}^{nj} \beta_{rj} - 1$$

$$L_{f_r} = k_{f_r} \bar{\rho}^{\alpha_r} \prod_{j=1}^{nj} (\gamma_j)^{\alpha_{rj}}$$

$$L_{b_r} = k_{b_r} \bar{\rho}^{\beta_r} \prod_{j=1}^{nj} (\gamma_j)^{\beta_{rj}}$$

$$\bar{\rho}\ (gm/cm^3) = 0.51536\ \rho\ (slugs/ft^3)$$

For the ns species the mass concentrations γ_j are given by the expressions

$$\gamma_j = \frac{C_j}{M_j} \qquad j = 1, 2, \ldots ns$$

whereas for the catalytic third bodies the γ_j are given by the following expressions

$$\gamma_j = \sum_{i=1}^{ns} Z_{(j-ns),i}\, \gamma_i \qquad j = (ns+1), \ldots nj$$

The quantity $Z_{(j-ns),i}$ is the third body efficiency relative to argon and is determined from the reaction being considered.

As discussed previously, it is desirable to rewrite the expression for the rate of production terms so that the species concentrations appear as one of the unknowns. When rewritten in this way, the rate of production terms are given by the expression

$$\frac{\dot{w}_i}{\rho} = \dot{w}_i^0 - \dot{w}_i^1 C_i \tag{24}$$

where

$$\dot{w}_i^0 = \mu_i \sum_{r=1}^{nr} (\Gamma_{ri}^{+} L_{f_r} + \Gamma_{ri}^{-} L_{b_r}) \tag{41a}$$

$$\dot{w}_i^1 = \sum_{r=1}^{nr} [\Gamma_{ri}^{+} (L_{b_r}/\gamma_i) + \Gamma_{ri}^{-} (L_{f_r}/\gamma_i)] \tag{41b}$$

$$\Gamma_{ri}^{+} = \begin{cases} (\beta_{ri} - \alpha_{ri}) & \text{if } (\beta_{ri} - \alpha_{ri}) > 0 \\ 0 & \text{if } (\beta_{ri} - \alpha_{ri}) \leq 0 \end{cases}$$

$$\Gamma_{ri}^{-} = \begin{cases} 0 & \text{if } (\beta_{ri} - \alpha_{ri}) \geq 0 \\ -(\beta_{ri} - \alpha_{ri}) & \text{if } (\beta_{ri} - \alpha_{ri}) < 0 \end{cases}$$

As discussed previously, the energy equation required the rate of production terms rewritten with the temperature appearing as an unknown (Eq. 22). That form for the rate of production term was a function of the derivative of $\dot{w}_i/\rho$ with respect to T. With temperature in degrees Kelvin, T_k, the expression for the derivative is

$$\frac{\partial}{\partial T_k}\left(\frac{\dot{w}_i}{\rho}\right) = \frac{M_i}{T_k} \sum_{r=1}^{nr} (\beta_{ri} - \alpha_{ri}) \left[(C2_r + C1_r/T_k - \alpha_r) L_{f_r} - (D2_r + D1_r/T_k - \beta_r) L_{b_r}\right] \tag{42}$$

With the specification of the chemical kinetics, the system of governing equations for viscous shock-layer flows is complete.

As noted above, the rate of production terms are for nonequilibrium flows. As conditions approach equilibrium, the present technique encounters increasing difficulty in obtaining a converged solution, particularly at the stagnation point. For dissociating oxygen, Davis[8] following Blottner[30] rearranged the rate of production terms so that equilibrium conditions could be approached much more closely. For dissociating oxygen, the rate of production terms follow the procedure of Davis,[8] and solutions may be obtained closer to equilibrium with the dissociating oxygen model than with the multicomponent air model. In fact, a lower limit in altitude or pressure currently exists below which the solution of the multicomponent air gas model computer code will not converge. The lower limit depends on the body nose radius and must be determined for each vehicle based upon available data.

METHOD OF SOLUTION

In the present work, a finite-difference method (following Davis[7]) was used to solve the governing differential equations for the viscous shock-layer flows. The solutions for the continuity and n-momentum equations were obtained by integration with the trapezoidal rule. The s-momentum, energy and species conservation equations were expressed in the standard form for a parabolic partial differential equation

$$\frac{\partial^2 W}{\partial \eta^2} + A_1 \frac{\partial W}{\partial \eta} + A_2 W + A_3 + A_4 \frac{\partial W}{\partial \xi} = 0 \tag{15}$$

These equations were solved using the algorithm described by Davis.[7]

Solution for S-Momentum, Energy and Species Conservation Equations

With the finite-difference grid as shown in Fig. 2, Taylor series expansions are used to relate the partial derivatives to the function values at the finite-difference grid points. In the ξ direction the expansion for W is

$$W_{m+1}^n = W_m^n + \Delta\xi \left(\frac{\partial W}{\partial \xi} \right)_m^n + O\left[(\Delta\xi)^2\right]$$

Neglecting the terms of order $(\Delta\xi)^2$ gives the difference quotient for $\partial W/\partial \xi$ as

$$\frac{\partial W}{\partial \xi} = \frac{W_{m+1}^n - W_m^n}{\Delta\xi} \tag{43}$$

In the η-direction a variable grid spacing was used and the Taylor series expansions are

$$W_m^{n-1} = W_m^n - \Delta\eta_{n-1}\left(\frac{\partial W}{\partial \eta}\right)_m^n + \frac{(\Delta\eta_{n-1})^2}{2!}\left(\frac{\partial^2 W}{\partial \eta^2}\right)_m^n + O\left[(\Delta\eta_{n-1})^3\right]$$

and

$$W_m^{n+1} = W_m^n + \Delta\eta_n\left(\frac{\partial W}{\partial \eta}\right)_m^n + \frac{(\Delta\eta_n)^2}{2!}\left(\frac{\partial^2 W}{\partial \eta^2}\right)_m^n + O\left[(\Delta\eta_n)^3\right]$$

Neglecting the terms of order $(\Delta\eta)^3$ the above equations combine to give the following difference quotients.

$$\frac{\partial W}{\partial \eta} = a_1 W_m^{n+1} + b_1 W_m^n + c_1 W_m^{n-1} \tag{44a}$$

and

$$\frac{\partial^2 W}{\partial \eta^2} = a_2 W_m^{n+1} + b_2 W_m^n + c_2 W_m^{n-1} \tag{44b}$$

where

$$a_1 = \Delta\eta_{n-1}/(\Delta\eta_n\ \Delta\eta_T) \tag{45a}$$

$$b_1 = (\Delta\eta_n - \Delta\eta_{n-1})/(\Delta\eta_n\ \Delta\eta_{n-1}) \tag{45b}$$

$$c_1 = -\Delta\eta_n/(\Delta\eta_{n-1}\ \Delta\eta_T) \tag{45c}$$

$$a_2 = 2/(\Delta\eta_n\ \Delta\eta_T) \tag{45d}$$

$$b_2 = -2/(\Delta\eta_n\ \Delta\eta_{n-1}) \tag{45e}$$

$$c_2 = 2/(\Delta\eta_{n-1}\ \Delta\eta_T) \tag{45f}$$

$$\Delta\eta_T = \Delta\eta_n + \Delta\eta_{n-1} \tag{45g}$$

$$\Delta\eta_n = \eta_{n+1} - \eta_n \tag{45h}$$

$$\Delta\eta_{n-1} = \eta_n - \eta_{n-1} \tag{45i}$$

A more general approach is to evaluate the partial derivatives at $(m + \theta, n)$. The parameter θ gives the following finite-difference schemes.

$$\theta = \begin{cases} 0 & \text{explicit} \\ 1/2 & \text{Crank Nicholson} \\ 1 & \text{implicit} \end{cases}$$

The difference quotient representation of the partial derivatives in the η-direction then becomes

$$\frac{\partial W}{\partial \eta} = \theta \left(a_1 W_{m+1}^{n+1} + b_1 W_{m+1}^{n} + c_1 W_{m+1}^{n-1}\right) + (1 - \theta)\left(a_1 W_m^{n+1} + b_1 W_m^n + c_1 W_m^{n-1}\right) \tag{46a}$$

and

$$\frac{\partial^2 W}{\partial \eta^2} = \theta \left(a_2 W_{m+1}^{n+1} + b_2 W_{m+1}^{n} + c_2 W_{m+1}^{n-1}\right) + (1 - \theta)\left(a_2 W_m^{n+1} + b_2 W_m^n + c_2 W_m^{n-1}\right) \tag{46b}$$

Also the function W is evaluated at $(m + \theta, n)$ as

$$W = \theta W_{m+1}^{n} + (1 - \theta) W_m^n \tag{46c}$$

Substitution of Eqs. (43) and (46) into Eq. (15) gives the following simultaneous linear algebraic equations involving only W at m + 1.

$$\tilde{A}_n W_{m+1}^{n-1} + \tilde{B}_n W_{m+1}^{n} + \tilde{C}_n W_{m+1}^{n+1} = \tilde{D}_n \tag{47}$$

where n = 2, 3, ..., N-1. The coefficients for Eq. (47) are given by the following expressions:

$$\tilde{A}_n = (c_2 + A_{1_n}\, c_1)\,\Theta \tag{48a}$$

$$\tilde{B}_n = (b_2 + A_{1_n}\, b_1 + A_{2_n})\,\Theta + A_{4_n}/\Delta\xi \tag{48b}$$

$$\tilde{C}_n = (a_2 + A_{1_n} a_1)\,\Theta \tag{48c}$$

and

$$\tilde{D}_n = -\left[\left(\frac{\partial^2 W}{\partial \eta^2}\right)^n_m + A_{1_n}\left(\frac{\partial W}{\partial \eta}\right)^n_m + A_{2_n}\, W^n_m\right](1 - \Theta) - A_{3_n} + A_{4_n}\, W^n_m/\Delta\xi \tag{48d}$$

where A_{1_n}, A_{2_n}, A_{3_n} and A_{4_n} are the coefficients of Eq. (15) evaluated at the n^{th} grid point and are given by Eqs. (16), (17) and (18) for the s-momentum, energy and species conservation equations.

Assuming that

$$W^n_{m+1} = \tilde{E}_n\, W^{n+1}_{m+1} + \tilde{F}_n \tag{49}$$

is valid through the shock layer (see Richtmyer,[31] also Conte[32] and Carnahan, Luther and Wilkes[33]) then W^{n-1}_{m+1} is given by

$$W^{n-1}_{m+1} = \tilde{E}_{n-1}\, W^n_{m+1} + \tilde{F}_{n-1} \tag{50}$$

Substituting Eq. (50) into Eq. (47) and solving for W^n_{m+1} and comparing with Eq. (49) gives the recursion formulas

$$\tilde{E}_n = \frac{-\tilde{C}_n}{\tilde{B}_n + \tilde{A}_n\, \tilde{E}_{n-1}} \tag{51a}$$

and

$$\tilde{F}_n = \frac{\tilde{D}_n - \tilde{A}_n \tilde{F}_{n-1}}{\tilde{B}_n + \tilde{A}_n \tilde{E}_{n-1}} \tag{51b}$$

With the addition of expressions for n = 1 and n = N, the requirements for the algorithm are complete. At n = 1, $\left(\frac{\partial W}{\partial \eta}\right)^n_{m+1} = 0$ or $W^1_{m+1} = W_w$. That Eq. (47) remain valid irrespective of the finite-difference grid spacing in the η-direction requires

$$\tilde{F}_1 = W_w \text{ and } \tilde{E}_1 = 0, \text{ if } W^1_{n+1} = W_w \tag{52a}$$

or

$$\tilde{F}_1 = 0 \text{ and } \tilde{E}_1 = 1, \text{ if } \left(\frac{\partial W}{\partial \eta}\right)^n_{m+1} = 0 \tag{52b}$$

For n = N, the value of W is

$$W^N_{m+1} = W_{sh} \tag{53}$$

The solution of Eq. (15) is provided by the following algorithm. Starting with Eqs. (52), the $\tilde{E}_n$ and $\tilde{F}_n$ are evaluated (using Eqs. (16), (17), (18), (45) and (48)) with n increasing from 2 to N - 1. Then the W^n_{m+1} are evaluated from Eq. (49) with n decreasing from N - 1 to 1.

Solution for Y-Momentum and Continuity Equations

The normal momentum equation, Eq. (20a), is rewritten so that $\partial\overline{P}/\partial\eta$ may be evaluated directly as

$$\frac{\partial \overline{P}}{\partial \eta} = \frac{\kappa\, y_{sh}\, \rho_{sh}\, u^2_{sh}}{P_{sh}\,(1 + \kappa\, y_{sh}\, \eta)}\, \overline{\rho}\, \overline{u} - \frac{\rho_{sh}\, v^2_{sh}}{P_{sh}}\, \overline{\rho}\, \overline{v}\, \frac{\partial \overline{v}}{\partial \eta} -$$

$$\frac{y_{sh}\,\rho_{sh}\,u_{sh}\,v_{sh}}{P_{sh}\,(1 - \kappa\, y_{sh}\,\eta)}\;\bar{\rho}\,\bar{u}\left(\frac{\partial \bar{v}}{\partial \xi} + \frac{\bar{v}}{v_{sh}}\;\frac{\partial v_{sh}}{\partial \xi} - \frac{y'_{sh}}{y_{sh}}\,\frac{\partial \bar{v}}{\partial \eta}\right) \tag{54}$$

with only the first term on the right side of the equation retained when the thin shock-layer approximation is made, Eq. (20b). With the y-momentum equation written in this form, Eq. (54) or (20b), the pressure derivative with respect to η is calculated. With $\bar{P}$ at the shock known, $\bar{P}_{sh} = 1$, integration by the trapezoidal rule from the shock inward gives the solution of the normal momentum equation.

The continuity equation, Eq. (19), when integrated yields both the normal velocity (v) profile and the shock-layer thickness, y_{sh}. As given previously, the continuity equation is

$$\frac{\partial}{\partial \xi}\;[y_{sh}\,(r + y_{sh}\,\eta\cos\phi)^j\,\rho_{sh}\,u_{sh}\,\bar{\rho}\,\bar{u}] = \frac{\partial}{\partial \eta}\;[(r + y_{sh}\,\eta\cos\phi)^j\,\{y'_{sh}\,\rho_{sh}\,u_{sh}\,\bar{\rho}\,\bar{u}\,\eta$$

$$-\,(1 + \kappa\, y_{sh}\,\eta)\,\rho_{sh}\,v_{sh}\,\bar{\rho}\,\bar{v}\}] \tag{19}$$

where $j = 1$ for axisymmetric flow and $j = 0$ for two-dimensional flow.

The mass flux between the body ($\eta = 0$) and a given grid point n ($\eta = \eta$) is proportional to m_n (with m_N denoting $\eta = 1$, the shock) which is given by

$$m_n = \int_0^{\eta} y_{sh}\,(r + y_{sh}\,\eta\cos\phi)^j\,\rho_{sh}\,u_{sh}\,\bar{\rho}\,\bar{u}\,d\eta \tag{55}$$

Integrating Eq. (19) from 0 to η and substituting Eq. (55) gives the following form for the Continuity equation.

$$\frac{dm_n}{d\xi} = \int_0^{\eta} \frac{\partial}{\partial \eta}\;[(r + y_{sh}\,\eta\cos\phi)^j\;\{y'_{sh}\,\rho_{sh}\,u_{sh}\,\bar{\rho}\,\bar{u}\,\eta -$$

$$(1 + \kappa\, y_{sh}\,\eta)\,\rho_{sh}\,v_{sh}\,\bar{\rho}\,\bar{v}\}]\,d\eta \tag{56}$$

or equivalently as

$$\frac{dm_n}{d\xi} = (r + y_{sh}\,\eta\cos\phi)^j \{y'_{sh}\,\rho_{sh}\,u_{sh}\,\bar{\rho}\,\bar{u}\,\eta - (1 + \kappa\,y_{sh}\,\eta)\,\rho_{sh}\,v_{sh}\,\bar{\rho}\,\bar{v}\} \quad (57)$$

The term $dm_n/d\xi$ is obtained by evaluating Eq. (55) as $s + ds/2$ and $s - ds/2$ and dividing by ds. The normal velocity, v, is then obtained by rearranging Eq. (57).

The shock-layer thickness is obtained by integrating Eqs. (55) and (56) from 0 to 1 instead of from 0 to η. This gives

$$m_N = y_{sh}\,\rho_{sh}\,u_{sh}\,r^j \int_0^1 \bar{\rho}\,\bar{u}\,d\eta + j\,y_{sh}^2\,\rho_{sh}\,u_{sh}\cos\phi \int_0^1 \bar{\rho}\,\bar{u}\,\eta\,d\eta \quad (58)$$

and

$$\frac{dm_N}{d\xi} = (r + y_{sh}\cos\phi)^j \{y'_{sh}\,\rho_{sh}\,u_{sh} - (1 + \kappa\,y_{sh})\,\rho_{sh}\,v_{sh}\} \quad (59)$$

The term $dm_N/d\xi$ could also be evaluated from

$$\frac{dm_N}{d\xi} = \frac{1}{\Delta\xi}\left[(m_N)_{s + ds/2} - (m_N)_{s - ds/2}\right] \quad (60)$$

Rearranging Eq. (60) gives

$$(m_N)_{s + ds/2} = \Delta\xi\,\frac{dm_N}{d\xi} + (m_N)_{s - ds/2} \quad (61)$$

By evaluating m_N from Eq. (61), using Eq. (59) for $dm_N/d\xi$, Eq. (58) can be solved for the shock-layer thickness, y_{sh}.

When written as in Eq. (19), the continuity equation is indeterminate at $s = 0$. In order to evaluate the continuity equation at the stagnation point the following limit expressions as $\xi \to 0$ are used:

$r \to \xi$, $\cos \phi \to \xi$ and $u_{sh} \to \xi\, u'_{sh}$ where $u'_{sh} = d\, u_{sh}/d\xi$. Also, at $s = 0$, $y'_{sh} = 0$. With these expressions Eq. 19 becomes

$$\frac{\partial}{\partial \eta}\left[(1 + y_{sh}\,\eta)^{j+1}\, \rho_{sh}\, v_{sh}\, \bar{\rho}\, \bar{v}\right] = -\,(j+1)\, y_{sh}\,(1 + y_{sh}\,\eta)^{j}\, \rho_{sh}\, u'_{sh}\, \bar{\rho}\, \bar{u} \quad (62)$$

Denoting $r|_{\Delta\xi/2}$ as r_2 and $\cos\phi|_{\Delta\xi/2}$ as $\cos\phi_2$, an equivalent form of the continuity equation is

$$\frac{\partial}{\partial \eta}\left[(1 + y_{sh}\,\eta)^{j+1}\, \bar{\rho}\, \bar{v}\right] = \left(\frac{2}{\Delta\xi}\right)^{j+1} (j+1)\, y_{sh}\,(r_2 + y_{sh}\,\eta\cos\phi_2)^{j}\, \rho_{sh}\, u_{sh}\, \bar{\rho}\, \bar{u} \quad (63)$$

where $\rho_{sh}\, v_{sh} = -\sin\alpha = -1$ at $s = 0$ has been used. Integrating from 0 to η and rearranging terms gives the following expression for the normal velocity component.

$$\bar{v} = \left(\frac{2}{\Delta\xi}\right)^{j+1} \frac{(j+1)\, y_{sh}\, \rho_{sh}\, u_{sh}}{\bar{\rho}\,(1 + y_{sh}\,\eta)^{j+1}} \left[r_2^{j} \int_0^{\eta} \bar{\rho}\, \bar{u}\, d\eta + j\, y_{sh} \cos\phi_2 \int_0^{\eta} \bar{\rho}\, \bar{u}\, \eta\, d\eta \right] \quad (64)$$

Integrating Eq. (63) from 0 to 1 gives the following equation

$$(1 + y_{sh})^{j+1} = \left(\frac{2}{\Delta\xi}\right)^{j+1} (j+1)\, y_{sh}\, \rho_{sh}\, u_{sh} \left[r_2^{j} \int_0^{1} \bar{\rho}\, \bar{u}\, d\eta + j\, y_{sh} \cos\phi_2 \int_0^{1} \bar{\rho}\, \bar{u}\, \eta\, d\eta \right] \quad (65)$$

which can be solved for the shock-layer thickness, y_{sh}, by rearranging terms.

An alternate method for determining the shock-layer thickness, y_{sh}, is to directly match the mass flux through the shock with the mass flow in the shock layer between the body and the shock. The mass flux through the shock, corresponding to a given position on the body with radius r, is given by

$$\dot{m}_s = \rho_\infty^{*}\, U_\infty^{*}\, \frac{(2\pi)^{j}}{j+1}\,(r + y_{sh}\cos\phi)^{j+1} \quad (66)$$

The mass flux through the shock layer is given by

$$\dot{m}_{sl} = \int_0^{y_{sh}} \rho^* u^* \{2\pi (r + y \cos \phi)\}^j \, dy$$

or

$$\dot{m}_{sl} = \rho_\infty^* U_\infty^* \rho_{sh} u_{sh} y_{sh} (2\pi)^j \left[r^j \int_0^1 \bar{\rho} \bar{u} \, d\eta + j \, y_{sh} \cos \phi \int_0^1 \bar{\rho} \bar{u} \, \eta \, d\eta \right] \tag{67}$$

Equating the mass flux through the shock, $\dot{m}_s$, and the mass flux through the shock layer, $\dot{m}_{sl}$, gives

$$\frac{1}{j+1} (r + y_{sh} \cos \phi)^{j+1} = y_{sh} \rho_{sh} u_{sh} \left[r^j \int_0^1 \bar{\rho} \bar{u} \, d\eta + j \, y_{sh} \cos \phi \int_0^1 \bar{\rho} \bar{u} \, \eta \, d\eta \right] \tag{68}$$

which can be rearranged to solve for the shock-layer thickness. For $j = 0$ the Eq. (68) becomes

$$r + y_{sh} \cos \phi = y_{sh} \rho_{sh} u_{sh} \int_0^1 \bar{\rho} \bar{u} \, d\eta \tag{69a}$$

and for $j = 1$, Eq. (68) is written as

$$r^2 + 2r \, y_{sh} \cos \phi + y_{sh}^2 \cos^2 \phi = 2 \, y_{sh} \rho_{sh} u_{sh} \left[r \int_0^1 \bar{\rho} \bar{u} \, d\eta + y_{sh} \cos \phi \int_0^1 \bar{\rho} \bar{u} \, \eta \, d\eta \right] \tag{69b}$$

When Eq. (68) is rewritten for the limit of $s = 0$, the expressions for y_{sh} are equivalent to those obtained from Eq. (62).

Curvature for Nonanalytic Bodies

In the present work, two classes of nonanalytic blunt bodies were considered. For spherically blunted cones, the surface curvature is discontinuous at the sphere-cone tangent point. A continuous distribution of curvature was obtained by computing κ from the exponential approximation to the step function. The approximate value of κ was obtained from

$$\kappa = 1 - \{1 + \exp [-f (s - s_{tan})]\}^{-1} \tag{70}$$

where f is a constant with a typical value of 5. Calculations were made with other values of f and also with κ given by a true step function. These calculations showed that the effects of changing the value of f were mostly confined to the region $s = s_{tan} \pm 1$ and that few effects were observed for $s > 4$ or 5 or for $s < 0.5$.

The geometry for the second class of nonanalytic blunt bodies was specified in tabular form. For these bodies, the curvature was calculated from the expression

$$\kappa = \left[\left(\frac{d^2r}{ds^2}\right)^2 + \left(\frac{d^2z}{ds^2}\right)^2\right]^{1/2} \tag{71}$$

or from the equivalent expression

$$\kappa = \left|\frac{d^2r}{dz^2}\right| \left\{1 + \left(\frac{dr}{dz}\right)^2\right\}^{-1.5} \tag{72}$$

The derivatives in Eqs. (71) or (72) were evaluated with a four point walking least squares log-log curve fit.

Solution Procedure

At each s or ξ location the shock-layer equations were solved in the order of species, energy, s-momentum, continuity and y-momentum. At each location the solution was iterated until convergence was obtained for the tangential velocity, temperature and species concentration profiles at all points of the finite-difference grid. The convergence test required that

$$\left|1 - W_n^{k+1}/W_n^k\right| \leq \delta$$

where n denotes the finite-difference grid point, k denotes the previous iteration value of W_n, k + 1 denotes the new iteration value of W_n, W represents $\bar{u}$, $\bar{T}$ or C_i and δ is a small number, typically 0.01. After a converged solution was obtained at a specific location, ξ, the profiles were then used as initial profiles for obtaining a new solution at $\xi + \Delta\xi$. In this way the solution procedure marched downstream.

If the governing equations were fully parabolic, only one global iteration (i.e., a solution for the entire length of the body) would be sufficient. However, the equations depend upon $d\, y_{sh}/d\xi$ (and thus the shock angle). Also, the y-momentum equation (in FVSL form) depends upon $\partial\bar{v}/\partial\xi$ which is not known (especially at the stagnation point). The downstream dependence introduces an elliptic nature to the equations. The elliptic effect in the y-momentum equation is resolved by considering TVSL flows for the first global iteration. Subsequent global iterations may then be FVSL using the $\bar{v}$ profiles from the previous global iteration.

The elliptic effect due to $d\, y_{sh}/d\xi$ is resolved by making a suitable approximation for $d\, y_{sh}/d\xi$ for the first global iteration. Subsequent global iterations then use $d\, y_{sh}/d\xi$ (or the corresponding shock angle) as calculated

from the previous global iteration. In the work of Davis[7,8] only analytic bodies were considered and the assumption was made for the first global iteration that the shock and body angles were the same, i.e. that $d\, y_{sh}/d\xi = 0$. Then subsequent global iterations used the distribution of $d\, y_{sh}/d\xi$ calculated from the previous global iteration. In the present work this procedure was also used if the body geometry was nearly analytic as was the case for the tabular geometry considered. However, for the spherically blunted cones, the pressure distribution is highly non-Newtonian and the approximation that the shock and body angles are equal is inappropriate. For sphere-cones, an initial shock shape (and thus an initial distribution of $d\, y_{sh}/d\xi$) was determined from a blunt body, method of characteristics procedure such as that of Inouye, Rakich and Lomax.[1] This shock shape was used for the first global iteration and for subsequent global iterations, the shock angle was calculated from the body angle and the smoothed distribution of $d\, y_{sh}/d\xi$ from the previous global iteration.

RESULTS AND DISCUSSION

In the present work, the principal interest was in viscous shock-layer flows over nonanalytic blunt bodies such as the space shuttle orbiter and sphere-cones, but some predictions were made for flows over hyperboloids. Since for analytic bodies such as hyperboloids the present method is almost identical to that of Davis,[7,8] predictions of the present method for hyperboloids should agree almost exactly with the results of Davis.[8] While the results are not presented, such was indeed the case for the 10° half-angle hyperboloid at 225 Kft (Davis[8]). For this case the Reynolds number parameter was $\varepsilon = 0.197$ and the Reynolds number values were $Re_\infty/ft = 8355$, $Re_\infty/R_n = 690$ and $Re_s = 63.7$. Other cases considered by Davis[8] were from 100 Kft to 250 Kft with $Re_s = 9555$ to 23.7. The agreement of the present predictions with the predictions of Davis[8] for flow over a hyperboloid for this case indicates the accuracy of present technique.

In the present paper, predictions are presented for viscous shock-layer flows over four nonanalytic blunt bodies. In the first case, the geometry considered was the windward plane of symmetry of a space shuttle orbiter at 224 Kft and at a 34° angle of attack. In the second case, the body considered was a 20° sphere-cone at 280 and 310 Kft. This geometry was considered by Kang and Dunn[18-21] as approximating the windward plane of symmetry of a space shuttle. The third case considered was the RAM C reentry body, a 9° sphere-cone with $R_n = 0.5$ ft. at 25,000 fps at 230, 250, 265 and 275 Kft. The fourth case considered in the present paper was the 7.5° sphere-cone ($R_n = 1$ in. at $M_\infty = 13.4$) investigated by Pappas and Lee[17] in their experiments.

NASA Shuttle Geometry Case

The case considered by Tong, Buckingham and Morse[12] was a space shuttle orbiter geometry using the Rockwell Shuttle 2007 trajectory at altitudes between 300 and 180 Kft. They considered the windward plane of symmetry, and boundary-layer theory was used to predict the flow over the equivalent axisymmetric body. In Ref. 12 the body geometry was specified by a series of polynomial curve fits which were faired into a cone of half-angle corresponding to the angle of attack. In the present work the geometry considered followed the approach of Tong, but difficulties were encountered in directly using the polynomial curve fits for the forward portion of the body. In fact, the surface curvature as calculated from the polynomials was not only discontinuous but also changed sign. The polynomial curve fits were replaced by a table of s, r and z values, and a four point walking least squares log-log curve fit was used to interpolate for the needed values of r and z in this table. This approach gave a continuous distribution of surface curvature. The body geometry and the corresponding shock predicted by the present method are shown in Fig. 3 for an entry t = 800 sec. or an altitude of 224 Kft. Predictions by the present method were made for this particular case, since for the space shuttle at 224 Kft both the first-order boundary-layer theory used by Tong and the viscous shock-layer theory used in the present work should be equally appropriate.

The pressure distribution predicted by the present method for t = 800 sec. is shown in Fig. 4 with pressure distributions from Ref. 12 which were obtained with the tangent-cone approach. Results from the two methods agreed quite well.

Mass fraction profiles at the stagnation point are compared in Fig. 5. Even though there was no attempt made to match the reaction rate data used

in the present method with Tong's, the present results agreed reasonably well with his results. The most apparent differences were in the N profiles near the surface. Tong's results showed a pronounced rise in the N profile from the wall and then a gradual decrease with a sharp decrease near the shock. The N profile predicted by the present method showed a slight increase and then a decrease similar to that of the N profile of Tong. The O profiles were quite similar. The present method predicted a slightly more rapid decrease in the outer portion of the flowfield. The NO profiles were also quite similar. The present method predicted a higher peak value of NO slightly farther from the shock. In considering the difference between the present results and the results of Tong, it should be noted that not only were the reaction rates different, but also the present results were FVSL and the Tong results, at the stagnation point only, were TVSL. Considering these differences, the agreement between the present predictions and the predictions of Tong[12] was quite good.

While mass fraction profile differences did exist, there was little difference in the predicted stagnation point heat transfer as shown in the next figures. Heat-transfer distributions are shown in Figs. 6 and 7 and the wall temperature distribution is shown in Fig. 7. The predictions of the present method for the noncatalytic wall (NCW) condition showed a strong dependence on the gas model used. Over the front of the body, the heat transfer for nonequilibrium air (7 species) was as much as twice that for dissociating oxygen. This difference decreased downstream. For the equilibrium catalytic wall (ECW) condition, there was little difference between the predictions of the present method for nonequilibrium air and dissociating oxygen. For both the ECW and the NCW conditions the present multi-component gas results agreed well with the results of Tong, but the present method did not predict the rise in heat

transfer at s = 1 ft. that Tong predicted when entropy-layer swallowing was included. It should be noted that in the results of Tong the shock shape data used were for a different body and that entropy-layer swallowing effects are strongly dependent upon the shock shape. In the present method an initial shock shape was assumed and then updated after each global iteration. For this geometry the shock shapes from the second and third global iterations were essentially identical. A major advantage of the viscous shock-layer approach over the boundary-layer approach is evident from these results. For the viscous shock-layer approach, the shock shape is at least partially self-correcting with global iteration and problems such as displacement-thickness interaction and shock-generated external vorticity (entropy-layer swallowing and boundary-layer edge conditions) do not occur.

20° Sphere-Cone Case

Kang and Dunn[18-21] considered a 20° sphere-cone with R_n = 4 ft. since this geometry reasonably approximated the windward plane of symmetry configuration of a space shuttle. Flowfield predictions were presented for two altitudes, 280 and 310 Kft. Stanton number distributions predicted by the present method are shown in Fig. 8 with the results of Kang and Dunn. The present results showed a significant effect of altitude on the predicted heat-transfer distribution, but the effect was about half of that obtained by Kang and Dunn. The normalized heat-transfer distributions shown in Fig. 9 emphasize the differences between the present results and the results of Kang and Dunn. The normalized heat-transfer distributions showed little altitude effect for the present results but significant effects for the results of Kang and Dunn. Also, the shape of the distributions were quite different. The present results showed a sharp

decrease in q/q_0 over the spherical cap and a pronounced change in slope near the sphere-cone tangent point. The results of Kang and Dunn showed a more gradual decrease and a gradual change in slope.

Temperature profiles are shown in Figs. 10 and 11. The results of Kang and Dunn showed much less altitude dependence than did the present results. The present results correctly showed a thicker viscous layer at the higher altitude (most noticeable at s = 90) while the method of Kang and Dunn predicted almost exactly the same temperature profiles for the two altitudes, especially at s = 90. Moreover, the present results produced the downstream "recovery" of a thin boundary layer while the results of Kang and Dunn did not.

Predictions of the present method were also made for dissociating oxygen (O-O_2) flow over the 20° sphere-cone. The present predictions for 7 species air agreed well with the present predictions for dissociating oxygen for heat-transfer distributions and temperature profiles.

Predictions were also made (using reaction rate constants matched to those of Kang and Dunn[18-21] (see Table VI) for electron concentration profiles. The present predictions of the electron concentration profiles are shown in Figs. 12 and 13 with the profiles predicted by Kang and Dunn. The present predictions of N_e were much lower than the predictions of Kang and Dunn. Also, the present method predicted a monotonic decrease of N_e with increasing s; whereas, the method of Kang and Dunn predicted a minimum N_e at s = 10 or 30 with N_e at s = 90 higher than at s = 10, 30 and 50. Perhaps more significantly, the present method predicted the peak electron density in the viscous layer near the body; whereas, the method of Kang and Dunn predicted nearly the same profiles at 310 Kft and 280 Kft while the present method predicted much fuller electron density profiles (especially downstream) at 310 Kft than at 280 Kft.

The altitude effect predicted by the present method for both temperature and electron density profiles seems entirely reasonable and correct.

RAM C Reentry Case

The RAM C flights were part of a program conducted by the NASA Langley Research Center for studying flow-field electron concentrations under reentry conditions. The body for each RAM C flight was a 9° sphere-cone with a 6 in. nose radius. Associated with the experimental program were theoretical studies using numerical methods. For example, Kang and Dunn[18-21] used a TVSL integral method procedure to predict electron concentration profiles for several points on the RAM C trajectory. Also included in the Refs. 18-21 were other flow-field quantities such as temperature profiles and surface heat-transfer distributions.

The results presented by Kang and Dunn were for the higher altitude points on the RAM C trajectory where viscous shock-layer theory would be more appropriate. Predictions of the RAM C electron concentrations have also been made by other researchers. For example, Evans, Schexnayder and Huber[22,34] applied two different boundary-layer methods and obtained reasonable agreement with the experimental data with both methods. The use of the boundary-layer approach limited Evans et al. to consideration of the lower altitude points of the RAM C trajectory. However, the 230 Kft point was considered by Evans et al. and by Kang and Dunn. For the 230,000 ft. altitude point, predictions of the present finite-difference, viscous shock-layer method were compared with the predictions of a finite-difference, boundary-layer method (Evans, Schexnayder and Huber[22]) and the predictions of the TVSL integral method of Kang and Dunn.[18-21] In the present work the principal emphasis was not on predicting electron concentrations but rather was on predicting the hypersonic, viscous flowfield over nonanalytic blunt bodies with electron concentrations a part of the

flowfield predictions. The present results for the RAM C at 230 Kft included viscous shock-layer predictions for three gas models (perfect gas, dissociating oxygen, and multi-component, ionizing air). Also included were results of the inviscid, perfect gas method of Inouye, Rakich and Lomax,[1] a perfect gas, boundary-layer method (Refs. 13 and 14) and a seven species, nonequilibrium, ionizing air boundary-layer method (Refs. 14 and 15). Some predictions for flow over a 9° half-angle hyperboloid were included in addition to the predictions for the 9° sphere cone.

One reason for emphasizing the RAM C conditions at 230 Kft was experimental data and other numerical results for distributions of Stanton number, temperature behind the shock and shock-layer thickness in addition to temperature and electron concentration profiles. The experimental data and the numerical results of Evans, Schexnayder and Huber[22] were for electron concentration profiles only. The differences between the present predictions and the numerical results of Kang and Dunn[18-21] were unexpectedly large. Most of the discussion of the differences between the present results and the results of Kang and Dunn will be deferred to the end of this section.

Distributions of temperature behind the shock are shown in Fig. 14 for the RAM C sphere-cone and a 9° half-angle hyperboloid. Although the end of RAM C body was at s = 9.2 the results given by Kang and Dunn went to s = 90 and the present predictions were extended to s = 100. At the stagnation point there were small differences in T_{sh} due to differences in the gas model but the sphere-cone and hyperboloid gave the same value for the same gas model. The differences in T_{sh} due to differences in gas model for the present results were greatest at the stagnation point and decreased as the shock became more oblique. In the downstream portion of the flow, the principal differences in T_{sh} were due

to the differences in the bodies. The present results showed the expected differences in T_{sh} distributions for hyperboloids and sphere-cones and correctly predicted the distributions of T_{sh} coming together at $s \simeq 80$. In contrast to the present results, Kang and Dunn obtained a quite different distribution of T_{sh}.

Distributions of shock-layer thickness are compared in Fig. 15. While the present results show some distinct differences, they were in substantial agreement, especially for $s > 20$. The principal differences in the present results were again due to the differences in the bodies considered. The present shock-layer predictions showed only small differences in y_{sh} due to the chemistry. For the sphere-cone, the viscous shock-layer results were in reasonable agreement with the inviscid results but did not show as sharp a decrease in y_{sh} between $s = 15$ and 40. The present results for the hyperboloid were lower than the sphere-cone results for $s < 20$ but were about 50% greater for $s > 50$.

Temperature profiles are shown in Figs. 16 and 17. The profiles in Fig. 16 were for the probe location. The present method profile was for $s = 8.8$, the probe location. The profile of Kang and Dunn (for $s = 10$) was the profile closest to the probe location which they gave (the next closest profiles were for $s = 3.0$ and 20.0). The profiles in Fig. 17 were for $s = 90$. The profiles for the hyperboloid showed a smoother transition from the outer flow to an inner, viscous flow than did the present sphere-cone profiles. The profiles for dissociating oxygen showed a ten percent lower peak temperature than did the profiles for ionizing air. Despite these small differences, the four present profiles showed a very distinct inner viscous region ($y/y_{sh} = 0.0$ to 0.5) and an outer inviscid region ($y/y_{sh} = 0.5$ to 1.0). While not shown, the velocity profiles also indicated the edge of the viscous layer at $y/y_{sh} \simeq 0.5$.

The present viscous shock-layer temperature profiles have also been compared (not shown here) with the temperature profiles predicted by the seven species boundary-layer method[15,16] for flow over the 9° sphere-cone. The boundary-layer and viscous shock-layer profiles showed differences in peak and edge temperatures but were quite similar in character and the boundary-layer profiles also indicated the edge of the viscous layer at $y \simeq 1.0$ as did the viscous shock-layer profiles. Further, a comparison of the present profiles, as shown in Figs. 16 and 17, clearly showed the distinct downstream development of an outer inviscid flow and an inner viscous flow.

Electron concentration profiles for the RAM C at 230 Kft are shown in Figs. 18 and 19. The data that the present results are compared with were taken from figures in Ref. 22. In Fig. 18, the present results are compared with the experimental data and the results Evans, Schexnayder and Huber[22] obtained with a very reliable finite-difference, boundary-layer method (i.e. Blottner[30]). The reaction rate constants used for the present results in Fig. 18 were matched to those of Ref. 22 (Table V). The present results agreed reasonably well with the experimental data and with the boundary-layer theory results of Ref. 22 as to level of ionization and quite well with the boundary-layer theory results as to character of the N_e profile. The present viscous shock-layer theory predicted a higher temperature in the viscous layer than did the boundary-layer theory of Ref. 22, and this difference accounted for most of the difference in the N_e profiles.

Predictions of electron concentrations were also influenced by the reaction rates used. Predictions were made for the RAM C case using reaction rate constants matched to those of Kang and Dunn[19] (Table VI). The profiles predicted using the two different sets of rate constants are compared in Fig. 19.

The principal difference was a one-third reduction in peak N_e using Ref. 19 rate constants. The experimental data and the TVSL results of Kang and Dunn[19] were taken from Ref. 22. Except for the experimental data between y = 10 and 14 cm, which were affected by probe heating,[22] the use of the Ref. 19 reaction rate constants improved the agreement between the predictions of the present method and the experimental data, at least for y < 10 cm. However, as noted by Evans, Schexnayder and Huber,[22] the experimental data did not support the upswing in N_e near the shock that the Kang and Dunn[19] results gave. The present results also did not show such an upswing, but rather showed the opposite trend.

Heat-transfer distributions are shown in Fig. 20. The present results include boundary-layer (perfect gas[13,14] and seven species nonequilibrium air[15,16]) and viscous shock-layer (perfect gas, dissociating oxygen, and seven species nonequilibrium air) predictions for the RAM C 9° sphere-cone and seven specie TVSL predictions for a 9° half-angle hyperboloid. All of the present results were in good agreement for this case. Some differences due to chemistry and geometry did exist, but the agreement was good despite the diversity of methods, chemistry and geometry.

The heat-transfer rates at the stagnation point are not clearly shown in Fig. 20 but are given in Table IX. The present results for TVSL, seven species, 1st iteration were obtained using the method of Ref. 16. The present results showed some distinct differences but agreed reasonably well, at least compared with the results of Kang.

In Refs. 18-21, Kang and Dunn presented temperature profiles, heat transfer rates, shock temperature and shock-layer thickness distributions for the RAM C reentry body only at 230 Kft. However, predictions of electron concentration

profiles for s = 8.8 were given for 250, 265 and 275 Kft as well as for 230 Kft. In Ref. 21, Kang and Dunn noted that at 230 Kft the electron concentration profiles predicted with a single ionizing species (seven total species) and with five ionizing species (eleven total species) were essentially the same, but that at 275 Kft the five ionizing species chemistry model predicted electron concentrations an order of magnitude higher than the single ionizing species (NO^+) model. For these two altitudes they gave N_e profiles predicted with both 7 and 11 species, but at 250 and 265 Kft they presented N_e profiles predicted with the 11 species model only.

In Figs. 21 and 22, electron concentration profiles predicted by the present method are compared with the experimental data (from Ref. 22) and the results of Kang and Dunn[18-21]. The present results are for a single ionizing species (7 species total). In Fig. 21 the present results are for no shock slip (NSS) and the results of Kang and Dunn are for 7 species. In Fig. 22, the present results are for shock slip (SS) and the results of Kang and Dunn are for 11 species.

Comparing the present predictions without shock slip with Kang and Dunn's predictions with shock slip, Fig. 21, the present predictions agreed reasonably well as to level of ionization with the predictions of Kang and Dunn[18-21] with the NO^+ only model. The agreement between the present predictions and the experimental data was reasonably good at 230, 250 and 265 Kft, but at 275 Kft the present method, without shock slip, significantly underpredicted N_e. In contrast, the present predictions of electron concentration profiles, when shock slip was included, as shown in Fig. 22, agreed quite well with the experimental data, even at 275 Kft. Without shock slip, the species concentrations behind the shock were the same as in the free stream and thus

$C_{NO^+} = C_{e^-} = 0$. With shock slip, however, a finite concentration of NO^+ and thus e^- was permitted behind the shock and diffusion carried the ions to the shock zone. While the electron density at the shock was quite low with shock slip, the nonzero value of C_{NO^+} behind the shock raised the electron density profile, especially at the higher altitudes. Also at 275 Kft, with shock slip a thicker viscous shock layer was predicted, as was an increased static temperature and a decreased density distribution from the maximum values in the layer to the shock. Thus the present method predicted an increased ionization due to the higher temperature and decreased deionization due to the lower density.

Further, the present predictions showed correctly two trends not shown by the predictions of Kang and Dunn:[18-21] (i) the viscous-layer thickness increased with altitude, and (ii) the present predictions showed that the peak of the electron concentration profile occurred within the viscous layer and not at the shock. In Ref. 21, the explanation given by Kang and Dunn for the peak of the N_e profile occurring at the shock was that the temperature immediately behind the shock was quite low, with an accompanying high density. Thus, it was reasonable for the peak electron concentration to occur at the shock since, with shock slip, there was a finite electron concentration at the shock. If this were modified to state that the peak occurred near tne shock, this would appear to be reasonable. In fact, such results were indicated by the present predictions at 265 and 275 Kft. However, it does not appear reasonable that the electron concentration profiles would show a peak at the shock, or such a strong upswing toward the shock as predicted by Kang and Dunn.[18-21]

In the preceding discussion, the differences between the present results and the results of Kang and Dunn[18-21] were only briefly mentioned. In Refs. 18-21, a large number of results were presented but comparisons were made with

no other numerical results, and the only experimental results with which comparisons were made were for electron concentration profiles. As mentioned above, their results apparently agreed well with the N_e profiles but as Evans, Schexnayder and Huber[22] noted the experimental data did not support the upswing in the N_e profile near the shock as obtained by Kang and Dunn. It was also observed in Ref. 22 that the method of Kang and Dunn overpredicted the N_e values measured by the microwave reflectometers on the RAM C-II at the more forward body stations ($s \simeq 0.8$ and 2.1) by factors as large as 20; whereas for 233 Kft and lower, the results of the boundary-layer theory used in Ref. 22 agreed with the reflectometer data at all body stations. These two notes from Ref. 22 raise questions about the results given in Refs. 18-21. Further questions must be raised by the differences between the results from Refs. 18-21 and the present results.

As mentioned above the emphasis of the present work was on predicting the hypersonic viscous flowfield over nonanalytic blunt bodies including spherically blunted cones with electron concentration profiles only a part of the flowfield predictions. Since electron concentration profiles are subject to changes in reaction rate constants as well as changes in temperature profiles, mean flowfield quantities such as heat-transfer distributions would be a more reliable measure of method accuracy. For example, predictions for the RAM C at 230 Kft were also made with the reaction equations and rate constants from Blottner[29] (Table VII). Predictions of heat-transfer rates were only slightly affected, but the predictions of the electron concentrations were an order of magnitude lower than when other rate data (Tables V, VI and VIII) were used. Since there were no experimental data for y_{sh} or St distributions, calculations were made using well known, well established, independent methods (inviscid flowfield

technique of Ref. 1 and boundary-layer flows from Refs. 13-16). The predictions of the present viscous shock-layer methods agreed well with the results of these independent methods. In contrast, there were large differences between the present predictions and the results of Kang and Dunn.[18-21]

The value of T_{sh} at s = 0 obtained by Kang and Dunn as shown in Fig. 14 was nearly the same as for the present results, but for s > 1 their values of T_{sh} were distinctly lower than the present T_{sh} values. For s > 80 their value of T_{sh} was only about 60% of the present values. The distributions of T_{sh} obtained by Kang and Dunn should imply a lower shock angle (for s > 5 or 10) than that in the present results. However, the shock-layer thickness distributions shown in Fig. 15 seem to clearly indicate that (for s > 10) the shock angle obtained by Kang and Dunn was considerably greater than that in the present results. In fact, at s ≃ 10 the values of y_{sh} were all approximately unity, but at s = 90 the present results gave y_{sh} ≃ 1.9 for the inviscid flow over the sphere-cone, y_{sh} ≃ 2.2 for the sphere-cone shock-layer flows and y_{sh} ≃ 3.5 for the hyperboloid shock-layer flows; whereas Kang and Dunn's results gave y_{sh} ≃ 9. Thus, the trends of the T_{sh} and y_{sh} distributions from Refs. 18-21 were distinctly contradictory and inconsistent.

The temperature profiles as shown in Figs. 16 and 17 also differed markedly. The profiles of Kang and Dunn were nearly the same shape at s = 10 as at s = 90, while the present profiles showed a strong downstream influence. The present profiles showed a distinct outer inviscid region, somewhat weak at s = 8.8 but quite clear at s = 90. The present profiles showed about the same peak value of T at s = 8.8 and 90. In the profiles from Refs. 18-21, the peak value increased from T ≃ 7200° K at s = 10 to T ≃ 8200° K at s = 90.

With the temperature profiles as different as shown in Fig. 16, differences in electron concentration profiles were expected, but not the differences shown by the profiles in Fig. 19. The present results gave a peak value of N_e at $y \simeq 5$ cm while the peak of the temperature profile was at $y \simeq 3.5$ cm, but T at $y = 5$ cm was only slightly lower than T at $y = 3.5$ cm. This was quite reasonable, but in the results of Kang and Dunn, the peak value of N_e was at the shock ($y \simeq 17$ cm) while the peak value of T was at $y = 9$ cm. Further, T at the shock, where the peak in N_e occurred, was less than one-eighth of the peak temperature. Also, while the N_e profile of Kang and Dunn apparently agreed well with the experimental data, the peak value of N_e was two or three times the peak of the experimental data (points affected by probe heating excluded), twice the peak of the present results and three times the peak obtained by Evans, Schexnayder and Huber.[22]

At the stagnation point, the heat transfer obtained by Kang and Dunn was one-half to one-third of that predicted by the finite-difference methods used in the present work (see Table IX). In contrast to the stagnation point results, over most of the conical portion of the body the heat transfer predicted by Kang and Dunn was two to six times that predicted by the boundary-layer and viscous shock-layer methods used in the present work. However, the temperature profiles shown in Figs. 16 and 17 would apparently indicate that the heat transfer obtained by Kang and Dunn should have been lower than the present results.

Ames Experimental Case

A measure of the validity of a theory is the agreement with experimental data. For the shuttle configuration, flight heat-transfer data are some years in the future and, in general, wind-tunnel data for shuttle configurations are not readily available outside of the NASA and some contractors. One set

of experimental hypersonic wind tunnel data which has been published is that of Pappas and Lee[17] at the NASA Ames Research Center for flow over a 7.5° sphere-cone with R_n = 1 in. In the experimental program, surface pressure and heat-transfer distributions were measured at Mach 13 with varying rates of injection of foreign gases. Included in the experimental data were distributions for the no injection case. Experimental and present predictions of pressure and heat-transfer distributions are shown in Fig. 23 and 24. Also shown in these figures is the previous first-order boundary-layer theory of Lewis, Adams and Gilley[15] including transverse curvature and displacement-thickness interaction for the Ames conditions. The results from Ref. 15 were obtained using a global iteration for determining the displacement-thickness interaction effects, and the inviscid body pressure for the effective body was obtained using a blunt body, method of characteristics procedure similar to that of Ref. 1. The present theory did not compare as well with the experimental data as did the previous boundary-layer with viscous interaction included. In the present viscous shock-layer method, the effect of the discontinuity in surface curvature, κ, was most distinct immediately upstream of the sphere-cone tangent point and for a short distance downstream. The sphere-cone considered by Pappas and Lee[17] ended at $s \simeq 5$, and almost all of this body was within the length affected by the discontinuity in κ. Despite the effect of the discontinuity in κ, the agreement between the experimental data and the predictions of the present viscous shock-layer theory was quite good.

While the RAM C, 230 Kft, conditions were quite different from the Ames conditions, the Reynolds numbers were of the same order (Re_∞/R_n = 4315 for the RAM C conditions and Re_∞/R_n = 1515 for the Ames conditions). The shock Reynolds numbers were also similar (RAM C, Re_s = 269; Ames, Re_s = 193) and the values

of the Reynolds number parameter were nearly the same (RAM C, $\epsilon = 0.0965$; Ames, $\epsilon = 0.0980$). The Reynolds number similarity between the two cases should allow comparison of the normalized heat-transfer distributions. Fig. 25 shows the same data as Fig. 24 but with the present results for the RAM C conditions added. The present predictions for the RAM C and Ames conditions were in quite good agreement even though there was a difference in cone angle (and thus in the location of the sphere-cone tangent points). Further, the present viscous shock-layer results for the RAM C conditions agreed well with the Ames experimental data. The results of Kang and Dunn[18-21] for the RAM C are also shown in Fig. 25 in normalized form. Fig. 25 clearly shows that for $s > 3$ the results of Kang and Dunn were higher by an order of magnitude or more than the present results. A comparison of the results of Kang and Dunn for the RAM C with the Ames experimental data showed a difference by a factor of 11 or 12 at $s = 4$ or 4.5. The values of Re_∞/R_n and Re_s given above indicate that the Ames conditions were at least as much in a viscous shock-layer regime as the RAM C, 230 Kft, conditions and it is most surprising that the trend of the results of Kang and Dunn[18-21] did not agree better with the experimental data of Pappas and Lee.[17]

Computing Time Required

Some of the computing times required for the RAM C conditions are given in Table X. These computing times were obtained on the IBM 370/158 system of the Computing Center of the Virginia Polytechnic Institute and State University. The inviscid gas model calculation used the blunt body, method of characteristics technique of Ref. 1. The PG boundary-layer (BL) calculation was made with the method of Refs. 13, 14. The viscous shock-layer (VSL) computing times were for the present method. The inviscid method generated the pressure distribution

for the BL calculation and the initial shock shape for the VSL calculations. In the VSL method, the first global iteration was for $O\text{-}O_2$ and subsequent global iterations were for either $O\text{-}O_2$ or the 7 sp gas model.

The computing time (not shown) for a PG VSL was nearly the same as for the PG BL. As shown, a global iteration for the $O\text{-}O_2$ VSL required about twice the computing time of the PG BL. For $O\text{-}O_2$, when the second global iteration was TVSL, the computing time was almost the same as for the first global iteration. However, when the second iteration was FVSL, the second iteration required three times the computing time of the first iteration when the same value of N was used, and twice the computing time when the step size restriction was relaxed.

For the 7 sp gas model, the step size restriction was relaxed. The TVSL global iteration required six times the computing time required for $O\text{-}O_2$, and for the FVSL global iteration, the computing time was 3.5 to 5 times that required for the $O\text{-}O_2$ global iteration.

These computing times show that if the differences between the results for TVSL and FVSL are not great, a significant amount of computing time can be saved by using the TVSL model. Further, unless the 7 sp model is required, the computing time can be greatly reduced by using the $O\text{-}O_2$ gas model.

CONCLUSIONS

The results of the present finite-difference method for predicting hypersonic viscous shock-layer flows over nonanalytic blunt bodies were compared with predictions of other finite-difference methods and with experimental data. For the windward plane of symmetry of a shuttle orbiter configuration, the predictions of the present method agreed well with the boundary-layer predictions of Tong, Buckingham and Morse. For the low Reynolds number flows over a 20° sphere-cone, a pseudo-shuttle configuration, the predictions of the present method appeared quite reasonable. Also, the altitude effects on the temperature and electron concentration profiles were correctly predicted by the present method as was the "recovery" of a thin boundary layer on the downstream portion of the sphere-cone.

The agreement of the prediction of the present method with experimental data further tends to verify the appropriateness of the present method. For the RAM C, the predictions of the present method agreed well with the experimental electron concentration profiles, with the boundary-layer predictions of Evans, Schexnayder and Huber and with other boundary-layer predictions of heat-transfer rate distributions (for perfect gas and nonequilibrium air). Predictions of the present method also agreed well with the experimental data of Pappas and Lee for pressure and heat-transfer rate distributions.

The present viscous shock-layer method, accurate to second order in the Reynolds number parameter ε, eliminates most of the problems encountered in applying boundary-layer theory to hypersonic, low Reynolds number flows over nonanalytic blunt bodies. The comparisons of predictions of the present method with the results of Kang and Dunn indicate that the present method is clearly superior to the more approximate method of Kang and Dunn.

REFERENCES

[1]Inouye, M., Rakich, J., and Lomax, H., "A Description of Numerical Methods and Computer Programs for Two-Dimensional and Axisymmetric Supersonic Flow over Blunt Nosed and Flared Bodies," NASA TN D-2970, August 1965.

[2]Rizzi, A. W. and Inouye, M., "A Time-Split Finite-Volume Technique for Three-Dimensional Blunt-Body Flow," AIAA Paper 73-133, January 1973.

[3]Kutler, P., Reinhardt, W. A., and Warming, R. F., "Multishocked, Three-Dimensional Supersonic Flowfields with Real Gas Effects," AIAA Journal, Vol. 11, No. 5, May 1973, pp. 657-664.

[4]Blottner, F. G. and Flugge-Lotz, I., "Finite Difference Computation of the Boundary-Layer with Displacement Thickness Interaction," Journal de Mechanique, Vol. 11, No. 4, 1964.

[5]Blottner, F. G., "Finite-Difference Methods of Solution of the Boundary-Layer Equations," AIAA Journal, Vol. 8, No. 2, February 1970, pp. 193-206.

[6]Lewis, Clark H., "First Order Treatment of Higher-Order Boundary-Layer Effects," The Physics of Fluids, Vol. 13, No. 12, December 1970, pp. 2939-2949.

[7]Davis, R. T., "Numerical Solution of the Hypersonic Viscous Shock-Layer Equations," AIAA Journal, Vol. 8, No. 5, May 1970, pp. 843-851.

[8]Davis, R. T., "Hypersonic Flow of a Chemically Reacting Binary Mixture Past a Blunt Body," AIAA Paper No. 70-805, July 1970.

[9]Jain, A. C. and Adimurthy, V., "Hypersonic Merged Stagnation Shock Layers, Part I: Adiabatic Wall Case," AIAA Journal, Vol. 12, No. 3, March 1974, pp. 342-347.

[10]Jain, A. C. and Adimurthy, V., "Hypersonic Merged Stagnation Shock Layers, Part II: Cold Wall Case," AIAA Journal, Vol. 12, No. 3, March 1974, pp. 348-354.

[11]Moss, J. N., "Solutions for Reacting and Nonreacting Viscous Shock Layers with Multicomponent Diffusion and Mass Injection," PhD Dissertation, Virginia Polytechnic Institute and State University, Blacksburg, Virginia, October 1971.

[12]Tong, H., Buckingham, A. C., and Morse, H. L., "Nonequilibrium Chemistry Boundary Layer Integral Matrix Procedure," Aerotherm Final Report No. 73-67, July 1973.

[13]Anderson, E. C. and Lewis, C. H., "Laminar or Turbulent Boundary-Layer Flows of Perfect Gases or Reacting Gas Mixtures in Chemical Equilibrium," NASA CR-1893, 1971.

[14]Lewis, C. H., Anderson, E. C., and Miner, E. W., "Nonreacting and Equilibrium Chemically Reacting Turbulent Boundary-Layer Flows," AIAA Paper No. 71-597, June 1971.

[15]Lewis, C. H., Adams, J. C. and Gilley, G. E., "Effects of Mass Transfer and Chemical Nonequilibrium on Slender Blunted Cone Pressure and Heat Transfer Distributions at M_∞ = 13.2," AEDC TR-68-214, December 1968.

[16]Lewis, C. H. and Miner, E. W., "Stagnation Point Viscous Layers with Mass Transfer," Computers and Fluids, to be published, 1974.

[17]Pappas, C. C. and Lee, G., "Heat Transfer and Pressure on a Hypersonic Blunt Cone with Mass Addition," AIAA Journal, Vol. 8, No. 5, May 1970, pp. 954-956.

[18]Kang, S.-W. and Dunn, M. G., "Hypersonic Viscous Shock Layer with Chemical Nonequilibrium for Spherically Blunted Cones," AIAA Journal, Vol. 10, No. 10, October 1972, pp. 1361-1362.

[19]Kang, S.-W., Jones, W. L., and Dunn, M. G., "Theoretical and Measured Electron-Density Distributions at High Altitudes," AIAA Journal, Vol. 11, No. 2, February 1973, pp. 141-149.

[20]Kang, S.-W. and Dunn, M. G., "Hypersonic Viscous Shock Layer with Chemical Nonequilibrium for Spherically Blunted Cones," Cornell Aeronautical Laboratory Technical Report AF-3093-A-1, February 1972.

[21]Dunn, M. G. and Kang, S.-W., "Theoretical and Experimental Studies of Reentry Plasmas," NASA CR-2232, April 1973.

[22]Evans, J. S., Schexnayder, C. J., Jr., and Huber, P. W., "Boundary-Layer Electron Profiles for Entry of a Blunt Slender Body at High Altitudes," NASA TN D-7332, July 1973.

[23]Bird, R. B., Stewart, W. E., and Lightfoot, E. N., Transport Phenomena, John Wiley and Sons, Inc., 1960.

[24]Williams, F., Combustion Theory, Addison Wesley Book Co., Inc., 1965.

[25]Cheng, H. K., "The Blunt-Body Problem in Hypersonic Flow at Low Reynolds Number," IAS Paper No. 63-92, January 1963, also Cornell Aeronautical Laboratory Report No. AF-1285-A-10, June 1963.

[26]Browne, W. G., "Thermodynamic Properties of Some Atoms and Atomic Ions," MSD Engineering Physics TM2, General Electric Co., Philadelphia, Pa.

[27]Browne, W. G., "Thermodynamic Properties of Some Diatomic and Linear Polyatomic Molecules," MSD Engineering Physics TM3, General Electric Co., Philadelphia, Pa.

[28]Browne, W. G., "Thermodynamic Properties of Some Diatoms and Diatomic Ions at High Temperature," MSD Advanced Aerospace Physics TM8, General Electric Co., Philadelphia, Pa., May 1962.

[29]Blottner, F. G., "Non-Equilibrium Laminar Boundary Layer Flow of Ionized Air," General Electric Report R64SD56, November 1964.

[30]Blottner, F. G., Johnson, Margaret, and Ellis, Molly, "Chemically Reacting Viscous Flow Program for Multi-Component Gas Mixtures," Sandia Laboratories Report SC-RR-70-754, December 1971.

[31]Richtmyer, R. D., Difference Methods for Initial-Value Problems, Interscience Publishers, Inc., New York, 1957.

[32]Conte, S. D., Elementary Numerical Analysis, McGraw-Hill Book Co., Inc., New York, 1965.

[33]Carnahan, B., Luther, H. A., and Wilkes, J. O., Applied Numerical Methods, John Wiley & Sons, Inc., New York, 1969.

[34]Huber, P. W., Evans, J. S., and Schexnayder, C. J., Jr., "Comparison of Theoretical and Flight-Measured Ionization on a Blunt Body Re-Entry Flow-Field," AIAA Journal, Vol. 9, No. 6, June 1971, pp. 1154-1162.

TABLE I. Species Enthalpy vs. Temperature

$$h_i^* = \hat{h}_i T + \Delta h_i^F \qquad (ft^2/sec^2)$$

T, degrees Rankine

Δh_i^F from Table III

		$\hat{h}_i$ for species					
	T, °R	O	O_2	NO	N	NO^+	N_2
1	180	8253.7150	5442.2804	5803.4430	8879.4515	5803.3429	6215.9735
2	900	8279.5492	5525.2752	5846.3268	8879.4515	5817.9601	6232.1483
3	1260	8172.0972	5660.1810	5946.0192	8879.4515	5871.1144	6290.1901
4	2700	7984.1695	6144.7635	6414.0538	8879.4515	6255.8007	6704.0158
5	4140	7916.9475	6446.8247	6711.5374	8880.0949	6558.1401	7026.3598
6	5400	7891.3480	6651.0805	6878.1170	8887.6193	6737.5431	7216.7672
7	6660	7887.3735	6823.2823	6996.7650	8917.7885	6867.6546	7354.3427
8	8100	7904.8362	6987.3082	7097.7506	9000.4143	6979.1693	7471.3913
9	9540	7939.3705	7158.7746	7176.0428	9143.0924	7067.1563	7561.1930
10	10800	7978.0200	7284.8942	7258.5483	9311.8291	7134.6858	7625.3472
11	12060	8020.3155	7413.3062	7333.6368	9509.9128	7200.9305	7681.0745
12	13500	8069.3863	7533.8005	7417.0683	9755.3236	7283.2524	7739.7418
13	14760	8110.8055	7630.3696	7500.7502	9973.1209	7367.0678	7791.0723
14	16200	8155.0256	7730.7020	7578.5335	10212.8660	7481.7195	7854.8066
15	17460	8190.5613	7809.6284	7647.9069	10407.6790	7601.3354	7918.0698
16	18900	8227.8026	7889.6737	7727.8677	10608.9441	7746.6231	8041.8449
17	20250	8260.2088	7954.9242	7802.8644	10776.3045	7930.1726	8176.7842
18	21600	8291.5039	8011.0991	7877.2186	10924.9701	8184.6306	8335.0296
19	22950	8323.3312	8058.3548	7950.2963	11058.6940	8401.0605	8487.0016
20	24300	8357.7872	8097.2391	8021.5219	11182.4986	8629.6631	8655.8186

TABLE I. Concluded

	T, °R	O	O_2	NO	N	NO^+	N_2
21	25650	8397.2347	8128.1431	8090.3529	11302.1209	8863.6887	8839.0322
22	27000	8444.2088	8151.5362	8156.3056	11423.5663	9097.2137	9033.2465
23	28800	8523.2135	8171.8781	8239.0113	11598.3975	9398.9023	9302.5889
24	30600	8626.5659	8180.9537	8314.8840	11799.3230	9680.5674	9574.7909
25	32400	8759.8208	8179.8584	8383.2062	12036.1549	9935.0337	9840.4694
26	34200	8927.4222	8169.9221	8443.2769	12315.2200	10158.2132	10091.5815
27	36000	9132.1710	8152.0839	8494.9211	12638.8777	10348.1870	10321.8719
28	37800	9375.0216	8127.5954	8537.8049	13005.4121	10505.2886	10527.1405
29	39600	9654.7850	8097.3955	8572.0953	13409.3899	10631.1035	10704.9744
30	41400	9968.2845	8062.4232	8598.0425	13842.3752	10728.0510	10854.8374
31	43200	10310.4505	8023.4607	8615.9803	14293.8767	10798.9678	10977.1764
32	46800	11053.8208	7936.6947	8629.8299	15206.6739	10874.6403	11145.8058
33	50400	11824.5587	7841.8703	8618.1495	16062.0996	10880.8142	11227.7524
34	54000	12563.4851	7742.7897	8585.8615	16797.8135	10836.7624	11241.8719
35	57600	13225.1280	7642.0818	8537.4712	17382.6457	10757.4189	11205.6795
36	61200	13782.8239	7541.6399	8477.1501	17812.2173	10654.2140	11133.2949
37	64800	14227.4190	7442.7706	8408.0688	18099.3789	10535.5743	11035.8884
38	68400	14562.5905	7346.3110	8333.1472	18265.5955	10407.5068	10921.7709
39	72000	14799.5264	7252.8244	8254.4378	18333.8694	10274.2666	10797.2872
40	75600	14952.7007	7162.6239	8173.6177	18326.1841	10139.1074	10666.8161
41	79200	15037.0881	7075.8580	8091.9715	18261.1273	10004.0317	10533.6641
42	82800	15066.4587	6992.5815	8010.4255	18153.8908	9870.7080	10400.1546
43	86400	15052.8453	6912.7631	7929.7054	18016.8067	9740.0541	10267.8069
44	90000	15006.2311	6836.3168	7850.2952	17858.7580	9612.8209	10137.7826
45	93600	14934.7842	6763.1330	7772.5703	17687.1617	9489.3422	10010.8861
46	97200	14844.9983	6693.0787	7696.7644	17507.2367	9370.0350	9887.4747
47	100800	14741.9589	6626.0131	7623.0359	17322.9865	9254.8160	9767.9953
48	104400	14629.7030	6561.7875	7551.4766	17137.3422	9143.8520	9652.4480
49	108000	14511.3133	6500.2534	7482.1283	16952.4486	9037.0595	9541.0114

TABLE II. Species Specific Heat vs. Temperature

$C^*_{p_i} = \hat{C}_{p_i}$ $(ft^2/sec^2 - °R)$

		$\hat{C}_{p_i}$					
	T, °R	O	O_2	NO	N	NO^+	N_2
1	180	8865.3169	5442.7811	5803.8852	8879.4515	5803.6766	6216.3309
2	900	7950.1986	5814.0594	6030.5605	8879.4515	5896.1522	6318.1788
3	1260	7868.9876	6167.5933	6361.4418	8879.4515	6127.5163	6568.8978
4	2700	7796.0385	6834.3139	7129.7633	8879.4872	6944.8038	7440.7753
5	4140	7792.0953	7184.2332	7370.9974	8887.1546	7257.4220	7769.8127
6	5400	7830.4789	7451.9948	7471.0319	8955.1247	7384.2297	7901.8298
7	6660	7917.7612	7675.1452	7535.8332	9168.7220	7461.1870	7980.4610
8	8100	8057.9010	7911.7368	7591.7824	9633.8246	7527.2815	8041.6394
9	9540	8208.7282	8126.5783	7659.0200	10278.6199	7600.9015	8090.1014
10	10800	8329.9344	8314.4277	7767.4810	10902.3968	7698.2745	8132.9423
11	12060	8432.3479	8469.6518	7910.9834	11504.0473	7850.0115	8187.6062
12	13500	8523.6360	8612.5144	8128.3143	12095.9213	8112.6792	8281.8313
13	14760	8582.5962	8713.6761	8292.5494	12498.1476	8431.8468	8408.3793
14	16200	8631.0724	8798.8772	8465.2194	12818.6776	8899.7311	8660.2422
15	17460	8662.8683	8845.8200	8614.3117	12990.8101	9390.1420	9024.8463
16	18900	8695.9943	8869.3696	8779.1725	13094.5971	10078.4526	9507.8574
17	20250	8734.2839	8864.7536	8924.5937	13139.0109	10776.8585	10049.9380
18	21600	8791.4446	8837.2921	9058.3346	13171.9683	11526.9919	10622.5810
19	22950	8880.5107	8789.4104	9178.4761	13232.1637	12212.5493	11220.2458
20	24300	9015.3460	8723.6905	9283.5999	13355.5036	12815.0088	11833.7281

TABLE II. Concluded

	T, °R	O	O_2	NO	N	NO^+	N_2
21	25650	9209.8769	8642.3230	9372.3711	13573.2473	13323.2740	12436.1292
22	27000	9477.1848	8547.4986	9443.6217	13910.3274	13726.8326	13002.2486
23	28800	9966.0626	8404.0884	9509.9498	14574.1929	14088.8423	13660.8595
24	30600	10623.3242	8245.7347	9542.1544	15496.9631	14253.8700	14172.1096
25	32400	11456.3865	8077.2101	9540.2354	16666.0556	14242.2730	14513.4792
26	34200	12458.6462	7902.6612	9505.4445	18040.2200	14084.9210	14681.5724
27	36000	13608.5253	7725.9138	9440.3678	19552.9698	13816.1879	14688.0066
28	37800	14870.1596	7549.9331	9348.4262	21120.5889	13468.9456	14554.9440
29	39600	16196.0429	7377.1602	9233.7912	22651.5689	13071.5609	14309.8192
30	41400	17530.7827	7209.3945	9100.8847	24056.9034	12646.8941	13980.7818
31	43200	18816.8585	7047.9348	8953.8782	25260.9907	12212.3824	13594.0154
32	46800	21031.7755	6746.9846	8633.4175	26867.2150	11360.6293	12733.1743
33	50400	22518.4535	6477.3688	8299.1572	27309.2081	10575.3712	11857.1414
34	54000	23158.5966	6238.6647	7970.0195	26742.2844	9878.3837	11036.8714
35	57600	23025.5921	6028.6740	7657.7268	25481.0043	9271.6692	10302.9268
36	61200	22307.0545	5844.3923	7368.5696	23851.9029	8748.6365	9662.4567
37	64800	21220.0161	5682.6665	7105.0676	22109.6670	8299.3824	9110.9036
38	68400	19954.5951	5540.4690	6867.3626	20420.1558	7913.5864	8638.6697
39	72000	18650.2116	5415.0536	6654.2450	18872.1967	7581.7039	8235.0047
40	75600	17396.0569	5304.0104	6463.7873	17502.7149	7295.3333	7889.5155
41	79200	16240.6385	5205.2741	6293.7871	16316.8220	7047.3079	7592.9439
42	82800	15205.4875	5117.0529	6142.0167	15302.9187	6831.5955	7337.3546
43	86400	14294.0308	5037.8605	6006.3486	14442.1133	6643.1653	7116.0900
44	90000	13500.3379	4966.4057	5884.8222	13713.6378	6477.8456	6923.6004
45	93600	12813.6432	4901.6247	5775.6936	13097.4925	6332.1657	6755.3106
46	97200	12221.5069	4842.6020	5677.4196	12575.7154	6203.2388	6607.4493
47	100800	11711.5361	4788.5708	5588.6317	12132.8286	6088.6622	6476.9067
48	104400	11272.1204	4738.8741	5508.1536	11755.7135	5986.4168	6361.0913
49	108000	10892.9479	4692.9562	5434.9674	11433.4142	5894.8340	6257.8761

TABLE III. Species Heats of Formation and Molecular Weights

Species	Δh_i^F (ft^2/sec^2)	H^* (Kcal/mole)	M_i
O	1.661×10^8	58.9725	16.000
O_2	0	0	32.000
NO	3.225×10^7	21.477	30.008
N	3.619×10^8	112.507	14.008
NO^+	3.5341	235.836	30.008
N_2	0	0	28.016

$$\Delta h_i^F = \frac{10.388 \times 10^8}{23.053\ M_i}\ H^*$$

TABLE IV. Species Viscosity Curve Fit Constants

$$\mu_i^* = \exp C_i T_k (A_i \ln T_k + B_i) \quad \text{(gm/cm-sec)}$$

T_k, degrees Kelvin

Species	A_i	B_i	C_i
O	0.019558	0.438511	-11.6235
O_2	0.038271	0.021076	- 9.5989
NO	0.042501	-0.018874	- 9.6197
N	0.0085863	0.6463	-12.581
NO^+	0.042501	-0.018874	- 9.6197
N_2	0.048349	-0.022485	- 9.9827

TABLE V. Reaction Equations and Reaction Rate Constants from Evans, Schexnayder and Huber (Ref. 22)

Reaction Equations	
r = 1	$O_2 + M_1 \rightleftarrows 2O + M_1$
2	$O_2 + O_2 \rightleftarrows 2O + O_2$
3	$O_2 + N_2 \rightleftarrows 2O + N_2$
4	$O_2 + O \rightleftarrows 2O + O$
5	$N_2 + M_2 \rightleftarrows 2N + M_2$
6	$N_2 + N \rightleftarrows 2N + N$
7	$N_2 + N_2 \rightleftarrows 2N + N_2$
8	$NO + M_3 \rightleftarrows N + O + M_3$
9	$NO + M_4 \rightleftarrows N + O + M_4$
10	$NO + O \rightleftarrows O_2 + N$
11	$N_2 + O \rightleftarrows NO + N$
12	$N + O \rightleftarrows NO^+ + e^-$

Matrix of Catalytic Third Bodies; $Z_{(j-ns),i}$

		O	O_2	NO	N	NO^+	N_2
		i=1	2	3	4	5	6
(j-ns) = 1	M_1	0	0	1	1	0	0
2	M_2	1	1	1	0	0	0
3	M_3	0	1	0	0	0	1
4	M_4	1	0	1	1	0	0
5	e^-	0	0	0	0	1	0

TABLE V. Concluded

Reaction Rate Constants

T_k degrees Kelvin

$$k_{f_r} = T_k^{C2_r} \exp (CO_r - C1_r/T_k)$$

$$k_{b_r} = T_k^{D2_r} \exp (DO_r - D1_r/T_k)$$

Reaction No.	CO_r	$\exp (CO_r)$	$C1_r$	$C2_r$	DO_r	$\exp (DO_r)$	$D1_r$	$D2_r$
r = 1	42.7275	3.6×10^{18}	59,400	-1	35.6374	3.0×10^{15}	0	-1/2
2	44.9430	3.3×10^{19}	59,400	-1	37.8346	2.7×10^{16}	0	-1/2
3	43.4206	7.2×10^{18}	59,400	-1	36.3305	6.0×10^{15}	0	-1/2
4	45.9463	9.0×10^{19}	59,400	-1	38.8563	7.5×10^{16}	0	-1/2
5	39.7858	1.9×10^{17}	113,100	-1/2	36.9367	1.1×10^{16}	0	-1/2
6	51.3988	2.1×10^{22}	113,100	-3/2	48.5366	1.2×10^{21}	0	-3/2
7	40.7126	4.8×10^{17}	113,100	-1/2	37.8346	2.7×10^{16}	0	-1/2
8	47.4380	4.0×10^{20}	75,600	-3/2	46.0517	1.0×10^{20}	0	-3/2
9	50.4211	7.9×10^{21}	75,600	-3/2	49.0474	2.0×10^{21}	0	-3/2
10	21.8864	3.2×10^{9}	19,700	1	27.5902	9.6×10^{11}	3600	1/2
11	31.8505	6.8×10^{13}	37,500	0	30.3391	1.5×10^{13}	0	0
12	23.9013	2.4×10^{10}	32,400	1/2	47.4380	4.0×10^{20}	0	-1/2

TABLE VI. Reaction Equations and Reaction Rate Constants from Kang and Dunn (Ref. 21)

	Reaction Equations
r = 1	$O_2 + M_1 \rightleftarrows 2O + M_1$
2	$O_2 + O_2 \rightleftarrows 2O + O_2$
3	$O_2 + N_2 \rightleftarrows 2O + N_2$
4	$O_2 + O \rightleftarrows 2O + O$
5	$N_2 + M_2 \rightleftarrows 2N + M_2$
6	$N_2 + N \rightleftarrows 2N + N$
7	$N_2 + N_2 \rightleftarrows 2N + N_2$
8	$NO + M_3 \rightleftarrows N + O + M_3$
9	$NO + M_4 \rightleftarrows N + O + M_4$
10	$NO + O \rightleftarrows O_2 + N$
11	$N_2 + O \rightleftarrows NO + N$
12	$N + O \rightleftarrows NO^+ + e^-$

Matrix of Catalytic Third Bodies; $Z_{(j\text{-}ns),\, i}$

		O	O_2	NO	N	NO^+	N_2
		i=1	2	3	4	5	6
(j-ns) = 1	M_1	0	0	1	1	0	0
2	M_2	1	1	1	0	0	0
3	M_3	0	1	0	0	0	1
4	M_4	1	0	1	1	0	0
5	e^-	0	0	0	0	1	0

TABLE VI. Concluded

Reaction Rate Constants

T_k degrees Kelvin

$$k_{f_r} = T_k^{C2_r} \exp (CO_r - C1_r/T_k)$$

$$k_{b_r} = T_k^{D2_r} \exp (DO_r - D1_r/T_k)$$

Reaction No.	CO_r	exp (CO_r)	$C1_r$	$C2_r$	DO_r	exp (DO_r)	$D1_r$	$D2_r$
r = 1	42.7275	3.6×10^{18}	59,500	-1	35.6374	3.0×10^{15}	0	-1/2
2	44.9247	3.24×10^{19}	59,500	-1	37.8346	2.7×10^{16}	0	-1/2
3	43.4206	7.2×10^{18}	59,500	-1	36.3305	6.0×10^{15}	0	-1/2
4	45.9463	9.0×10^{19}	59,500	-1	38.8563	7.5×10^{16}	0	-1/2
5	39.7858	1.9×10^{17}	113,000	-1/2	36.9367	1.1×10^{16}	0	-1/2
6	52.0642	4.085×10^{22}	113,000	-3/2	49.1741	2.27×10^{21}	0	-3/2
7	40.6915	4.7×10^{17}	113,000	-1/2	37.8420	2.72×10^{16}	0	-1/2
8	47.4127	3.9×10^{20}	75,500	-3/2	46.0517	1.0×10^{20}	0	-3/2
9	48.1058	7.8×10^{20}	75,500	-3/2	46.7448	2.0×10^{20}	0	-3/2
10	21.8864	3.2×10^{9}	19,700	1	23.2882	1.3×10^{10}	3580	1
11	31.8795	7.0×10^{13}	38,000	0	30.3783	1.56×10^{13}	0	0
12	14.1520	1.4×10^{6}	31,900	3/2	50.2564	6.7×10^{21}	0	-3/2

TABLE VII. Reaction Equations and Reaction Rate Constants from Blottner (Ref. 29)

Reaction Equations						
r = 1	$O_2 + O_2$	$\rightleftarrows$	$2O + O_2$			
2	$O_2 + O$	$\rightleftarrows$	$2O + O$			
3	$O_2 + M_1$	$\rightleftarrows$	$2O + M_1$			
4	$N_2 + N_2$	$\rightleftarrows$	$2N + N_2$			
5	$N_2 + N$	$\rightleftarrows$	$2N + N$			
6	$N_2 + M_2$	$\rightleftarrows$	$2N + M_2$			
7	$NO + M_3$	$\rightleftarrows$	$N + O$	$+ M_3$		
8	$NO + O$	$\rightleftarrows$	$O_2 + N$			
9	$N_2 + O$	$\rightleftarrows$	$NO + N$			
10	$N_2 + O_2$	$\rightleftarrows$	$2NO$			
11	$N + O$	$\rightleftarrows$	$NO^+ + e^-$			

Matrix of Catalytic Third Bodies; $Z_{(j-ns),i}$

		O	O_2	NO	N	NO^+	N_2
		i-1	2	3	4	5	6
(j-ns) = 1	M_1	0	0	1	1	0	1
2	M_2	1	1	1	0	0	0
3	M_3	1	1	0	1	0	1
4	M_4	0	0	0	0	1	0

TABLE VII. Concluded

Reaction Rate Constants

T_k degrees Kelvin

$$k_{f_r} = T_k^{C2_r} \exp (CO_r - C1_r/T_k)$$

$$k_{b_r} = T_k^{D2_r} \exp (DO_r - D1_r/T_k)$$

Reaction No.	CO_r	exp (CO_r)	$C1_r$	$C2_r$	DO_r	exp (DO_r)	$D1_r$	$D2_r$
r = 1	44.5820	2.3×10^{19}	59,400	-1	37.4832	1.9×10^{16}	0	-1/2
2	45.8892	8.5×10^{19}	59,400	-1	38.8015	7.1×10^{16}	0	-1/2
3	42.5451	3.0×10^{18}	59,400	-1	35.4551	2.5×10^{15}	0	-1/2
4	45.0841	3.8×10^{19}	113,200	-1	42.1397	2.0×10^{18}	0	-1
5	46.3141	1.3×10^{20}	113,200	-1	43.3924	7.0×10^{18}	0	-1
6	44.3910	1.9×10^{19}	113,200	-1	41.4465	1.0×10^{18}	0	-1
7	40.0194	2.4×10^{17}	75,500	-1/2	38.6331	6.0×10^{16}	0	-1/2
8	17.5767	4.3×10^{7}	19,100	-3/2	19.0085	1.8×10^{8}	3020	-3/2
9	31.8505	6.8×10^{13}	37,750	0	30.3391	1.5×10^{13}	0	0
10	32.9593	2.0×10^{14}	61,600	0	30.3391	1.5×10^{13}	40,000	0
11	18.6830	1.3×10^{8}	31,900	1	44.4423	2.0×10^{19}	0	0

TABLE VIII. Reaction Equations and Reaction Rate Constants from Blottner (Ref. 30)

Reaction Equations						
r = 1	$O_2 + M_1$	$\rightleftarrows$	$2O + M_1$			
2	$N_2 + M_2$	$\rightleftarrows$	$2N + M_2$			
3	$N_2 + N$	$\rightleftarrows$	$2N + N$			
4	$NO + M_3$	$\rightleftarrows$	$N + O$	$+ M_3$		
5	$NO + O$	$\rightleftarrows$	$O_2 + N$			
6	$N_2 + O$	$\rightleftarrows$	$NO + N$			
7	$N + O$	$\rightleftarrows$	$NO^+ + e^-$			

Catalytic Third Bodies Efficiencies Relative to Argon; $Z_{(j-ns),i}$

		O	O_2	NO	N	NO^+	N_2
		i=1	2	3	4	5	6
(j-ns) = 1	M_1	25	9	1	1	0	2
2	M_2	1	1	1	0	0	2.5
3	M_3	20	1	20	20	0	1
4	e^-	0	0	0	0	1	0

TABLE VIII. Concluded

Reaction Rate Constants

T_k degrees Kelvin

$$k_{f_r} = T_k^{C2_r} \exp (CO_r - C1_r/T_k)$$

$$k_{b_r} = T_k^{D2_r} \exp (DO_r - D1_r/T_k)$$

Reaction No.	CO_r	$\exp (CO_r)$	$C1_r$	$C2_r$	DO_r	$\exp (DO_r)$	$D1_r$	$D2_r$
r = 1	42.7302	3.61×10^{18}	59,400	-1	35.6407	3.01×10^{15}	0	-1/2
2	39.7963	1.92×10^{17}	113,100	-1/2	36.9275	1.09×10^{16}	0	-1/2
3	52.0800	4.15×10^{22}	113,100	-3/2	49.1959	2.32×10^{21}	0	-3/2
4	47.4305	3.97×10^{20}	75,600	-3/2	46.0617	1.01×10^{20}	0	-3/2
5	21.8801	3.18×10^{9}	19,700	1	27.5933	9.63×10^{11}	3600	1/2
6	31.8431	6.75×10^{13}	37,500	0	30.3391	1.50×10^{13}	0	0
7	22.9238	9.03×10^{9}	32,400	1/2	44.3369	1.80×10^{19}	0	-1

TABLE IX. Stagnation Heat Transfer for

9° Sphere-Cone, R_n = 6 in., RAM C Conditions, 230 Kft

Model	Gas	Iter	Wall	Shock	$\dot{q}$, BTU/ft^2-sec
			Present Results		
BL	PG	---	---	---	231.074
BL	7 sp	---	ECW	---	177.250
FVSL	PG	3	---	SS	123.973
FVSL	O-O_2	3	ECW	SS	238.742
TVSL	O-O_2	2	ECW	NSS	190.278
TVSL	7 sp	2	ECW	NSS	156.883
TVSL	7 sp	1	ECW	SS	252.539
			Kang Results		
TVSL	11 sp	---	ECW	SS	87.772

Table X. Computing Times for RAM C

Sphere-Cone to $s/R_n = 120$[a]

Global Iteration Number[b]	Gas Model	Viscous Model	No. of Stations	No. of Iteractions[c]	N[d]	Computing Time[e] Min:sec
-	PG	Inviscid	--	---	-	5:35
-	PG	BL	61	189	3	1:34
1st	$O-O_2$	TVSL	52	271	3	3:29
2nd	$O-O_2$	TVSL	58	291	3	3:34
2nd	$O-O_2$	FVSL	100	715	3	10:00
2nd	$O-O_2$	FVSL	62	474	4	6:58
2nd	7 sp	TVSL	42	241	4	20:40
2nd	7 sp	FVSL	57	415	4	35:45

[a]Convergence test of 1% for velocity, temperature and species profiles at each grid point.

[b]Data are for the indicated global iteration only.

[c]Total number of station iterations for the global iteration.

[d]The s step size was doubled if a converged solution was obtained with the number of station iterations $\leq$ N.

[e]Execution time; IBM 370/158.

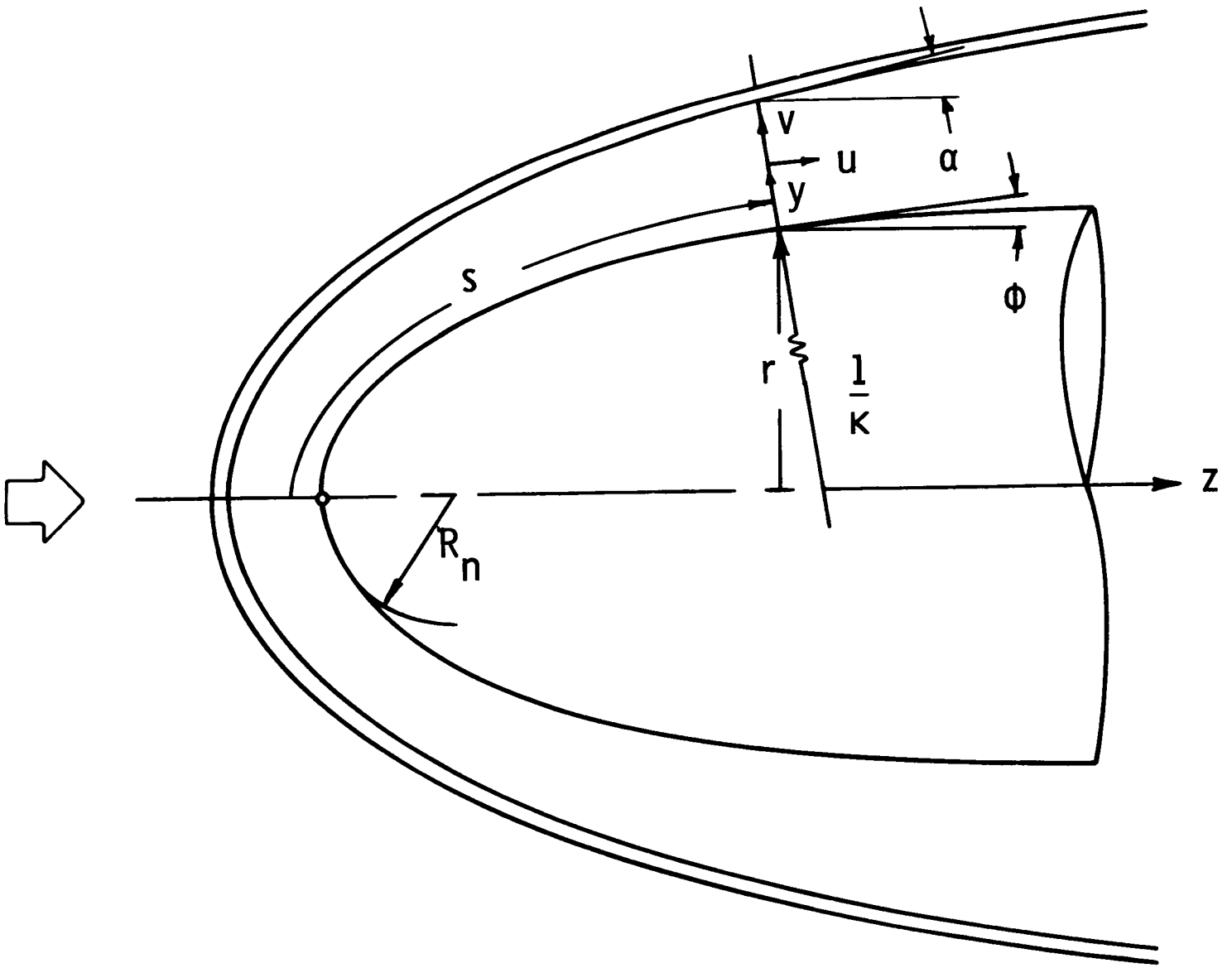

Figure 1. Coordinate System for Viscous Shock-Layer Over Blunt Bodies

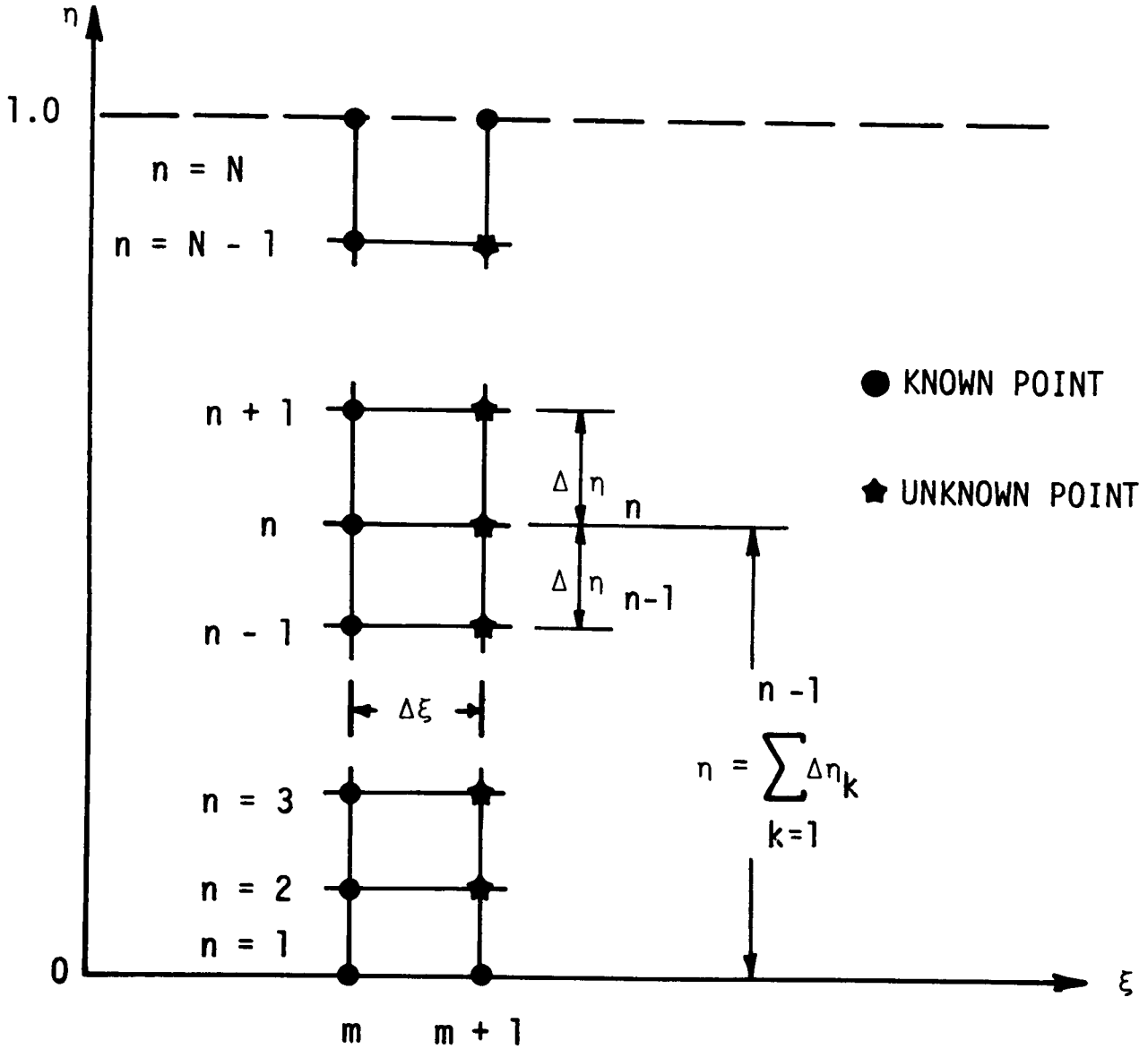

Figure 2. Schematic of Finite-Difference Grid System

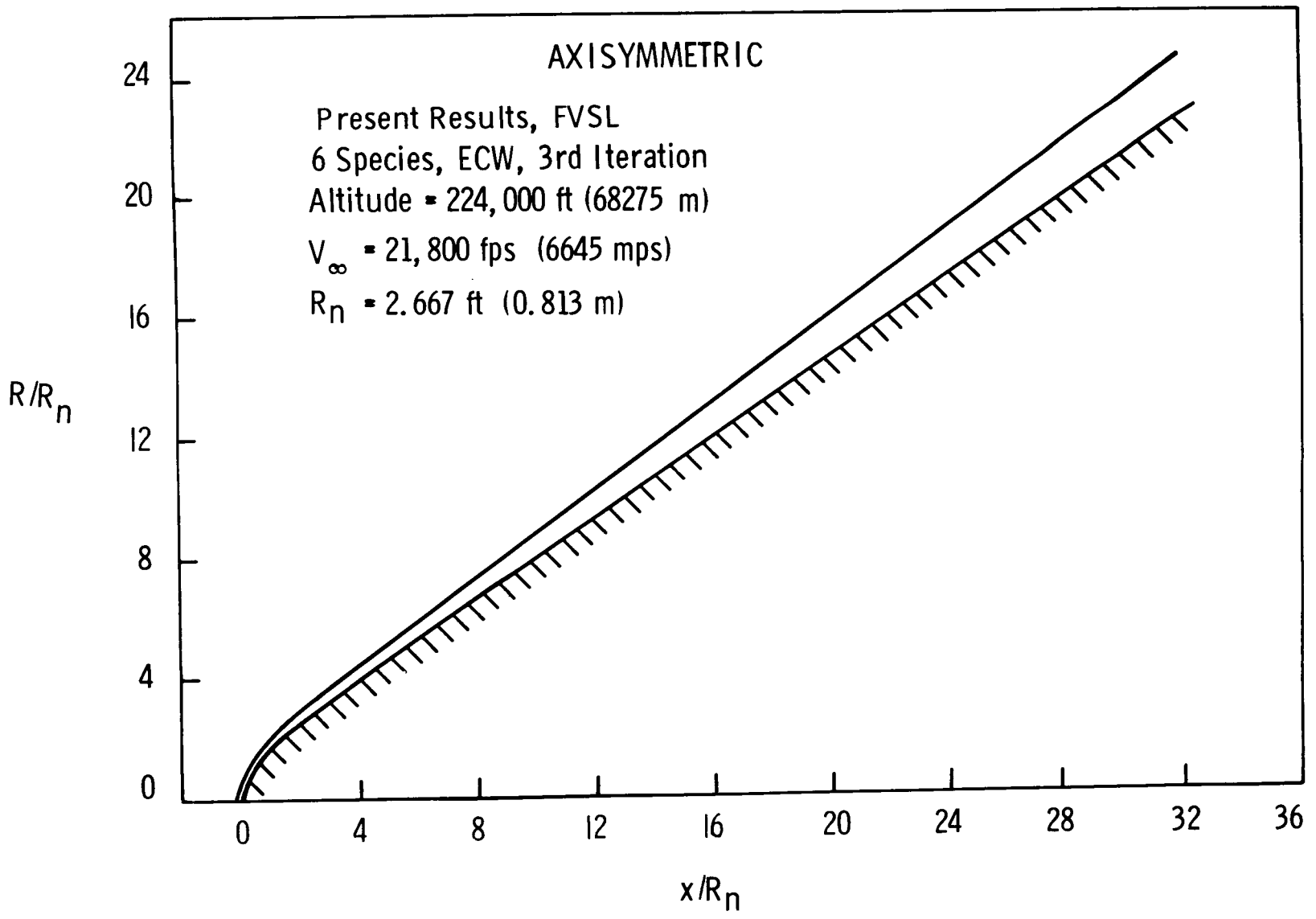

Figure 3. Body and Shock Geometry for NASA Shuttle-like Body

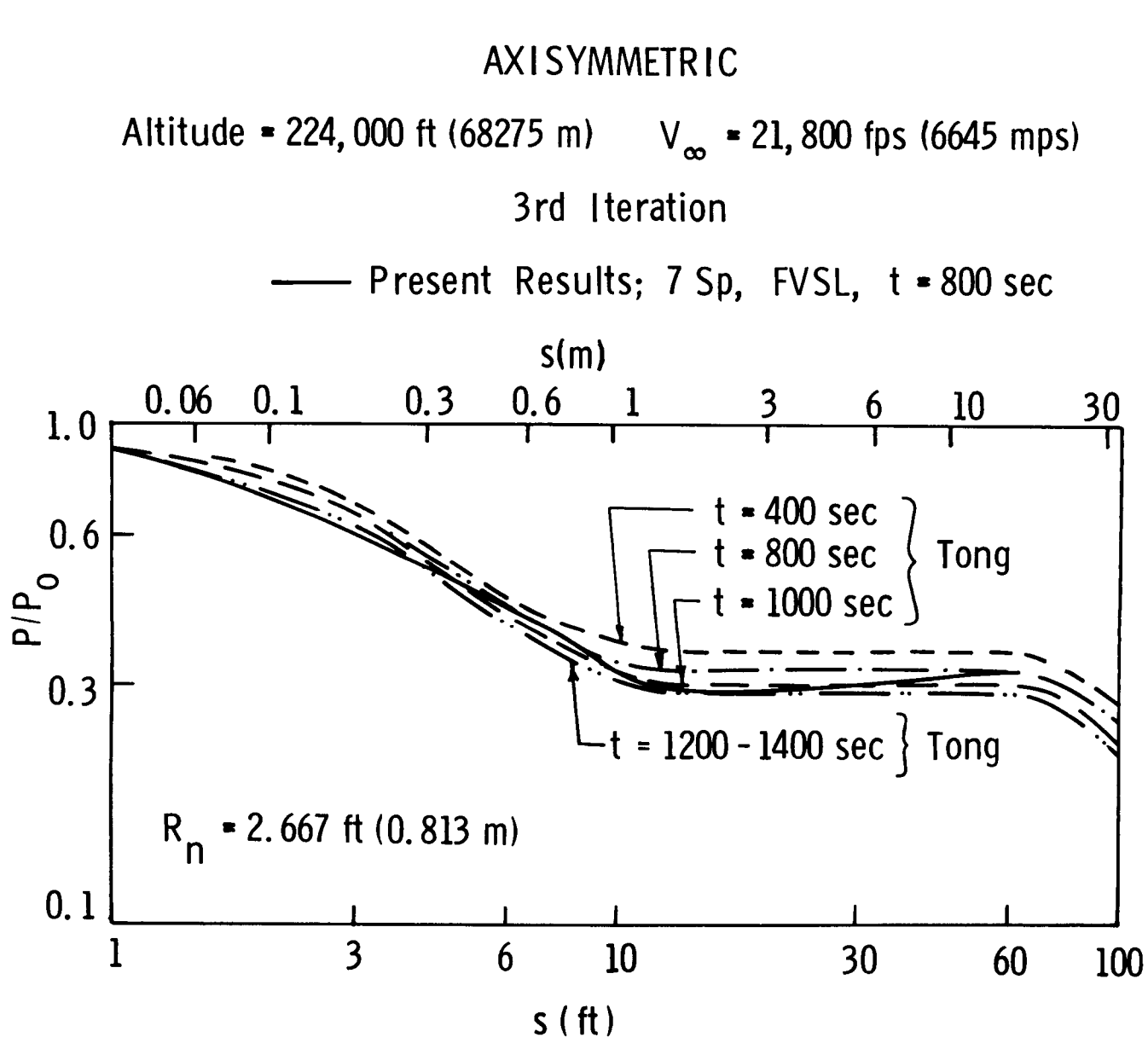

Figure 4. Pressure Distributions for NASA Shuttle-like Body

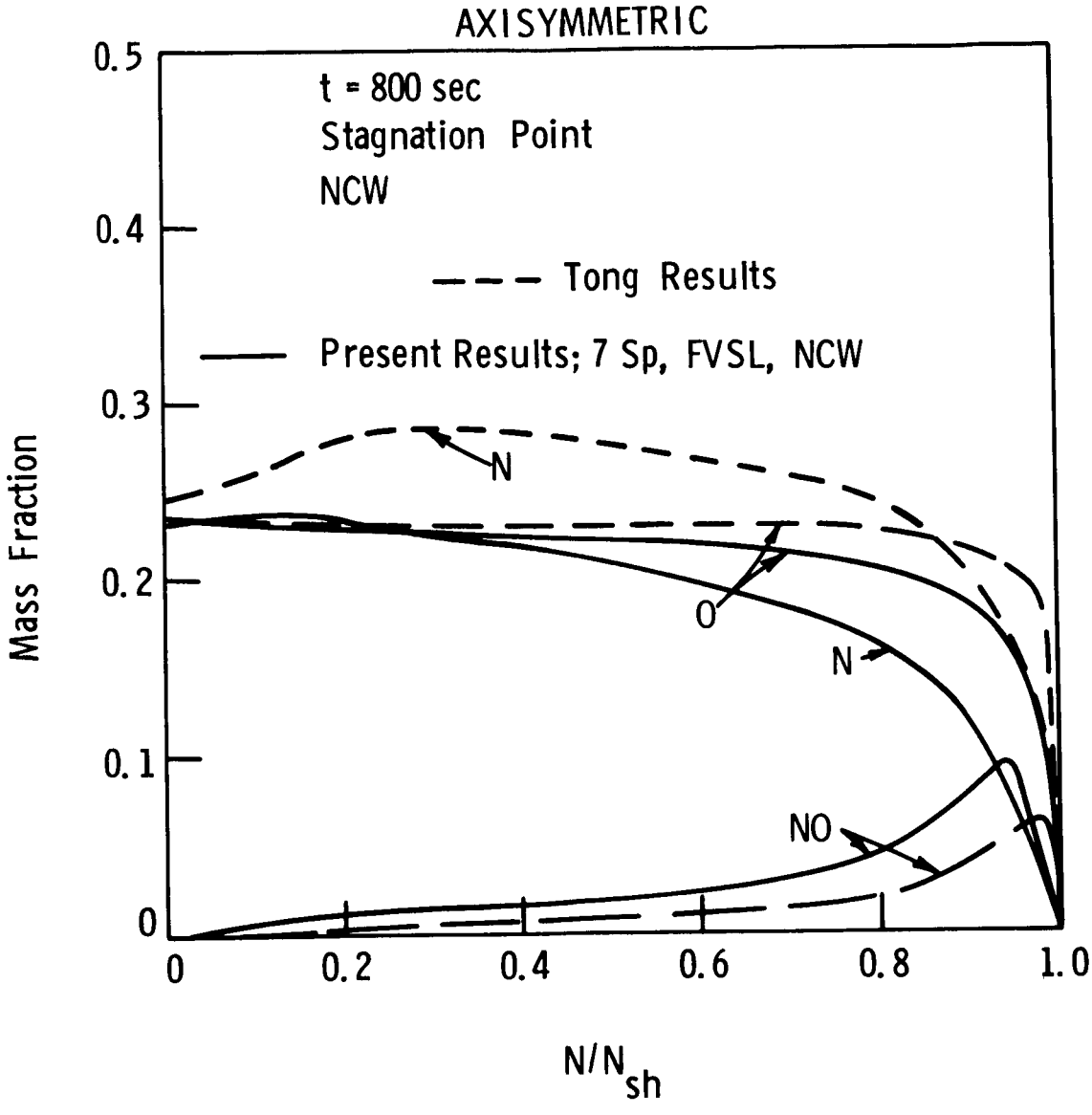

Figure 5. Stagnation Point Species Mass Fractions for NASA Shuttle-like Body

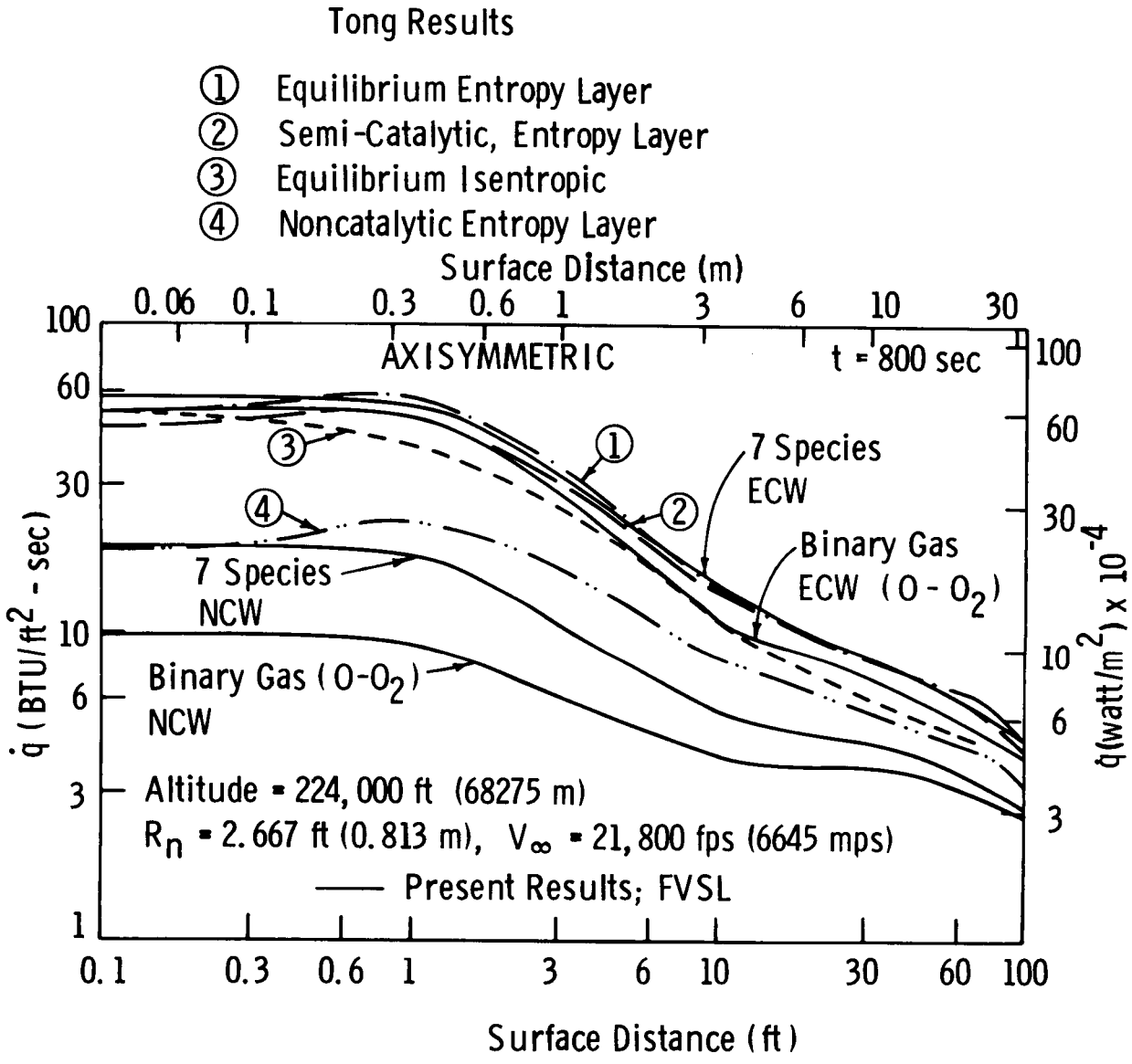

Figure 6. Heat-Transfer Distributions for NASA Shuttle-like Body

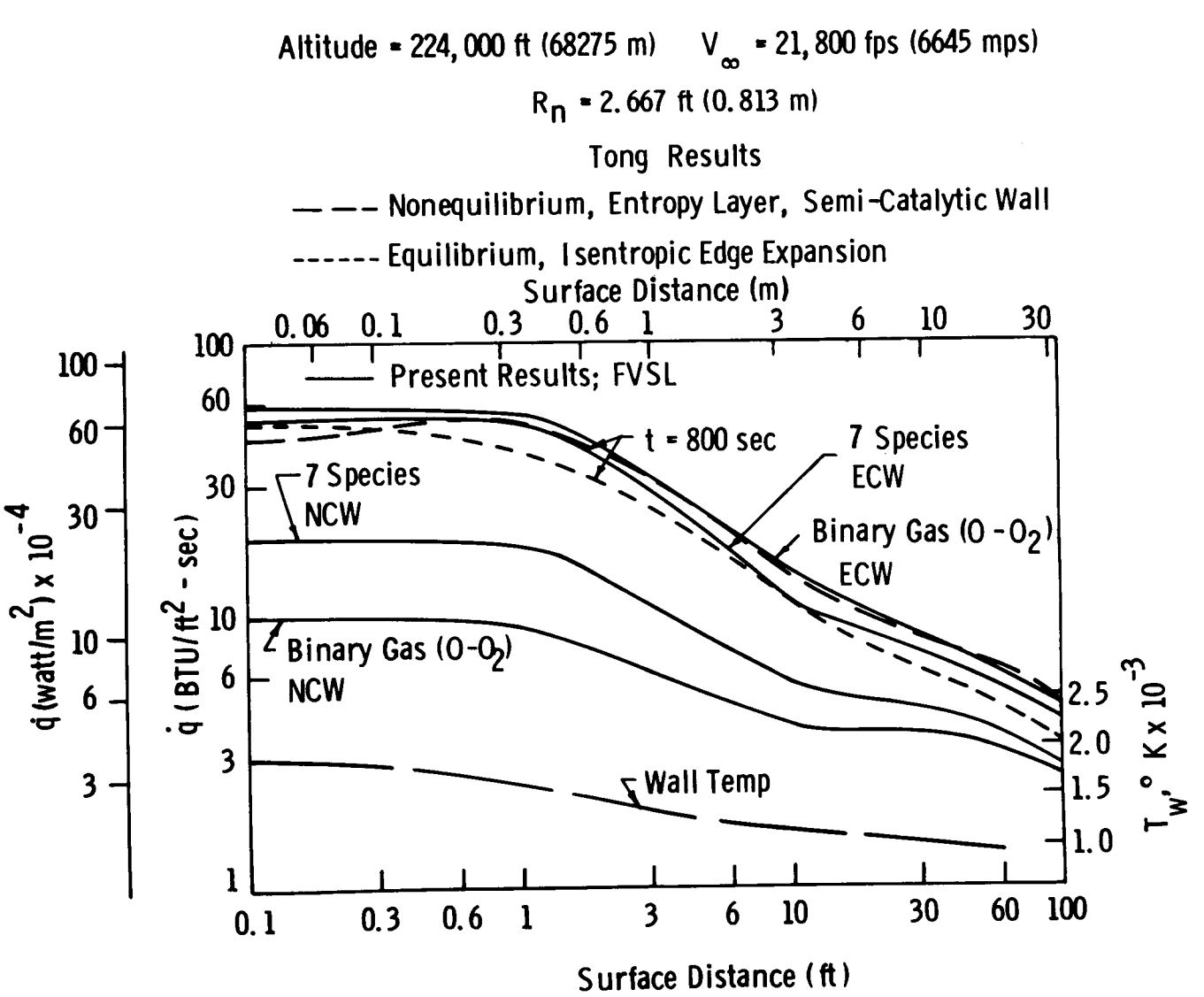

Figure 7. Heat-Transfer and Wall Temperature Distributions for NASA Shuttle-like Body

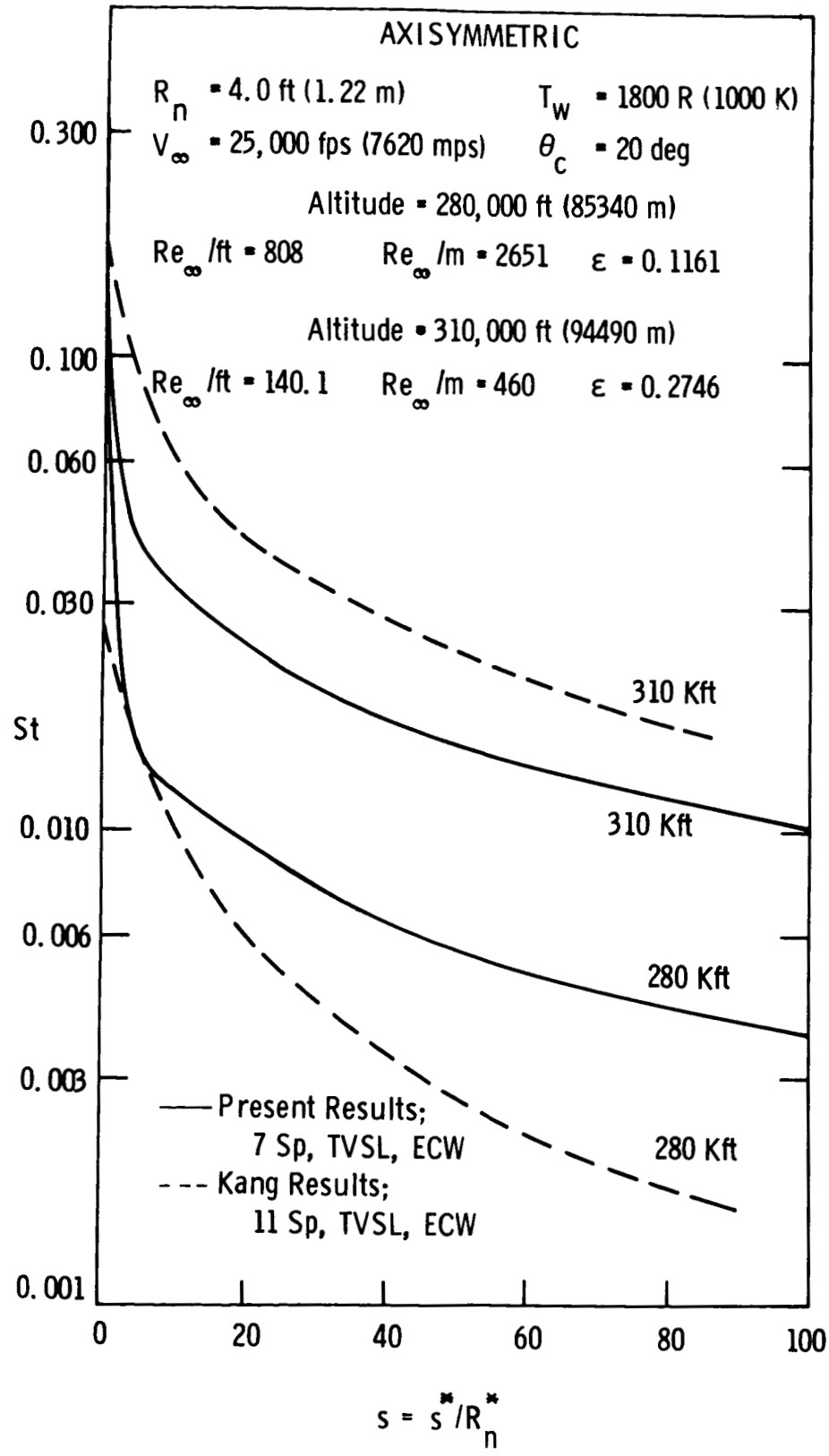

Figure 8. Stanton Number Distributions for 20° Sphere-Cone

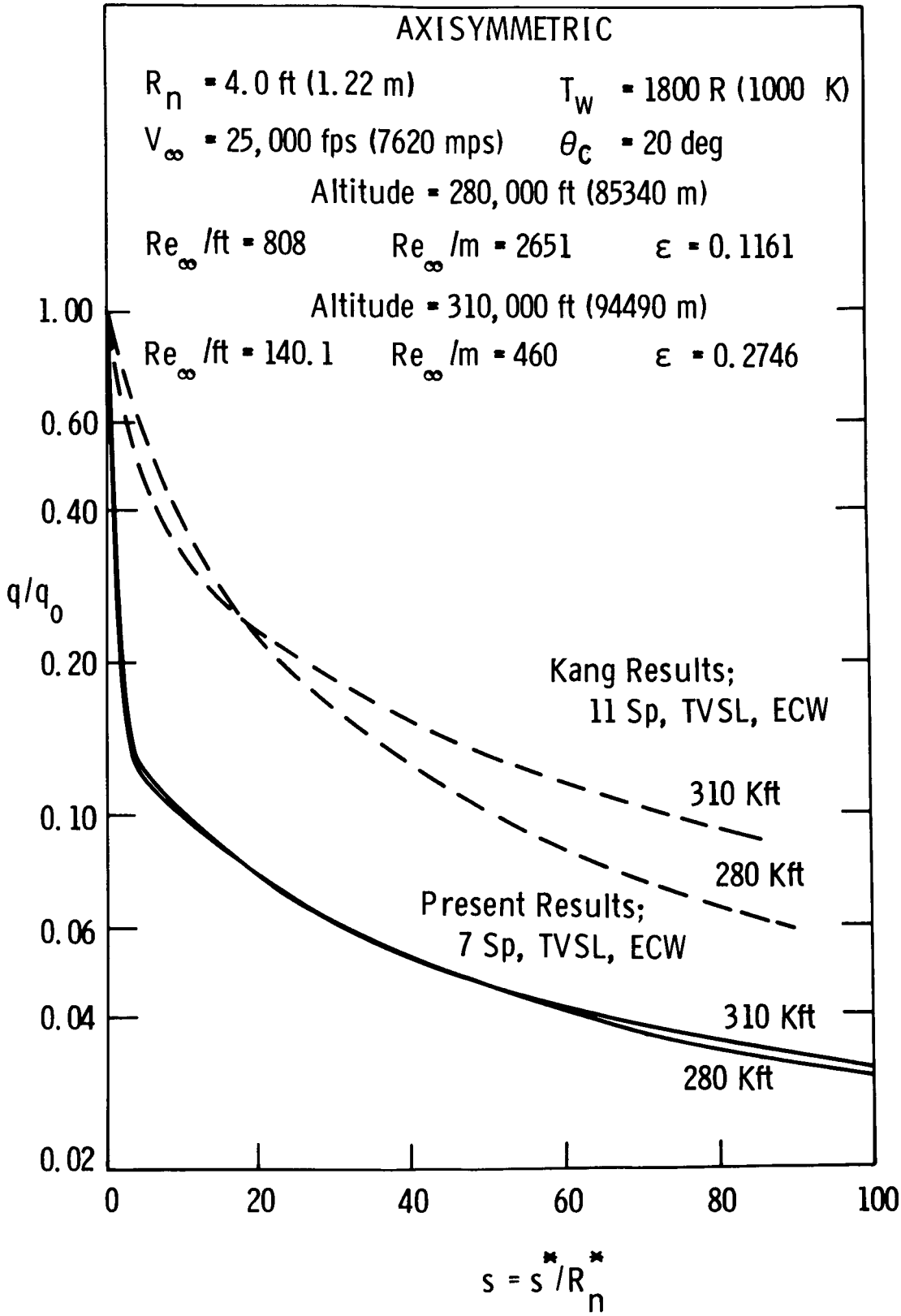

Figure 9. Normalized Heat-Transfer Distributions for 20° Sphere-Cone

AXISYMMETRIC

Altitude = 280,000 ft (85,344 m) V_∞ = 25,000 fps (7620 mps)

Re_∞/ft = 808 Re_∞/m = 2651 θ_c = 20 deg

R_n = 4.0 ft (1.22 m) T_W = 1800 °R (1000 °K) ε = 0.1161

—— Present Results; 7 Sp, TVSL, ECW

--- Kang Results; 11 Sp, TVSL, ECW

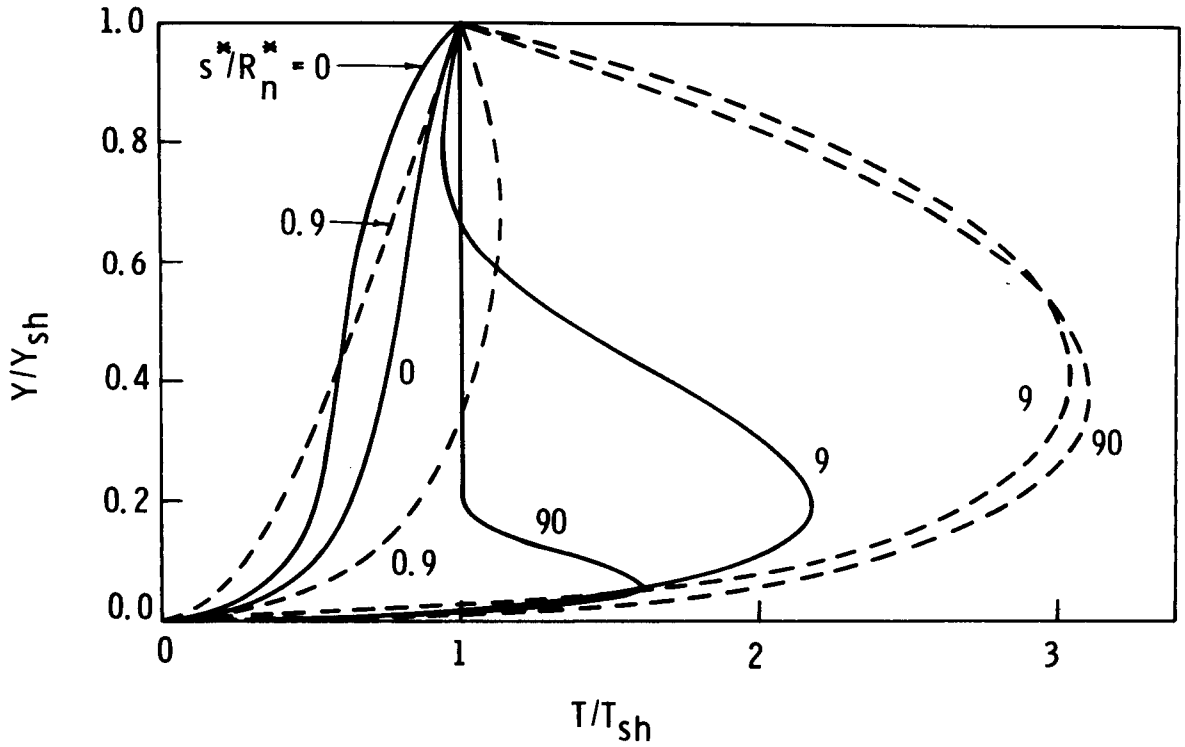

Figure 10. Temperature Profiles for 20° Sphere-Cone at 280 Kft

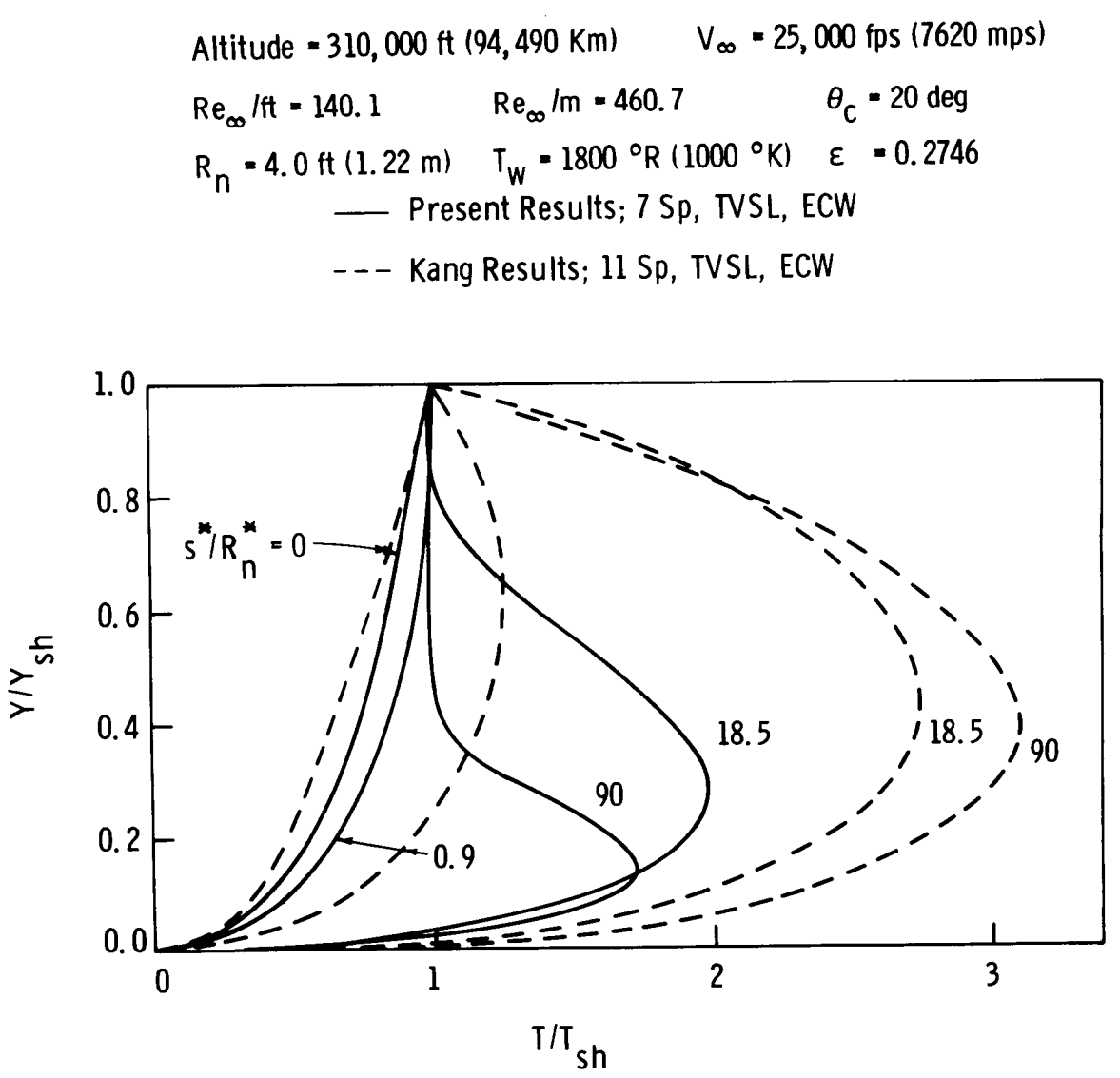

Figure 11. Temperature Profiles for 20° Sphere-Cone at 310 Kft

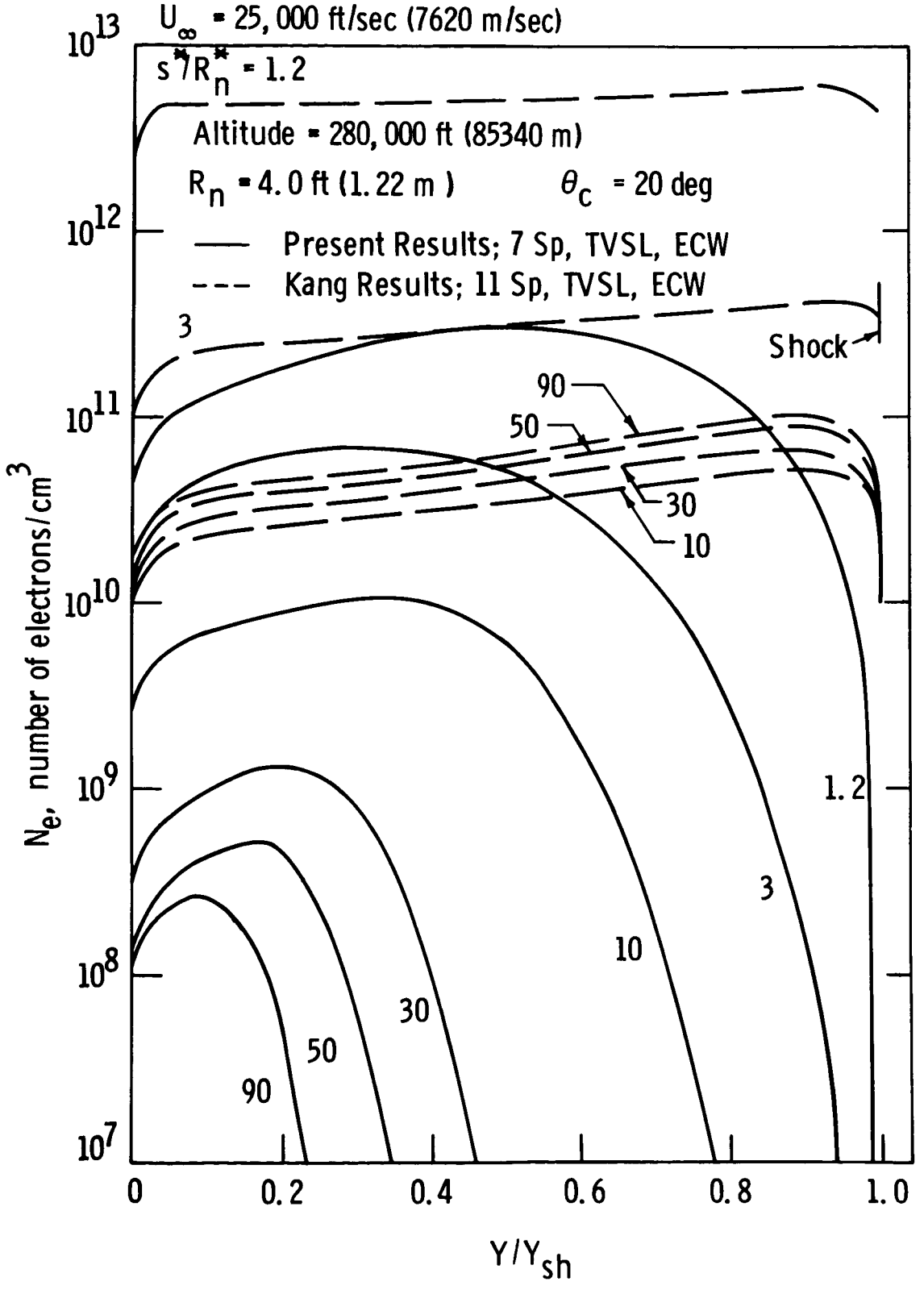

Figure 12. Electron Concentration Profiles for 20° Sphere-Cone at 280 Kft

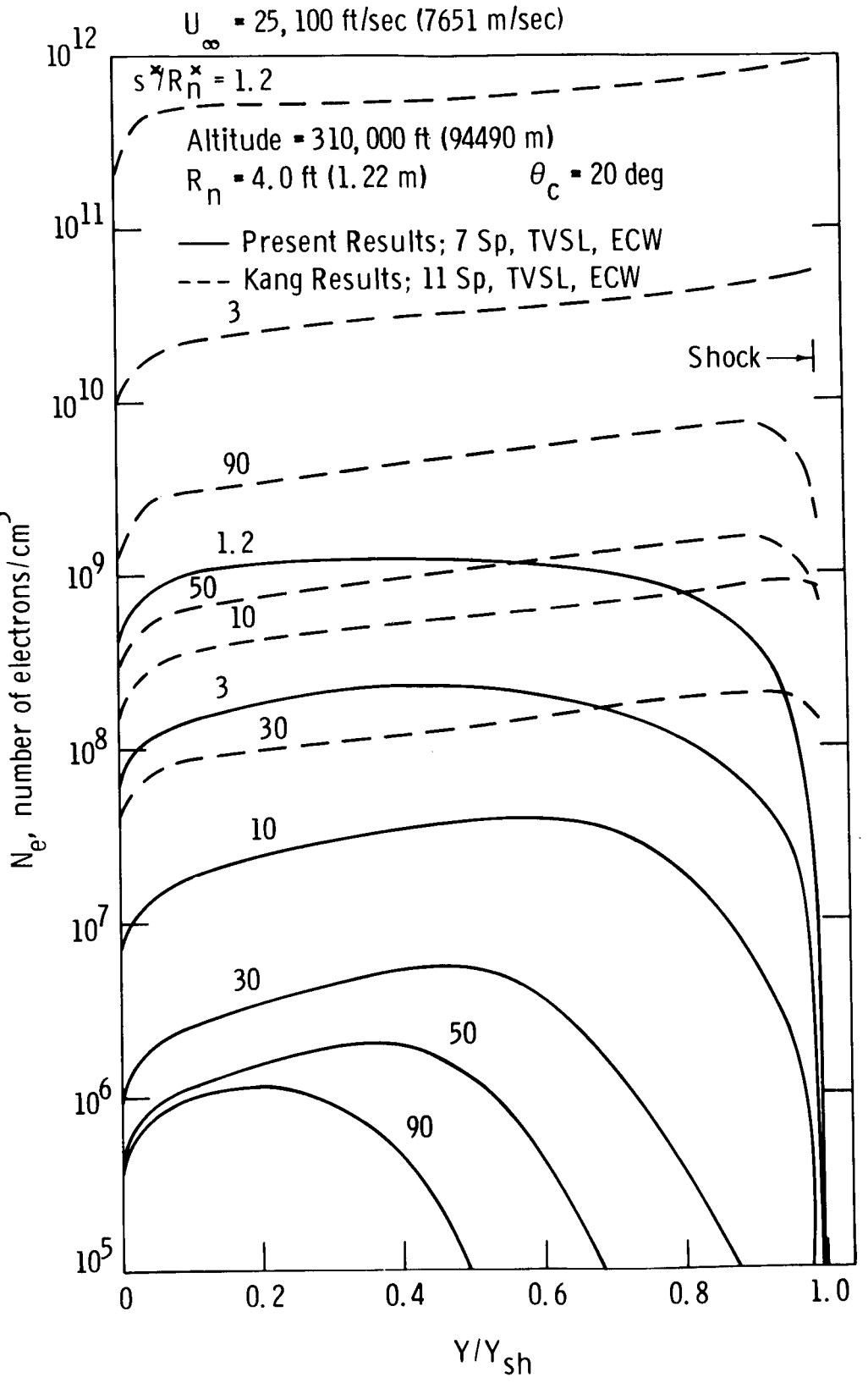

Figure 13. Electron Concentration Profiles for 20° Sphere-Cone at 310 Kft

AXISYMMETRIC

Altitude = 230,000 ft (70100 m) θ_c = 9 deg

Re_∞/ft = 8630 Re_∞/m = 28314

R_n = 0.5 ft (0.15 m) T_w = 1800 °R (1000 °K)

V_∞ = 25,000 fps (7620 mps)

CURVE	GAS	BODY	THEORY	ITER	SHOCK	WALL
			Present Results			
1	$O\text{-}O_2$	Hyp	TVSL	2	NSS	ECW
2	7 Sp	Hyp	TVSL	2	NSS	ECW
3	$O\text{-}O_2$	Cone	TVSL	2	NSS	ECW
4	7 Sp	Cone	TVSL	2	NSS	ECW
			Kang Results			
5	11 Sp	Cone	TVSL	2	SS	ECW

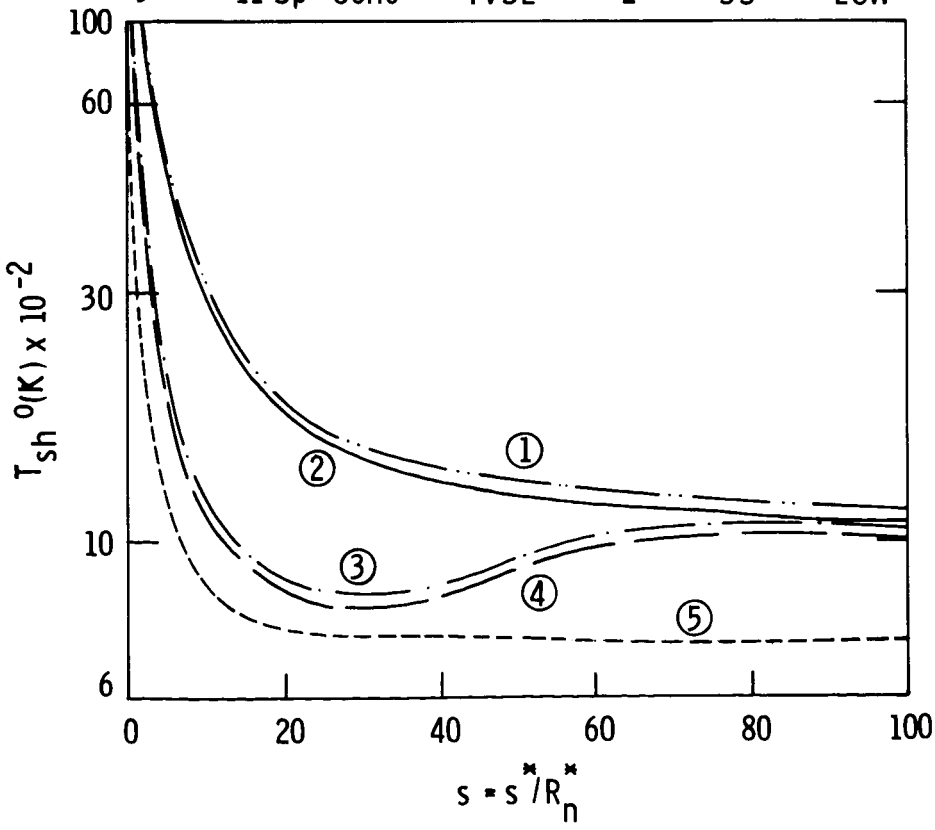

Figure 14. Shock-Temperature Distributions for RAM C Conditions, 230 Kft

AXISYMMETRIC

Altitude = 230,000 ft (70100 m) θ_c = 9 deg

Re_∞/ft = 8630 Re_∞/m = 28314

R_n = 0.5 ft (0.15 m) T_w = 1800 °R (1000 °K)

V_∞ = 25,000 fps (7620 mps)

CURVE	GAS	BODY	THEORY	ITER	SHOCK	WALL
			Present Results			
1	7 Sp	Cone	Inviscid	-	--	-
2	O-O_2	Cone	TVSL	2	NSS	ECW
3	7 Sp	Cone	TVSL	2	NSS	ECW
4	O-O_2	Hyp	TVSL	2	NSS	ECW
5	7 Sp	Hyp	TVSL	2	NSS	ECW
			Kang Results			
6	11 Sp	Cone	TVSL	2	SS	ECW

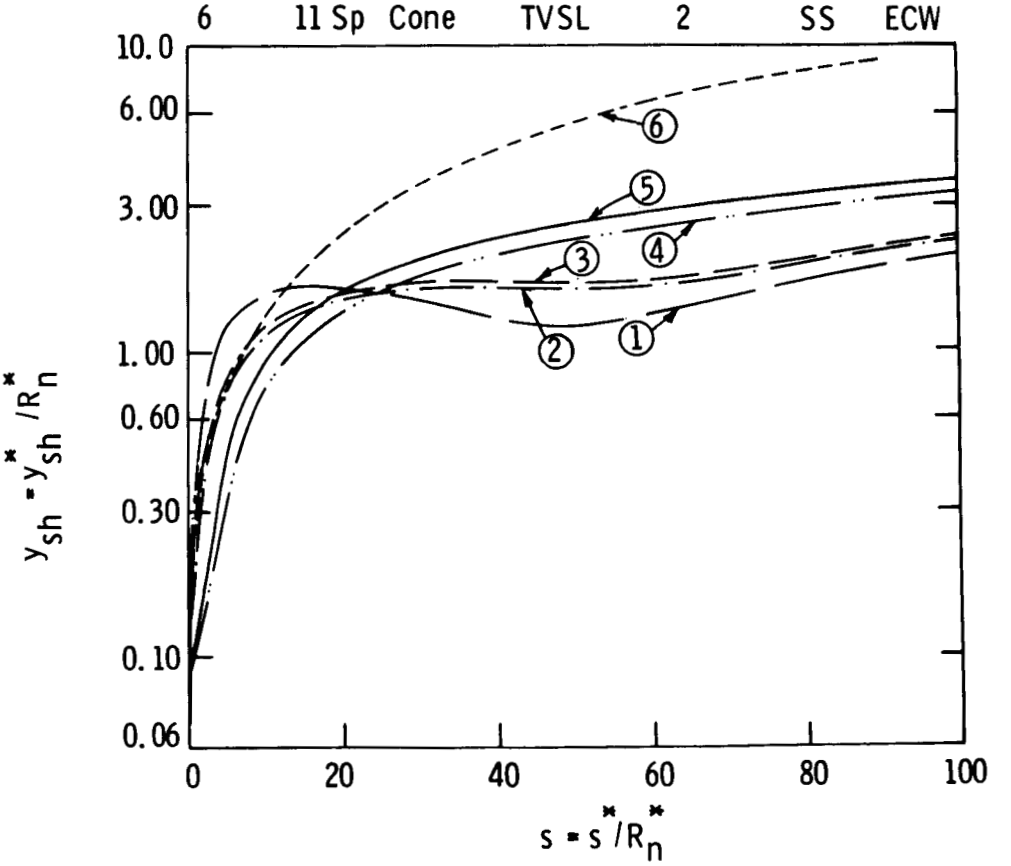

Figure 15. Shock-Layer Thickness Distributions for 9° Sphere-Cone, RAM C Conditions, 230 Kft

AXISYMMETRIC

Altitude = 230,000 ft (70100 m) θ_c = 9 deg

Re_∞/ft = 8630 Re_∞/m = 28314

R_n = 0.5 ft (0.15 m) T_w = 1800 °R (1000 °K)

V_∞ = 25,000 fps (7620 mps)

CURVE	GAS	BODY	THEORY	ITER	SHOCK	WALL	s^*/R_n^*
			Present Results				
1	7 Sp	Cone	TVSL	2	NSS	ECW	8.8
			Kang Results				
2	11 Sp	Cone	TVSL	2	SS	ECW	10.0

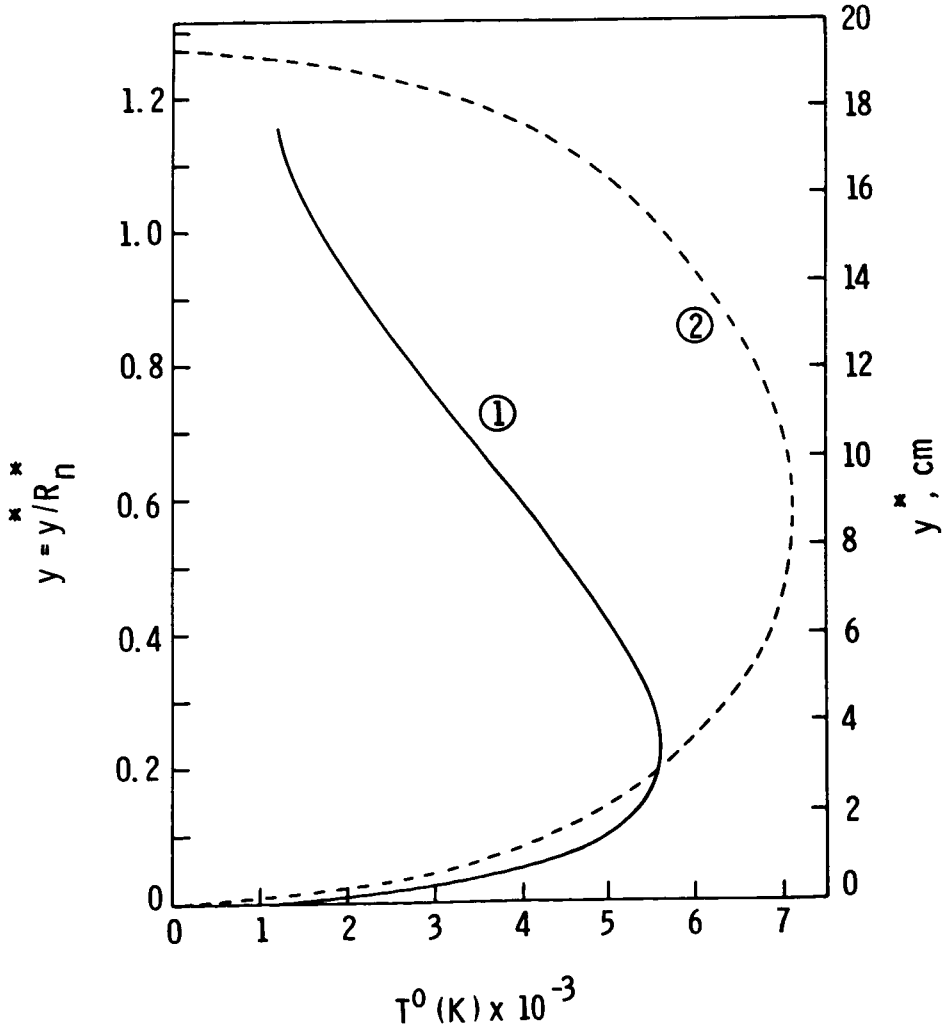

Figure 16. Temperature Profiles for 9° Sphere-Cone Near Probe Location, RAM C Conditions, 230 Kft

AXISYMMETRIC

Altitude = 230,000 ft (70100 m) θ_c = 9 deg

Re_∞/ft = 8630 Re_∞/m = 28314

R_n = 0.5 ft (0.15 m) T_w = 1800 °R (1000 °K)

V_∞ = 25,000 fps (7620 mps)

CURVE	GAS	BODY	THEORY	ITER	SHOCK	WALL
			Present Results			
1	7 Sp	Hyp	TVSL	2	NSS	ECW
2	O-O_2	Hyp	TVSL	2	NSS	ECW
3	O-O_2	Cone	TVSL	2	NSS	ECW
4	7 Sp	Cone	TVSL	2	NSS	ECW
			Kang Results			
5	11 sp	Cone	TVSL	2	SS	ECW

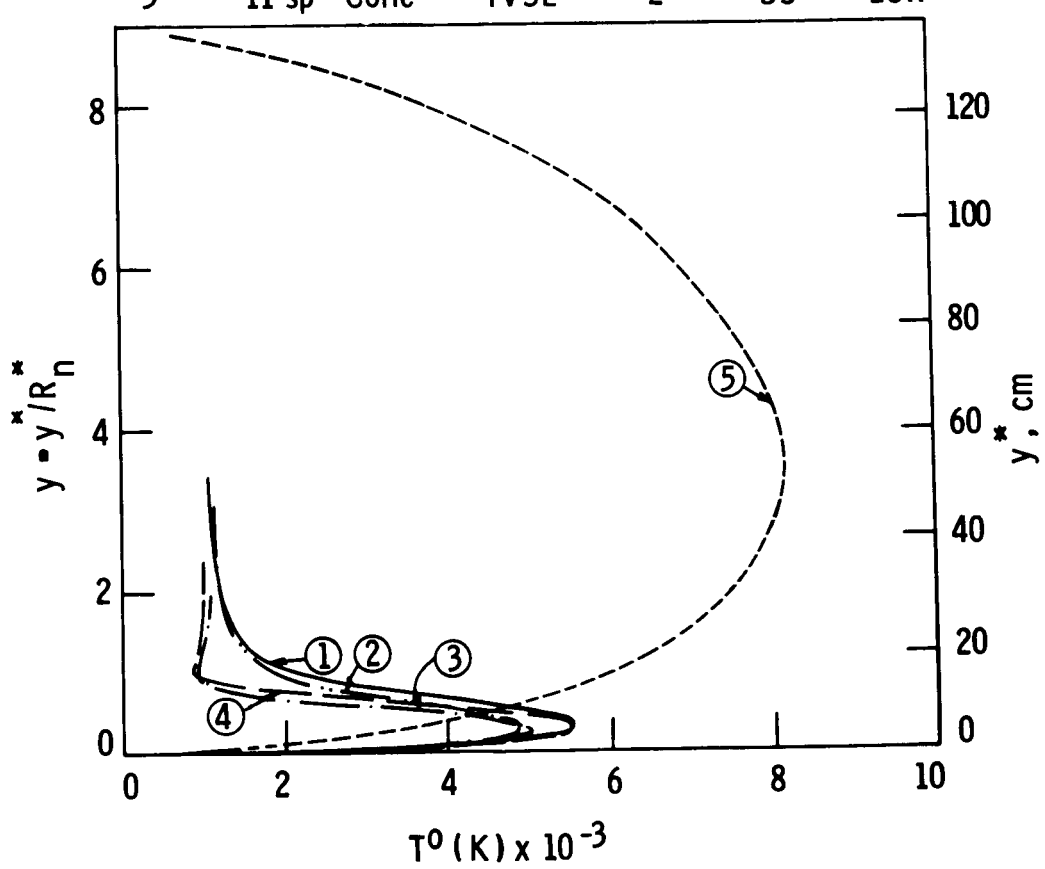

Figure 17. Temperature Profiles for RAM C Conditions at s/R_n = 90, 230 Kft

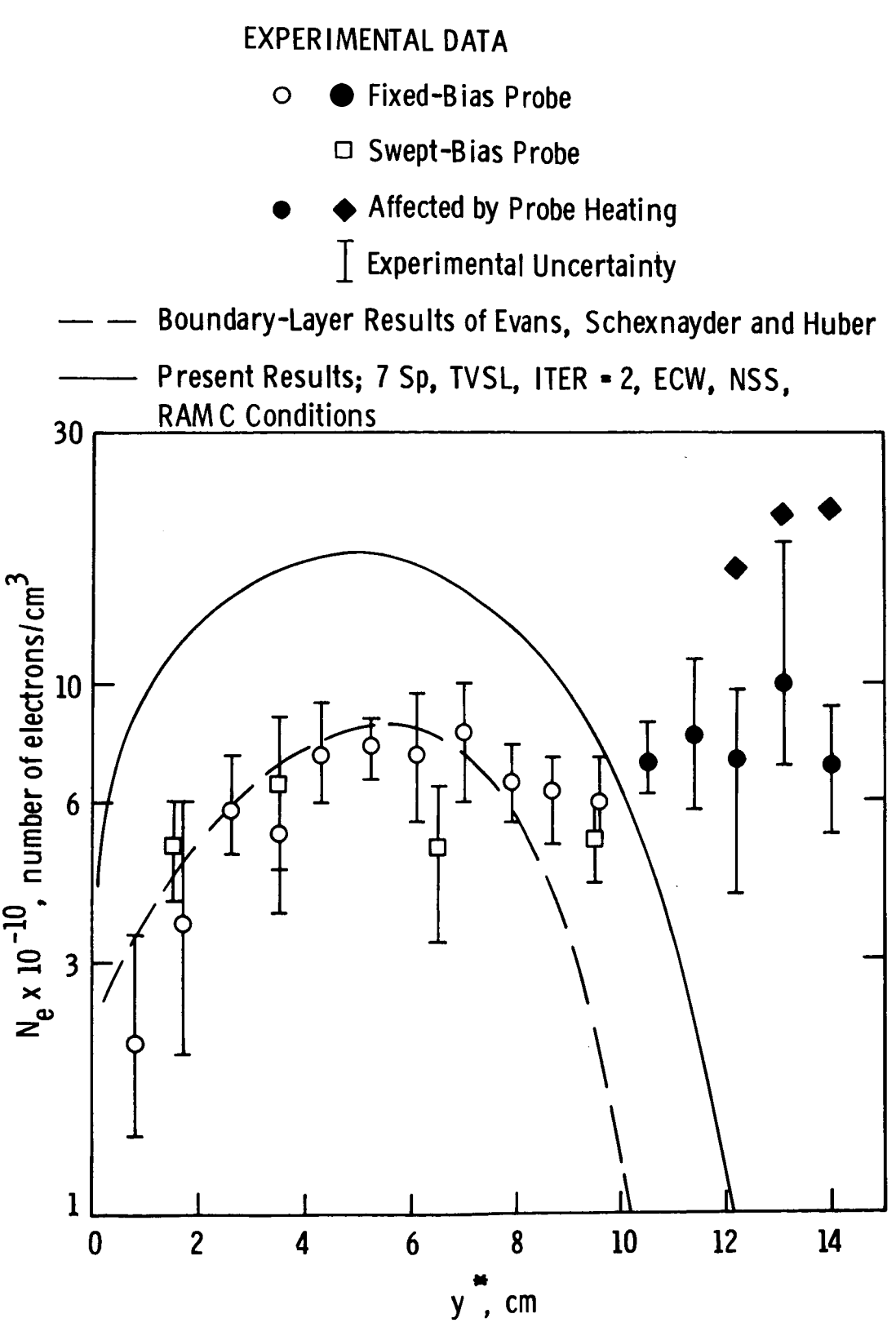

Figure 18. Present Electron Concentration Profiles Compared with Experimental and Boundary-Layer Theory Profiles, s/R_n = 8.8, RAM C Conditions, 230 Kft

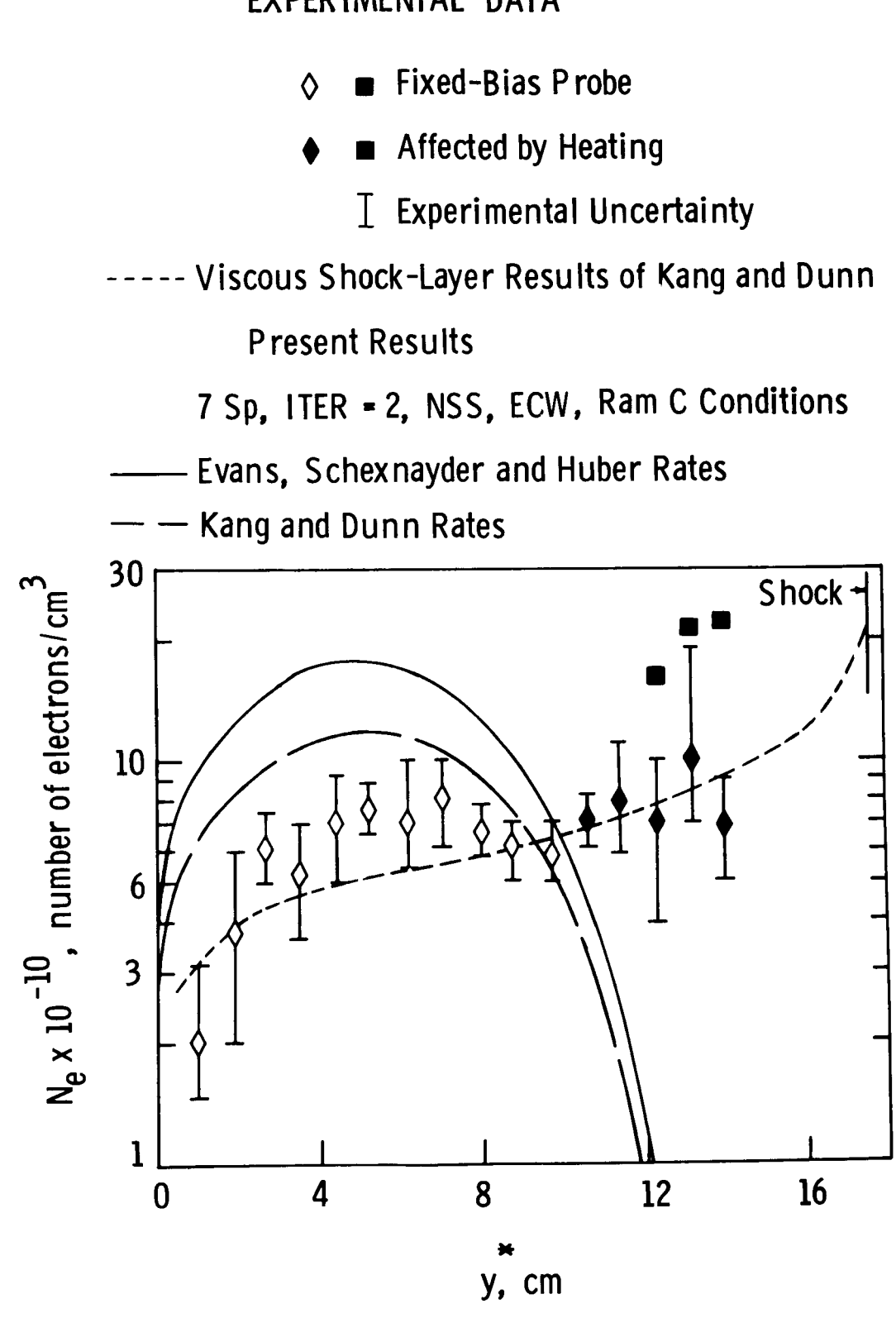

Figure 19. Present Electron Concentration Profiles with Different Reaction Rates Compared with Experimental and Kang and Dunn Profiles, s/R_n = 8.8, RAM C Conditions, 230 Kft

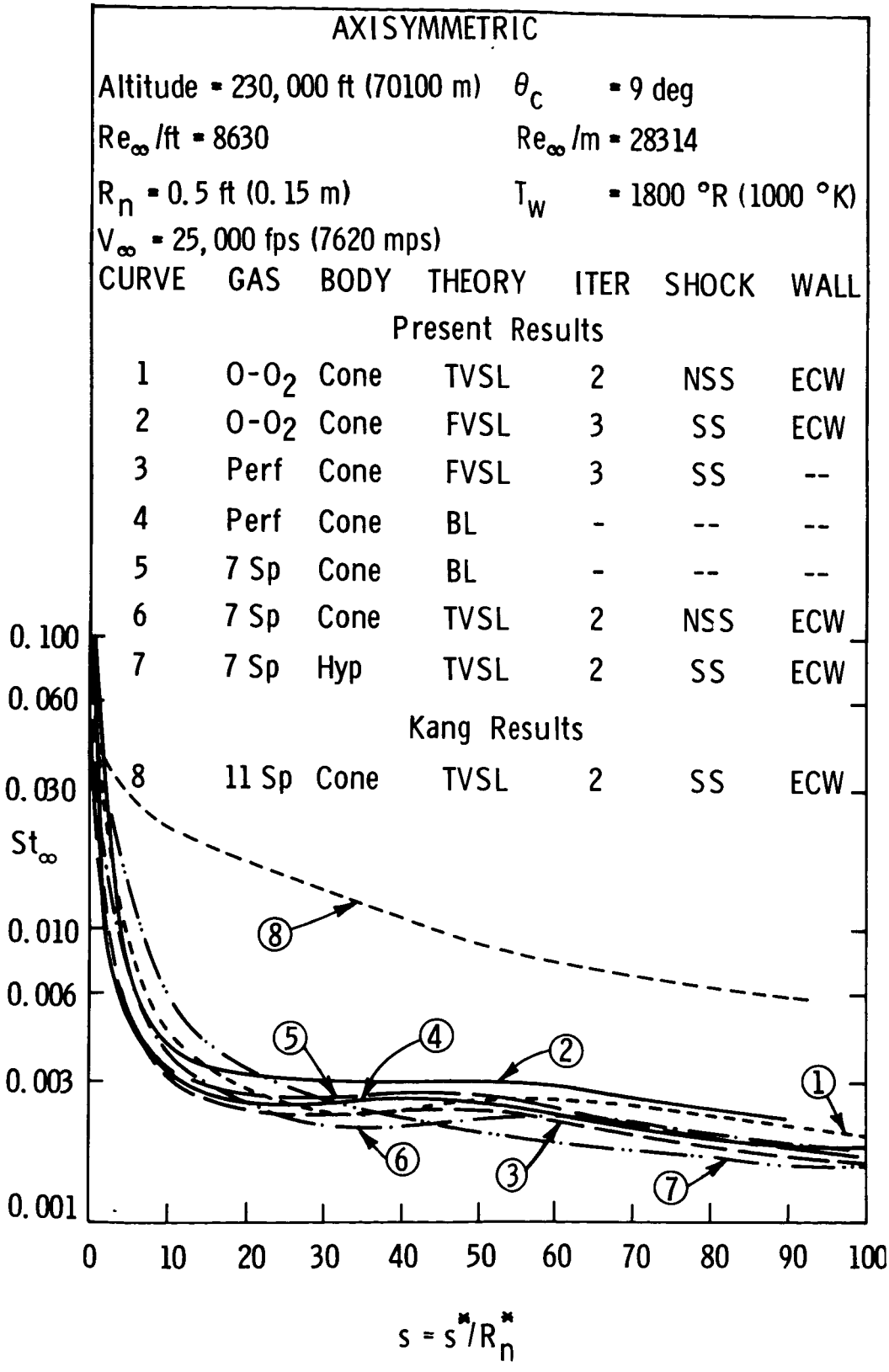

Figure 20. Stanton Number Distributions for 9° Sphere-Cone, RAM C Conditions, 230 Kft

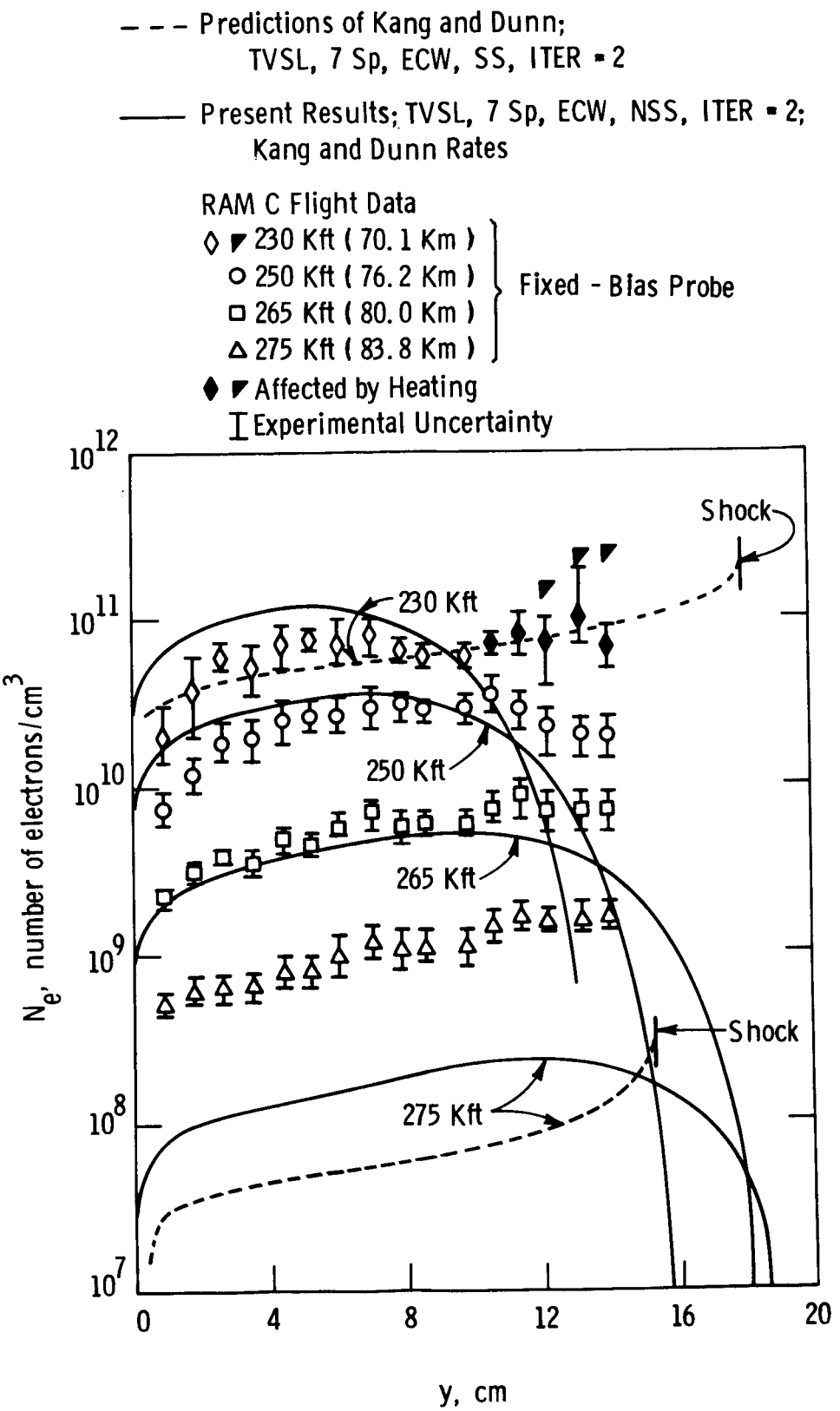

Figure 21. Present Predictions of Electron Concentration Profiles without Shock Slip Compared with Experimental Data and Predictions of Kang and Dunn, s/R_n = 8.8, RAM C Conditions

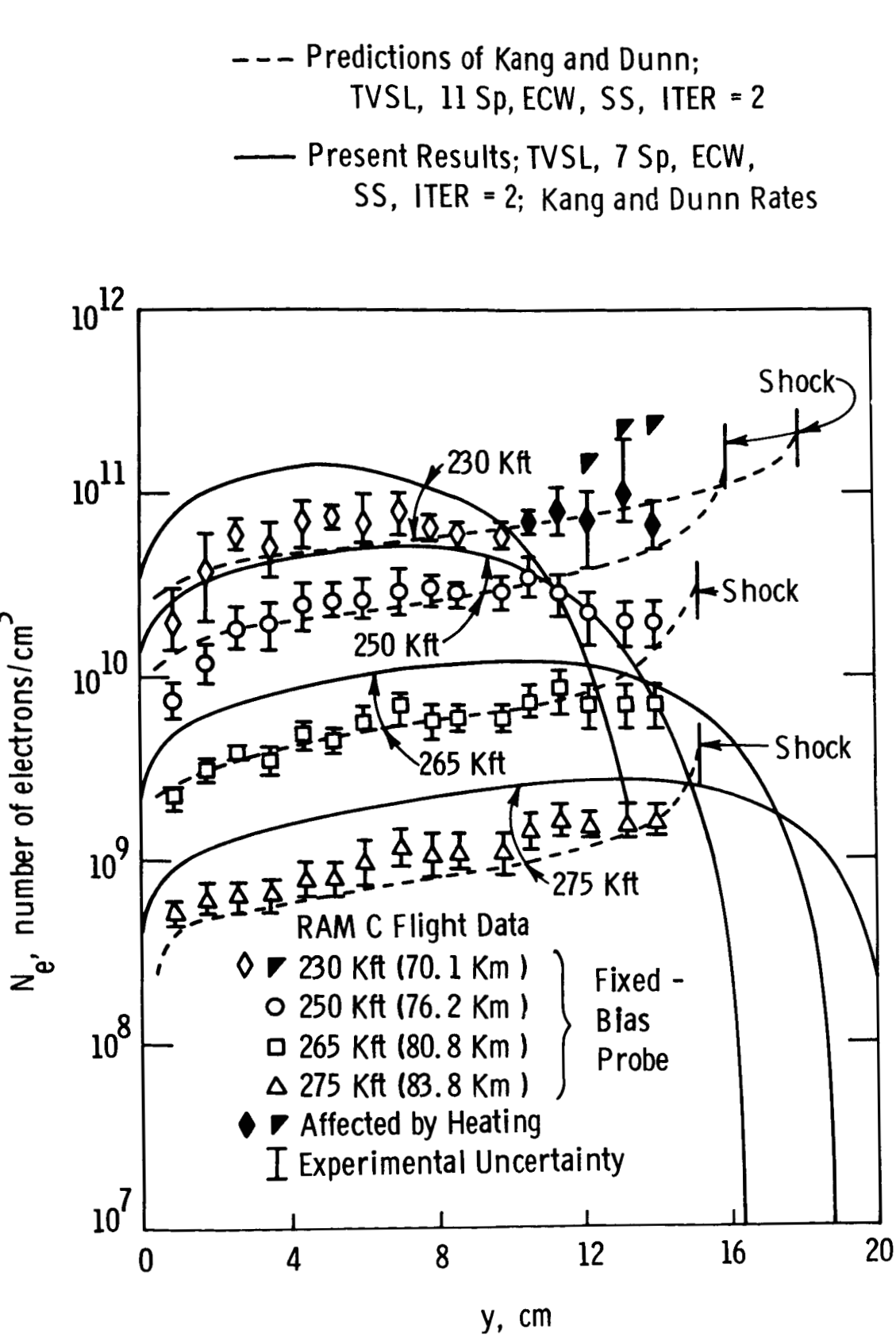

Figure 22. Present Predictions of Electron Concentration Profiles with Shock Slip Compared with Experimental Data and Predictions of Kang and Dunn, s/R_n = 8.8, RAM C Conditions

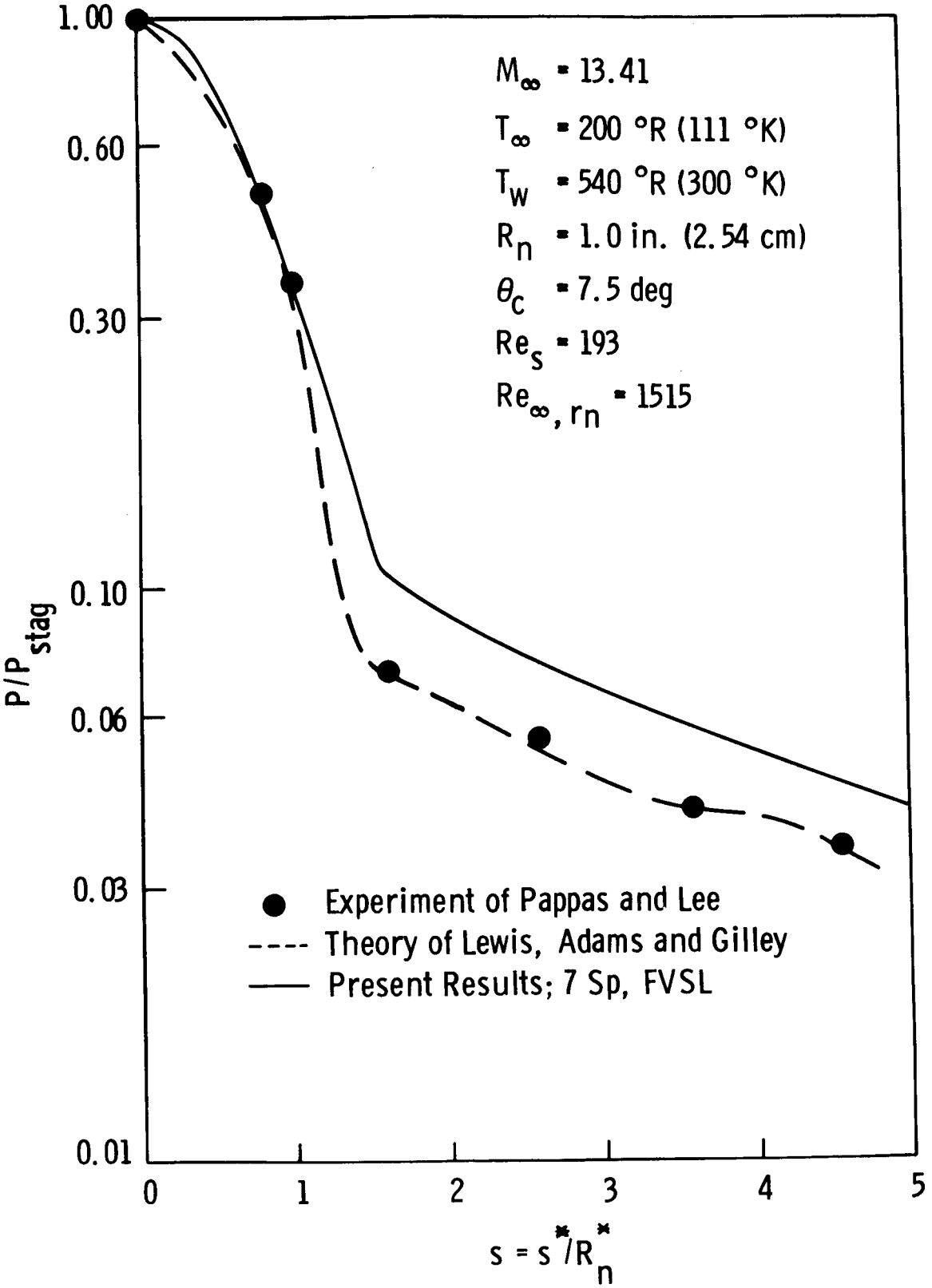

Figure 23. Normalized Surface-Pressure Distributions for 7.5° Sphere-Cone, Ames Conditions

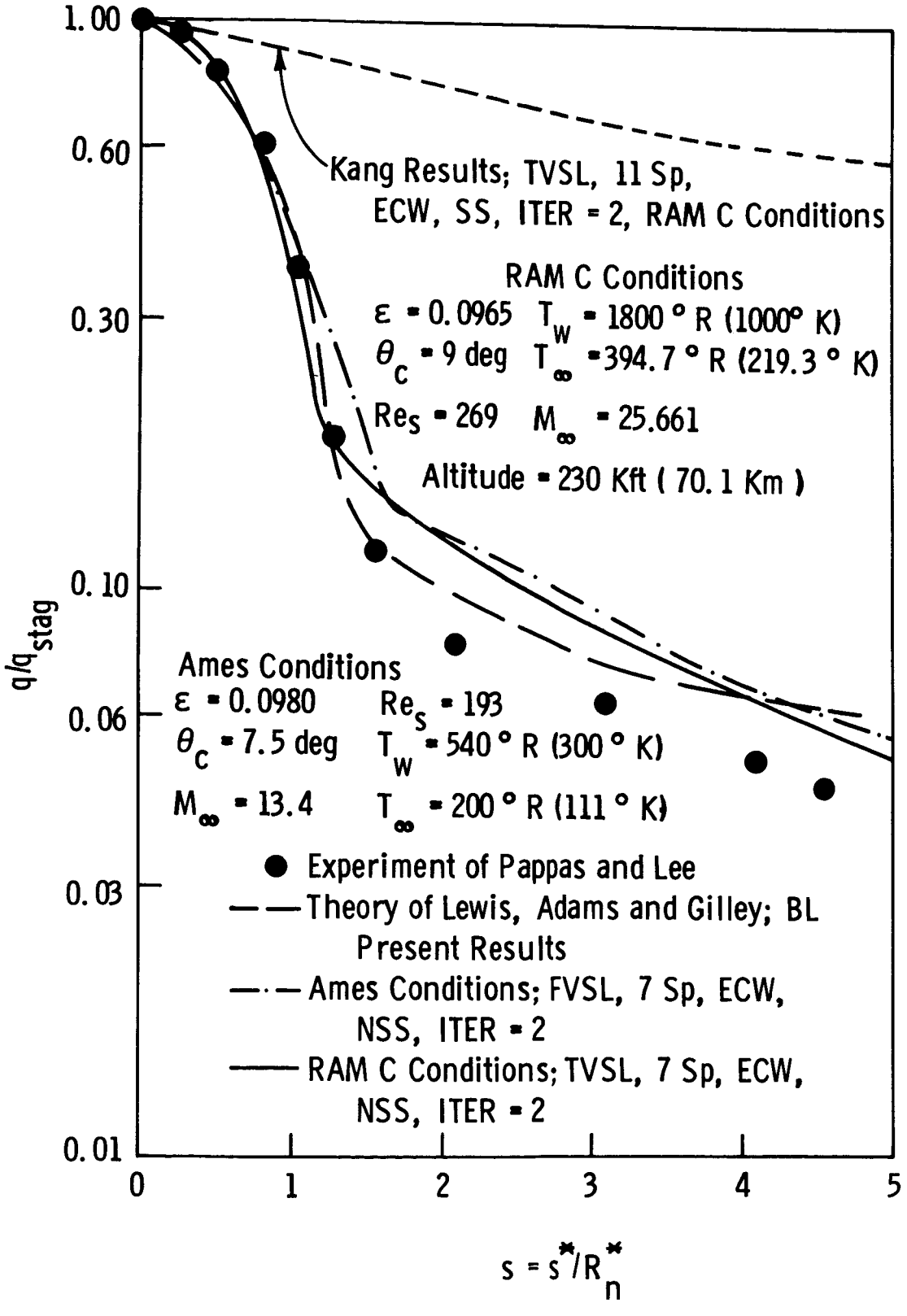

Figure 24. Normalized Heat-Transfer Distributions for 7.5° Sphere-Cone, Ames Conditions

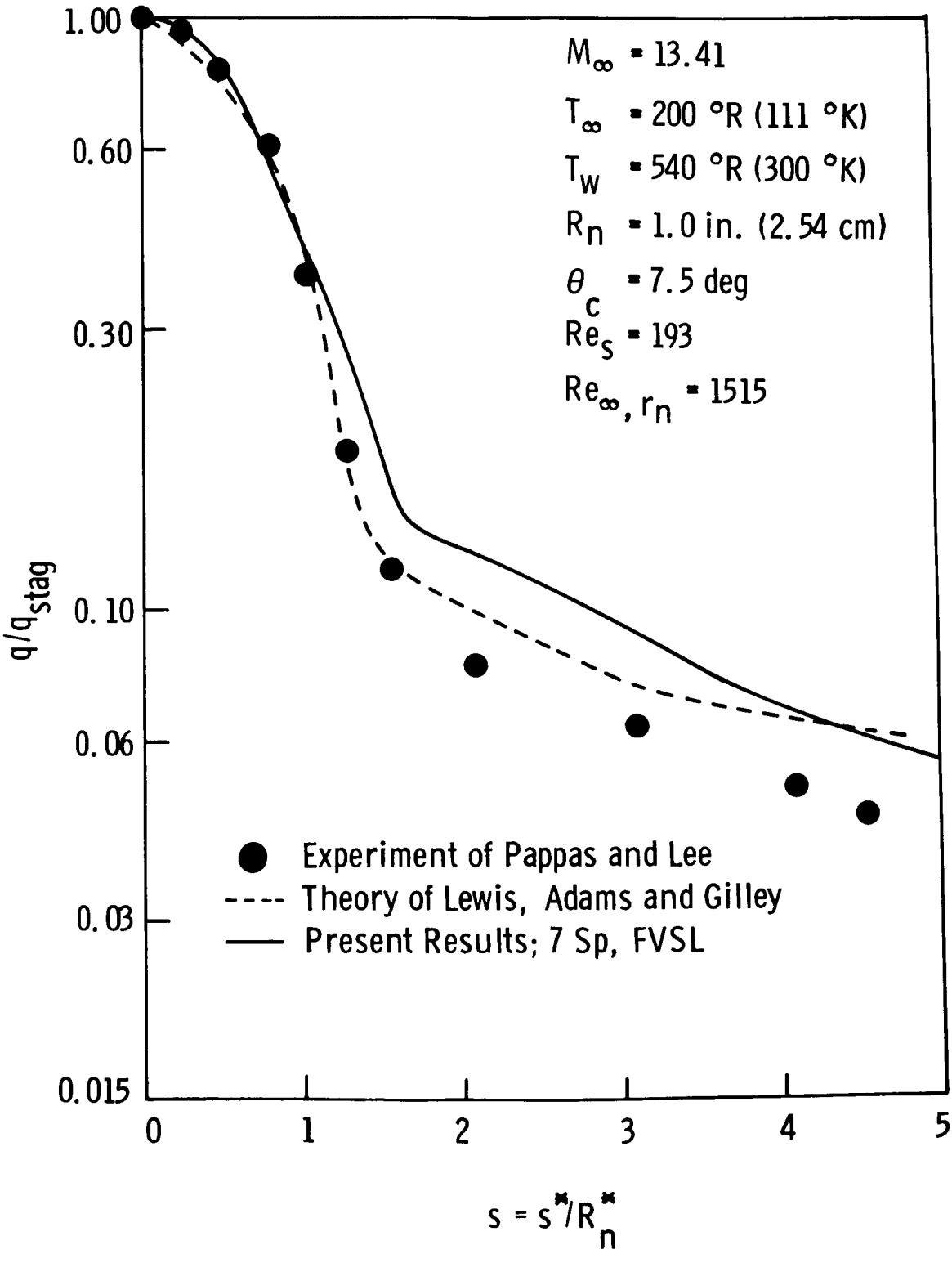

Figure 25. Comparison of Predicted Heat-Transfer Distributions for Sphere-Cones, RAM C and Ames Conditions